

# Simulations of Ductile Fracture in Pipeline Steels under Quasi-Static and Dynamic Loading Conditions

by

Christopher W. Bassindale

A thesis submitted to the Faculty of Graduate and Postdoctoral  
Affairs in partial fulfillment of the requirements for the degree of

Master of Applied Science

in

Mechanical Engineering

Carleton University  
Ottawa, Ontario

© 2017, Christopher W. Bassindale

## **Abstract**

To circumvent numerous costly experimental investigations of full scale pipeline burst tests, fracture resistance parameters are determined from small scale lab tests for a given material. Developed over the past several decades, fracture parameters such as the Charpy V-notch energy, drop weight tear test (DWTT) absorbed energy, and most recently the crack tip opening angle (CTOA) have proven to be useful design tools for the pipeline industry. The CTOA is becoming a rival measure of ductile fracture propagation; however, there are several aspects such as the effect of loading mode and loading rate, which are still under investigation.

In this thesis, extensive finite element simulations of ductile fracture propagation were analyzed using the cohesive zone model (CZM). The analyses focused on the effect of loading mode under quasi-static loading conditions on the CTOA, and higher loading rates on the CTOA and CZM parameters. Two common pipeline steels were used in this work, namely, American Petroleum Institute (API) standard C2-X70 and C4-X100. A small scale yielding (SSY) model, a clamped single edge notch tensile (SENT) model, and a DWTT model were examined under quasi-static loading conditions. The SSY model examined the effect of the traction-separation law (TSL) shape on crack growth resistance and the CTOA. The quasi-static SENT and DWTT models were compared to assess the effect of loading mode on the CTOA. The DWTT was also examined under an impact loading rate. A plate model, which simplifies the geometry of a pipe to a plate, was examined under a dynamic loading rate. These two models were utilized to assess the effect of loading rate on the CTOA and the TSL.

The results of the loading mode simulations demonstrate that the CTOA has a weak dependence on the loading mode (constraint). Moreover, this work reinforces the notion of the transferability of the CTOA from the DWTT (bending) to a more representative loading mode for pipeline applications (tensile).

The results of the loading rate study demonstrate that the CZM must be recalibrated to produce an experimental parameter, such as the dynamic CTOA, for higher loading rates. A relation between the cohesive energy and crack velocity was developed to provide insight into the effect of loading rate on the CZM based on a constant CTOA model. Lastly, this study provided data that supports the notion that the upswing in the Battelle two curve method (TCM) is due to the effect of inertia.

## **Acknowledgements**

First and foremost, I would like to thank Professor Xin Wang, my thesis supervisor, for all of his support, encouragement and guidance throughout the course of my master's work. As well, I would also like to thank my thesis co-supervisor, Dr. William Tyson, for his support and guidance throughout this work.

I would also like to thank the fast ductile fracture arrest methodology group at CanmetMATERIALS, specifically, Dr. Su Xu, Dr. Hari Simha, Dr. Mark Gesing, and Dr. Bruce Williams for their insight and assistance. Moreover, the financial support from Natural Resources Canada was greatly appreciated. I would also like to extend my appreciation to Carleton University and NSERC for the financial support through scholarships and grants.

Last but not least, I would like to thank my friends and family for their support throughout these busy times.

# Table of Contents

<b>Abstract</b> .....	<b>ii</b>
<b>Acknowledgements</b> .....	<b>iv</b>
<b>Table of Contents</b> .....	<b>v</b>
<b>List of Tables</b> .....	<b>x</b>
<b>List of Figures</b> .....	<b>xii</b>
<b>Nomenclature</b> .....	<b>xviii</b>
<b>Acronyms</b> .....	<b>xxi</b>
<b>Chapter 1: Introduction</b> .....	<b>1</b>
1.1 Thesis Objectives.....	4
1.2 Thesis Outline.....	5
<b>Chapter 2: Literature Review and Background</b> .....	<b>7</b>
2.1 Modelling of Ductile Fracture using the Cohesive Zone Model .....	7
2.2 Fracture Toughness Characterization of Pipeline Steels .....	12
2.3 The Crack Tip Opening Angle (CTOA).....	13
2.3.1 CTOA Measurement – Optical Method.....	13
2.3.2 CTOA Measurement - Simplified Single Specimen Method.....	15
2.3.3 Effect of T-Stress (Constraint) on the CTOA .....	16
2.3.4 Effect of crack velocity on the CTOA .....	17
2.4 Pipeline Design for Dynamic Fracture .....	19
2.5 DWTT Experimental Methods .....	21
2.6 Pipeline Steels .....	23
2.6.1 Stress-Strain Relationship of Pipeline Steels .....	24
2.6.2 Effect of Strain Rate on The Strength of Pipeline Steels .....	24
2.6.3 Implementation of the Material Model in ABAQUS .....	26

2.6.4	Verification of the Material Model in ABAQUS.....	27
2.7	Motivation for the Current Work.....	28
<b>Chapter 3: The Cohesive Zone Model and Parameter Calibration .....</b>		<b>42</b>
3.1	Traction-Separation based Modelling in ABAQUS.....	43
3.1.1	Linear Elastic Behavior.....	43
3.1.2	Damage Initiation.....	44
3.1.3	Damage Evolution.....	45
3.1.4	Element Based Cohesive Zone Modelling in ABAQUS.....	46
3.2	Calibration of the Cohesive Zone Model Parameters.....	47
3.2.1	Cohesive Stiffness.....	47
3.2.2	Shape of the Traction Separation Law .....	48
3.2.3	Cohesive Energy .....	50
3.2.4	Maximum Traction.....	51
3.2.5	Effect of Separation Rate on the TSL .....	52
3.2.6	Cohesive Zone Mesh Sizing.....	53
3.2.7	TSL Calibration with the DWTT Model.....	55
3.3	Verification of the Cohesive Zone Model .....	56
<b>Chapter 4: FE Simulation of Ductile Fracture Using a Small Scale yielding Model under Quasi-Static Loading Conditions .....</b>		<b>65</b>
4.1	Small Scale Yielding (SSY) Model.....	65
4.1.1	Geometry and Computational Procedures.....	65
4.1.2	Loading Conditions.....	66
4.1.3	Material Properties .....	68
4.1.4	Cohesive Zone Properties .....	68
4.1.5	FE Mesh Design.....	69
4.2	Analysis Methodology.....	70

4.3	Verification of the SSY Model.....	71
4.4	Results and Discussion – Effect of the TSL Shape on Crack Growth Resistance and the CTOA	72
4.5	Conclusions .....	73
<b>Chapter 5: FE Simulations of a Single Edge Notch Tension Specimen under Quasi-static Loading Conditions .....</b>		<b>84</b>
5.1	Clamped Single Edge Notch Tensile (SENT) Specimen Model.....	84
5.1.1	Geometry and Computational Procedures.....	84
5.1.2	Loading Conditions.....	85
5.1.3	Material Properties .....	86
5.1.4	Cohesive Zone Properties .....	86
5.1.5	SENT FE Mesh Design.....	86
5.2	Analysis Methodology.....	87
5.3	Results and Discussion – Effect of Loading Mode on the CTOA.....	87
5.4	Conclusions .....	89
<b>Chapter 6: FE Simulations of a Drop Weight Tear Test Specimen under Quasi-static Loading Conditions.....</b>		<b>98</b>
6.1	Drop Weight Tear Test (DWTT) Model .....	98
6.1.1	Geometry and Computational Procedures.....	99
6.1.2	Material Properties .....	100
6.1.3	Cohesive Zone Properties .....	100
6.1.4	Loading Conditions.....	100
6.1.5	Finite Element Mesh Design.....	101
6.2	Analysis Methodology.....	102
6.3	Results and Discussion – Quasi-Static Loading Conditions.....	102
6.3.1	CTOA.....	102

6.3.2	Load-Load Line Displacement.....	103
6.4	Conclusions .....	104
<b>Chapter 7: FE Simulations of a Drop Weight Tear Test Specimen under Impact Loading Conditions.....</b>		<b>111</b>
7.1	Drop Weight Tear Test (DWTT) Model .....	111
7.1.1	Geometry and Computational Procedures.....	112
7.1.2	Material Properties .....	112
7.1.3	Cohesive Zone Properties .....	112
7.1.4	Loading Conditions.....	112
7.1.5	Finite Element Mesh Design .....	113
7.2	Analysis Methodology.....	113
7.3	Results and Discussion – Impact Loading Rate .....	114
7.3.1	CTOA.....	114
7.3.2	Crack Growth Rate.....	115
7.3.3	Load-Load Line Displacement (Load-LLD).....	117
7.4	Crack Velocity – Cohesive Energy Relationship .....	118
7.4.1	X70.....	119
7.4.2	X100.....	120
7.5	Conclusions .....	122
<b>Chapter 8: FE Simulations of a Plate Model under Dynamic Loading Conditions</b>		<b>133</b>
8.1	Tensile Plate Model.....	133
8.1.1	Geometry and Computational Procedures.....	133
8.1.2	Material Properties .....	135
8.1.3	Cohesive Zone Properties .....	135
8.1.4	Loading Conditions.....	136
8.1.5	Mesh Design.....	137

8.2	Analysis Methodology.....	137
8.3	Results and Discussion – Effect of Crack Velocity on the CTOA.....	138
8.3.1	Excluding Material Rate Hardening.....	138
8.3.2	Including Material Rate Hardening.....	141
8.4	Results and Discussion – Influence of Inertia.....	144
8.5	Conclusions.....	146
	<b>Chapter 9: Conclusions and Future Recommendations.....</b>	<b>165</b>
9.1	Conclusions.....	165
9.2	Thesis Applications and Limitations.....	169
9.3	Recommendations for Future Work.....	170
	<b>References.....</b>	<b>171</b>

## List of Tables

Table 2.1 - Chemical composition of X70 and X100 (%wt.) (Xu & Tyson, 2015). .....	31
Table 2.2 – Average tensile mechanical properties of X70 and X100 (2-3 trials) (Xu & Tyson, 2015). .....	31
Table 2.3 - Simulation material model parameters (ABAQUS input).....	31
Table 2.4 - Strain rates and dynamic stress terms from Eq. 2.5. ....	31
Table 2.5 - X70 Quasi-static true stress - plastic strain data. (ABAQUS input) .....	32
Table 2.6 – X100 Quasi-static true stress - plastic strain data. (ABAQUS input).....	33
Table 3.1 - CZM mesh parameters for SSY, SENT, DWTT and Plate models.....	58
Table 3.2 - TSL calibration trials with quasi-static DWTT model. ....	58
Table 3.3 - Quasi-static CZM parameters for SSY, SENT, DWTT and Plate model's....	58
Table 4.1 – TH steel stress and plastic strain data. (ABAQUS input).....	75
Table 4.2 - TH TSL parameters for verification analysis. ....	75
Table 4.3 - X70 TSL naming convention. ....	76
Table 4.4 - X70 TSL parameters.....	76
Table 4.5 - SSY model FE mesh specifications.....	76
Table 4.6 - TH steel parameters.....	77
Table 4.7 - SSY model average steady-state CTOA.....	77
Table 5.1 - SENT Mesh Details.....	91
Table 6.1 - Quasi-Static Cohesive Properties for X70 and X100. ....	105
Table 6.2 – DWTT Mesh Details.....	105
Table 7.1 - TSL parameters updated for impact loading rate (matching experimental CTOA). .....	123

Table 7.2 - Steady-state crack velocities.....	123
Table 8.1 - Plate model dimensions.....	147
Table 8.2 - Finite element mesh details of plate model.....	147
Table 8.3 - Steady-state crack velocities excluding material rate hardening.....	147
Table 8.4 - Average steady-state CTOA excluding material rate hardening.....	148
Table 8.5 - Steady-state crack velocity - Material rate hardening (no TSL update).....	148
Table 8.6 - Steady-state crack velocity - Material rate hardening (TSL updated for constant CTOA).....	148
Table 8.7 – Cohesive energy updated for constant CTOA.....	149
Table 8.8 – Steady-state crack velocities for mass scaling analysis.....	149
Table 8.9 – Average steady-state CTOA for mass scaling analysis.....	149

## List of Figures

Figure 2.1 - CTOA optical measurement (Darcis, McCowan, Wondhoff, McColskey, & Siewert, 2008)(modified).....	34
Figure 2.2 - FE CTOA measurement technique. ....	34
Figure 2.3 - Load vs. load-line displacement plots of shallow-notched DWTT specimens (Xu, Bouchard, & Tyson, 2007) .....	35
Figure 2.4 - Plots of $\ln(PPI)$ vs. $(Y-Y_i)S'$ relations and data range for determination of the Slope (Xu, Bouchard, & Tyson, 2007). ....	35
Figure 2.5 - Battelle two curve method. ....	36
Figure 2.6 - Standard DWTT test specimen dimensions. (ASTM, 2014) .....	36
Figure 2.7 - Quasi-static DWTT apparatus at CanmetMATERIALS.....	37
Figure 2.8 – DWTT impact tower at CanmetMATERIALS. ....	37
Figure 2.9 – Experimental Load-LLD data of X70 steel at quasi-static and impact loading rates. ....	38
Figure 2.10 - Experimental Load-LLD data of X100 steel at quasi-static and impact loading rates. ....	38
Figure 2.11 - X70 and X100 quasi-static engineering stress-strain curves.....	39
Figure 2.12 - Quasi-static true stress - true strain data. (X70 and X100) .....	39
Figure 2.13 - Dynamic stress term as a function of strain rate from Eq. 2.4. ....	40
Figure 2.14 - Unit cell model for material verification.....	40
Figure 2.15 - Material rate verification - X70.....	41
Figure 2.16 - Material rate verification - X100.....	41
Figure 3.1 - Concept of the cohesive zone model (Li & Chandra, 2002)(modified).....	59

Figure 3.2 - Generic traction separation law.....	60
Figure 3.3 - Implementation of cohesive elements in ABAQUS (ABAQUS, 2014). .....	61
Figure 3.4 - Various TSL shapes: (a) Constant (Dugdale, 1960), (b) Bilinear (Barenblatt, 1962), (c) Polynomial (Needleman, 1987), (d) Exponential, (e) Trapezoidal (Tvergaard & Hutchinson, 1992), (f) Smooth trapezoidal (Schwalbe, Scheider, & Cornec, 2013).....	61
Figure 3.5 - TSL rate dependence (Rate2 > Rate1 > Quasi-static).....	62
Figure 3.6 - Cohesive element. ....	62
Figure 3.7 - Unit cell loading conditions. ....	63
Figure 3.8 - X70 TSL verification. ....	63
Figure 3.9 – X100 TSL verification.....	64
Figure 4.1 - SSY model geometry. ....	77
Figure 4.2 - SSY model loading conditions.....	78
Figure 4.3 - TH steel true stress-true strain data. ....	78
Figure 4.4 - TSL used for verification analysis. ....	79
Figure 4.5 - X70 TSL's. ....	79
Figure 4.6 - SSY model FE mesh zones. ....	80
Figure 4.7 - SSY model FE mesh - half model.....	80
Figure 4.8 - SSY model mesh transition zone. ....	81
Figure 4.9 - SSY model ligament mesh.....	81
Figure 4.10 - SSY model verification using TH steel.....	82
Figure 4.11 - Non-dimensional crack growth resistance data examining the effect of the plateau size.....	82
Figure 4.12 - CTOA as a function of crack extension - X70.....	83

Figure 5.1 - SENT model dimensions - Not to scale. ....	92
Figure 5.2 - SENT model loading conditions - Not to scale.....	93
Figure 5.3 - SENT FE mesh zones.....	94
Figure 5.4 - SENT model FE mesh design. ....	95
Figure 5.5 - Crack tip triaxiality as a function of crack extension - X70. ....	96
Figure 5.6 - CTOA as a function of crack extension - X70.....	96
Figure 5.7 - Crack tip triaxiality as a function of crack extension – X100.....	97
Figure 5.8 - CTOA as a function of crack extension – X100. ....	97
Figure 6.1 - Geometry of DWTT model.....	106
Figure 6.2 - DWTT model notch tip simplification.....	107
Figure 6.3 - Mesh zones (half model).....	107
Figure 6.4 - DWTT model mesh (half model).....	108
Figure 6.5 – X70 quasi-static model CTOA as a function of crack extension. ....	109
Figure 6.6 - X100 quasi-static CTOA as a function of crack extension.....	109
Figure 6.7 - X70 FE and experimental quasi-static Load-LLD.....	110
Figure 6.8 – X100 FE and experimental quasi-static Load-LLD. ....	110
Figure 7.1 - X70 impact model CTOA as a function of crack extension. ....	124
Figure 7.2 - X70 quasi-static and updated impact TSL. ....	124
Figure 7.3 - X100 impact model CTOA as a function of crack extension. ....	125
Figure 7.4 - X100 quasi-static and updated impact TSL. ....	125
Figure 7.5 - X70 crack extension as a function of time. (FE updated TSL).....	126
Figure 7.6 – X100 crack extension as a function of time. (FE updated TSL) .....	126

Figure 7.7 - X70 FE and experimental impact Load-LLD (FE updated and non-updated TSL) .....	127
Figure 7.8 – X100 FE and experimental impact Load-LLD (FE updated and non-updated TSL) .....	127
Figure 7.9 - X70 crack extension as a function of time.....	128
Figure 7.10 - X70 crack extension as a function of time (continued).....	128
Figure 7.11 - X70 CTOA as a function of crack extension. ....	129
Figure 7.12 - X70 CTOA as a function of crack extension (continued).....	129
Figure 7.13 - X70 cohesive energy as a function of crack velocity.....	130
Figure 7.14 – X100 crack extension as a function of time. ....	130
Figure 7.15 – X100 crack extension as a function of time (continued).....	131
Figure 7.16 – X100 CTOA as a function of crack extension.....	131
Figure 7.17 – X100 cohesive energy as a function of crack velocity. ....	132
Figure 8.1 - Simplification of pipe to a tensile plate.....	150
Figure 8.2 - Plate model geometry.....	150
Figure 8.3 - Plate model loading conditions - first step.....	151
Figure 8.4 - Plate model loading conditions - second step. ....	151
Figure 8.5 - Plate model mesh zones. ....	151
Figure 8.6 - Plate model FE mesh design. ....	152
Figure 8.7 - Crack extension as a function of time - X70 excluding material rate hardening. .....	153
Figure 8.8 - CTOA as a function of crack extension - X70 excluding material rate hardening.....	153

Figure 8.9 - Crack extension as a function of time – X100 excluding material rate hardening.....	154
Figure 8.10 - CTOA as a function of crack extension – X100 excluding material rate hardening.....	154
Figure 8.11 - Crack extension as a function of time – X70 material rate hardening (no TSL update).....	155
Figure 8.12 - Crack extension as a function of time – X70 material rate hardening (TSL updated constant CTOA). ....	155
Figure 8.13 - CVDFR – X70 comparing quasi-static TSL to constant CTOA updated TSL. ....	156
Figure 8.14 - CVDFR – X70 comparing rate insensitive model to constant CTOA updated TSL. ....	156
Figure 8.15 – X70 cohesive energy as a function of crack velocity. ....	157
Figure 8.16 - Crack extension as a function of time - X100 material rate hardening (no TSL update).....	157
Figure 8.17 - Crack extension as a function of time – X100 material rate hardening (TSL updated constant CTOA). ....	158
Figure 8.18 – CVDFR – X100 comparing quasi-static TSL to constant CTOA updated TSL. ....	158
Figure 8.19 - CVDFR – X100 comparing rate insensitive model to constant CTOA updated TSL. ....	159
Figure 8.20 - X100 cohesive energy as a function of crack velocity.....	159
Figure 8.21 - Crack extension as a function of time - unscaled mass model.....	160

Figure 8.22 - Crack extension as a function of time – 1.5x density model. ....	160
Figure 8.23 - Crack extension as a function of time – 2x density model. ....	161
Figure 8.24 - Applied stress as a function of steady-state crack velocity. ....	161
Figure 8.25 - Crack extension and CTOA as function of time – 100 MPa models. ....	162
Figure 8.26 - Crack extension and CTOA as function of time - 200 MPa models. ....	162
Figure 8.27 - Crack extension and CTOA as function of time - 300 MPa models. ....	163
Figure 8.28 - Crack extension and CTOA as function of time - 400 MPa models. ....	163
Figure 8.29 - Crack extension and CTOA as function of time - 500 MPa models. ....	164

## Nomenclature

### *Latin Characters*

Symbol	Description	Units
$a_o$	Initial crack length	[ <i>mm</i> ]
$a$	Crack length	[ <i>mm</i> ]
$B$	Specimen thickness	[ <i>mm</i> ]
$C_1, C_2, n$	Johnson-Cook material constants	[–]
$CTOA$	Crack tip opening angle	[°]
$CV$	Crack velocity	[ <i>m/s</i> ]
$D$	Scalar damage variable	[–]
$E$	Young's modulus	[ <i>MPa</i> ]
$G$	Shear modulus	[ <i>MPa</i> ]
$g$	Cohesive element thickness	[ <i>mm</i> ]
$H$	Specimen daylight length	[ <i>mm</i> ]
$H^*$	SENT specimen clamped region length	[ <i>mm</i> ]
$h$	Cohesive element length	[ <i>mm</i> ]
$K$	Cohesive Stiffness	$\left[\frac{MPa}{mm}\right]$
$K_o$	Crack stress intensity factor at initiation	[ <i>MPa</i> √ <i>mm</i> ]
$K_r$	Crack stress intensity factor	[ <i>MPa</i> √ <i>mm</i> ]
$L$	Length	[ <i>mm</i> ]
$M$	Cohesive length adjustment parameter	[–]
$P$	Load	[ <i>N</i> ]
$R_o$	Plastic zone radius at crack initiation	[ <i>mm</i> ]
$r_i$	Optical method nodal distance	[ <i>mm</i> ]
$r$	SSY model radius	[ <i>mm</i> ]
$r_p$	Plastic rotation factor	[–]
$S$	Span	[ <i>mm</i> ]
$Q$	Temperature	[ <i>K</i> ]
$T_i$	Cohesive traction	[ <i>MPa</i> ]

$T_i^o$	Maximum cohesive traction	[MPa]
$t$	Time	[s]
$U_x$	SSY model nodal displacement in the x-axis	[mm]
$U_y$	SSY model nodal displacement in the y-axis	[mm]
$w$	Specimen width	[mm]
$x$	X component of displacement vector	[mm]
$Y$	Load-line displacement	[mm]
$y$	Y component of displacement vector	[mm]
$Z$	Non-dimensional compliance	[-]

*Greek Characters*

Symbol	Description	Units
$\alpha$	Johnson-Cook material constant	[-]
$\Gamma_o$	Cohesive Energy	[MPa – mm]
$\Delta$	Optical method separation	[mm]
$\delta$	Cohesive element separation	[mm]
$\varepsilon$	Mechanical Strain	$\frac{mm}{mm}$
$\dot{\varepsilon}$	Mechanical strain rate	$\left[ \frac{\left( \frac{mm}{mm} \right)}{s} \right]$
$\dot{\varepsilon}_p$	Plastic strain rate	$\left[ \frac{\left( \frac{mm}{mm} \right)}{s} \right]$
$\dot{\varepsilon}_o$	Reference strain rate	$\left[ \frac{\left( \frac{mm}{mm} \right)}{s} \right]$
$\zeta$	Slope of Ln (P/P <sub>max</sub> ) vs. (Y–Y <sub>max</sub> )/S	[-]
$\theta$	SSY model angle	[rad]
$\nu$	Poisson's ratio	[-]
$\rho$	Density	$\frac{Kg}{m^3}$
$\sigma$	Stress	[MPa]

*Subscripts*

Symbols	Description	Units
<i>cz</i>	Cohesive zone	[-]
<i>max</i>	Maximum	[-]
<i>n</i>	Normal direction	[-]
<i>s</i>	Shear direction	[-]
<i>t</i>	Tangential direction	[-]

## Acronyms

Acronym	Description
API	American Petroleum Institute
ASTM	American Society for Testing and Materials
CTOA	Crack Tip Opening Angle
CVDFR	Crack velocity – driving force relation
CZM	Cohesive Zone Model
DWTT	Drop Weight Tear Test
EPFM	Elastic Plastic Fracture Mechanics
FE	Finite Element
FEA	Finite Element Analysis
ISO	International Standards Organization
LEFM	Linear Elastic Fracture Mechanics
LLD	Load Line Displacement
NEB	National Energy Board
RA	Reduction of Area
SENT	Single Edge Notch Tension
SS-CTOA	Steady-state CTOA
SSY	Small Scale Yielding
S-SSM	Simplified Single Specimen Method
TSL	Traction-Separation Law
UTS	Ultimate Tensile Strength
YS	Yield Strength

## **Chapter 1: Introduction**

The use of pipelines for the transportation of natural gas and oil has been extensive over the past 80 years. Other forms of transportation include oil truck, oil tankers and railway tankers. The attraction to pipelines over other options stem from the reduced maintenance and operation costs. Moreover, pipelines do not have as significant carbon footprint as automotive transportation. Furthermore, based on the sheer amount of resources required to be transported, it is not economically feasible to transport it by vehicle or rail, especially over certain types of terrain. This has laid the foundation for the use of pipelines in the oil and natural gas industry. The extensive use of pipelines has produced a necessity to be able to properly design and confidently predict fracture arrest.

The most common causes of failures in pipelines include material processing defects such as internal and external surface flaws, and manufacturing defects typically associated with welding. Other common causes of failures in pipelines include stress corrosion cracking, fatigue, dents and over pressurizing. The National Energy Board (NEB) has published a report summarizing 39 pipeline ruptures in Canada between the years of 1992 – 2014 (National Energy Board, 2014). The cause of these ruptures varied from cracking, metal loss, external interference, material/manufacturing defects, and other causes. One notable example is the 1999 Enbridge rupture that resulted in 3123 m<sup>3</sup> of crude oil being leaked (National Energy Board, 2014). The results of these leaks can be catastrophic on the environment and the wildlife in the area. This makes the design and fracture assessment of pipelines of great importance.

In recent years, there have been massive improvements in the strength and toughness of steels used in the pipeline industry. Common examples include the American

Petroleum Institute (API) standard X70 and X100 steels. High toughness steels are preferred for many reasons; they exhibit a large amount of ductility prior to the initiation of a crack. Moreover, they also exhibit stable crack propagation prior to complete failure. In the pipeline industry there is currently a mismatch between the design methodology and characterization of the toughness of the materials being assessed for use. Ideally, axially flawed pipes would be assessed experimentally in full scale burst tests; however, those can prove to be very expensive and difficult to perform.

Historically, the Charpy V-notch energy was used to characterize the fracture resistance in pipeline steels; however, it has been found that the Charpy V-notch test is not applicable to high strength and high toughness steels (Duan, Zhou, Shim, & Wilkowski, 2010a). The drop weight tear test (DWTT) was introduced to provide a better measure of fracture resistance, as the specimen is closer in dimensions to the service size of the material to be examined. The fracture resistance of the material was quantified through the absorbed energy during the test. The DWTT is currently used for determining the fracture resistance of a material to an axial flaw in a pipe. Another fracture resistance parameter being developed in the pipeline industry is the crack tip opening angle (CTOA). The CTOA is currently being researched and is gaining traction as a fracture characterization parameter for high strength and high toughness steels. The CTOA design methodology is based on the notion that the CTOA is a material parameter, and can be used for material selection; however, examining the CTOA in a full scale pipe test poses a significant challenge. Lab test specimens such as the DWTT and the modified double cantilevered beam (MDCB) have been developed to determine the CTOA of materials. The intention of these specimens would be to determine the CTOA from a lab test specimen and use the

data for the design of the pipe (Horsley, 2003). However, there are still certain areas of the CTOA that require further investigation.

Fracture propagation in pipelines is a highly dynamic process, with crack velocities on the order of 200-500 m/s (Reuven, et al., 2008a). Understanding the effects of high loading rates on the toughness (CTOA) of pipeline steels is crucial for material selection and general design. The standard DWTT specimen induces crack velocities on the order of 8-30 m/s. Experimental data quantifying the effects of crack velocity on the CTOA of pipeline steels is minimal. Addressing the effect of dynamic fracture on the CTOA and CZM parameters is one of the main objectives of this thesis.

Furthermore, there is currently a discrepancy in the manner of loading in which the DWTT specimen is loaded compared to the nature of loading in a pipe. The DWTT specimens are used to assess toughness of axial cracks running in full-scale pipes. They are also a standard test specimen for the determination of the CTOA from pipeline steels (ASTM E3039-16, 2016). In the conventional test, the load is applied in bending, but in an actual pipeline, an axial crack is primarily loaded in tension. The assessment of loading mode under quasi-static loading conditions on the CTOA and the effect of higher loading rates on the CTOA are the main focus of this work. The main objectives of this work are outlined in the following section.

## 1.1 Thesis Objectives

The primary objectives of this thesis are to examine the effect of loading mode on the CTOA under quasi-static loading conditions, and to examine the effect of higher loading rates on the CTOA and CZM parameters of high strength pipeline steels. The main objective of the rate analysis was to assess the effect of crack velocity on the traction separation law (TSL) parameters, updating the cohesive zone model (CZM) parameters to produce a constant CTOA in the model. The materials of interest in this work are the API standard steels known as C2-X70, and C4-X100. The specific objectives of this thesis are outlined below.

1. Assemble a method by which to calibrate the parameters in a CZM based on the mechanical properties of the material.
2. Examine the effect of the plateau size in a TSL on the crack growth resistance data and the measured CTOA using a small scale yielding (SSY) model.
3. Examine the effect of loading mode on the CTOA under quasi-static loading conditions through comparing a bending model (DWTT) to a tensile model (SENT).
4. Assess the use of the experimental CTOA as a calibration parameter of the CZM under quasi-static loading conditions.
5. Compare the DWTT FE results to those obtained from experimentation under quasi-static and impact loading conditions. Specifically examine the load-load line displacement data, and crack velocity.

6. Study the effect of crack velocity on the CTOA using a rate independent cohesive zone model.
7. Examine the relation between the cohesive energy and crack velocity to produce a constant CTOA.
8. Study the effect of inertia and bulk material rate hardening on the fracture resistance data generated for the two curve method of a dynamic fracture model.

## **1.2 Thesis Outline**

The contents of this thesis are divided into nine chapters, with the simulations/results chapters divided into two parts. The first part presents simulations performed under quasi-static loading conditions (Chapters 4, 5, 6) the second part examines models under dynamic loading conditions (Chapters 7 and 8).

Chapters 2 and 3 present the literature review and background. Chapter 2 focuses on the development and use of the CZM, as well as background knowledge of the various topics required to understand the contents of this work. The mathematical framework of the cohesive zone model is presented in Chapter 3 along with the calibration method for the various parameters. Chapter 4 presents a study conducted on an SSY model specifically examining the effect of the shape of the traction separation law on ductile fracture. The effect of loading mode on the CTOA was assessed in Chapter 5 through comparing a tensile and bending specimen under quasi-static loading conditions. Chapter 6 examines and compares numerical data of a DWTT specimen under quasi-static loading conditions to experimental data. Chapter 7 examines the DWTT specimen under impact loading conditions. Chapter 8 examines a plate model derived as a simplified version of a pipe.

This analysis continues that of Chapter 7, with assessing the effect of loading rate on the CZM parameters based on a constant CTOA model. Furthermore, the plate model was used to assess the effect of inertia on the fracture resistance data and CTOA. The concluding remarks and recommendations for future work are presented in Chapter 9.

## **Chapter 2: Literature Review and Background**

This chapter presents a review of modelling efforts utilizing the cohesive zone model, as well as introduces fundamental concepts involved in CTOA based design. The literature review will focus on the history and the development of the CZM. An emphasis will be placed on the past and current modelling efforts of ductile fracture in pipeline steels. The sections devoted to the background will cover topics such as fracture toughness characterization, the CTOA, experimental methods with the DWTT, and the current design methodology for pipelines. In addition, pipeline steels will be introduced along with their implementation into the numerical model. Lastly, the motivation for each of the analyses performed in this work will be presented.

### **2.1 Modelling of Ductile Fracture using the Cohesive Zone Model**

A large amount of effort has been invested in developing and refining numerical modelling techniques for use with engineering materials. Specifically, in the field of fracture mechanics the implementation of numerical models allowed for the approximation of hundreds of stress intensity solutions, the investigation of elastic-plastic effects at the crack tip, and the study of crack propagation in structures (Anderson, 2011). The ability to study crack propagation is especially attractive for the pipeline industry to circumvent a large number of costly experimental investigations, such as full scale pipeline burst tests.

Two common crack propagation modelling techniques include a material damage model and the cohesive zone model. Material damage models involve designating certain elements within the model to experience damage and eventual failure throughout the analysis. These models often require very fine meshes to adequately capture the fracture

process, and can even face large numerical instabilities due to stiffness degradation. The cohesive zone model (CZM) is a phenomenological technique for modelling crack propagation. It is widely used for its simplicity, numerical stability, and ability to capture the fracture process with relatively large meshes. The CZM idealizes the fracture process to a relation between the cohesive stress and the current separation known as the traction separation law (TSL). The cohesive zone model was exclusively used for the analysis of ductile fracture in this work. The constitutive model of the CZM and the parameter calibration will be reviewed in Chapter 3.

The extent of yielding ahead of a notch tip was studied in the work of (Dugdale, 1960). In that work, a relation was developed, and validated through experimentation, between the extent of yielding ahead of a notch tip and the external applied load using the strip yield model and an ideal elastic-plastic material. The work demonstrated that the stress at the crack tip is limited by the yield stress. The framework of the modern CZM was proposed in the work of (Barenblatt, 1962) through the analysis of the strength of brittle materials using the Griffith theory of fracture. The strength of the material ahead of the crack tip was replaced with a cohesive law to approximate the debonding of atomic lattices. Furthermore, the cohesive stress distribution ahead of the crack tip was studied and it was found that the cohesive stress distribution at the crack tip is the highest and decreases ahead of the crack tip. The concept of the CZM was based on the assumption that the cohesive forces were acting on a length smaller than the ligament. This foundation paved the way for the use of the CZM as a fracture propagation modelling technique.

Since the proposal of the CZM, there have been many research efforts in the development of the model itself. Several of the aspects include the calibration of the model

parameters, the effect of the shape of the traction separation law, and the effect of the mesh sizing. The calibration of the model parameters has been extensively investigated for a multitude of engineering materials. Examination of the literature regarding the calibration aspect of the CZM is presented in Section 3.2.

From a modelling aspect the CZM, also referred to as the fictitious crack model, has been used to analyze many different materials and models. Much of the early implementation of the CZM was in the modelling of brittle materials such as a rock and concrete. In its earliest form, the CZM was applied through finite elements analysis (FEA) to examine crack propagation in a concrete bending specimen in the work of (Hillerborg, Modeer, & Peterson, 1976). This work demonstrated the ability of the CZM to be used with FEA to produce realistic crack initiation and propagation results. Moreover, Hillerborg commented on the ability of the model to produce results with the use of a coarse mesh, giving rise to the notion of a computationally efficient modelling technique.

The CZM has since been implemented to model crack propagation in ductile materials in the works of (Needleman, 1987), (Tvergaard & Hutchinson, 1992), (Tvergaard & Hutchinson, 1994), (Seigmund & Brocks, 2000), (Dunbar, 2011), and (Parmar, 2014). In the work of (Tvergaard & Hutchinson, 1992), the CZM was used to investigate the effect of the traction separation law on ductile fracture in a small scale yielding (SSY) model. The effect of several TSL parameters were examined and quantified through the effect on the crack growth resistance data. This work was extended upon in (Tvergaard & Hutchinson, 1994), where the SSY model was used to investigate the effect of T-stress on the crack growth resistance. The CZM has also been used to simulate delamination in adhesively bonded joints, composites structures and fiber-metal laminates. There are far

too many efforts utilizing the CZM to mention, a specific focus of the modelling aspect will be placed on efforts examining pipeline steels and DWTT specimens.

#### *DWTT Modelling with the CZM*

The CZM has been used extensively in the modelling of ductile fracture in small scale test specimens, most notably the DWTT specimen. This specimen has been analyzed at both quasi-static and dynamic loading rates for a variety of different materials.

In the work of (Dunbar, 2011) and (Parmar, 2014), 2-dimensional DWTT models of X70 and X100 were analyzed under quasi-static loading conditions. In those efforts, a specific focus was placed on the comparison of the measured CTOA with that of experimentation. The work of (Dunbar, 2011) specifically examined the ability of the CZM to predict the experimental CTOA. The work of (Parmar, 2014) furthered this research through examining the effect of T-stress on the CTOA. Both of these efforts only focused on simulations under quasi-static loading conditions. X70 was also analyzed using a 3-dimensional model at a quasi-static and impact loading rate in the work of (Shim, Mohammed, Wilkowski, & Duan, 2013). This effort focused on examining the load displacement data of the DWTT as well as examining the extent of tunneling in the crack front. The surface and mid-thickness CTOA's were also examined. X100 was examined using a 3-dimensional model in the work of (Cerrone, Wawrzynek, Nonn, Paulino, & Ingrassia, 2014). The use of X100 was in the verification of the implementation of the Park–Paulino–Roesler cohesive zone model.

A research group at the University of Alberta has been using the CZM to study the effects of dynamic fracture on the CTOA. The modelling efforts of (Ren & Ru, 2013) and

(Yu & Ru, 2015) are based on recreating the experimental results presented in the work of (Duan, Zhou, Shim, & Wilkowski, 2010b). In the aforementioned literature, a crack velocity dependence of the CTOA was developed experimentally using the modified DWTT specimen; this work is further discussed in Section 2.3.4. In the work of (Ren & Ru, 2013), a relationship between the cohesive energy and the CTOA is developed. This effort ignores the effect of rate hardening in the bulk material as well as assumes a speed dependent CTOA (CTOA decreases with increasing crack velocity) as deduced from the experiments of (Duan, Zhou, Shim, & Wilkowski, 2010b). The work of (Yu & Ru, 2015), extends upon the work of (Ren & Ru, 2013), with the inclusion of material rate hardening; however, this effort is still based on modelling the speed dependent CTOA. Furthermore, in both of these modelling efforts, the TSL was assumed to have an exponential degradation shape.

#### *Pipeline Modelling with the CZM*

A research group at Engineering Mechanics Corporation of Columbus (EMC<sup>2</sup>) has used the CZM to model ductile fracture in small diameter pipes. In the work of (Shim, Wilkowski, Rudland, Rothwell, & Merritt, 2008) small diameter pipes (152.4mm outer diameter) were examined under dynamic fracture using the cohesive zone model. This modelling effort was to validate an adjustment to the two curve method (TCM). An interesting aspect of this work was that the CZM parameters were based on calibrating to match the experimental crack velocity. In using the crack velocity as the calibration parameter, good agreement with the CTOA was observed. Most recently, the research

group extended their original work to larger diameter pipes (762mm outer diameter) examining different forms of mechanical crack arrestors (Uddin & Wilkowski, 2016).

## **2.2 Fracture Toughness Characterization of Pipeline Steels**

Historically, the toughness of pipeline materials was characterized by the Charpy V-notch energy (CVN); however, this specimen possesses some significant deficiencies, which prove it inadequate for emerging high toughness steels. The CVN requires a specimen significantly smaller and thinner than the application size of the material. Furthermore, the length of the Charpy ligament is not long enough for the crack to reach steady-state propagation. Lastly, it has been reported that testing high toughness materials with a Charpy test can often result in the specimen not completely breaking (Xu, Bouchard, & Tyson, 2004).

The drop weight tear test (DWTT) is a common mill test to determine the toughness of a material, which improves upon the CVN. This test induces fracture of a specimen through a three-point bend loading orientation. The fracture toughness is quantified through the absorbed energy of the DWTT specimen during impact. The DWTT allows for a larger specimen, often the thickness of the service part, to be tested thus yielding test data, which is more indicative to the application size. Moreover, the larger specimen allows for a longer ligament providing a better chance of steady-state fracture to occur. In addition to characterizing the toughness through the absorbed energy, this specimen also allows for the determination of the crack tip opening angle (CTOA) for a given material. The methods in which the CTOA can be determined experimentally are detailed in Sections

2.2.1 and 2.2.2. The CTOA is fast becoming a rival measure of fracture resistance for pipeline steels, and will be further discussed in the following section.

### **2.3 The Crack Tip Opening Angle (CTOA)**

The crack tip opening angle is the geometric angle produced between two newly formed crack faces during crack propagation, this is illustrated in Figure 2.1. The basic concept behind the CTOA is that a crack will propagate once the angle between the flanks created by a propagating crack reaches a certain value. The CTOA was first proposed in the work of (Rice & Sorensen, 1978) and has been gaining traction as a rival measurement of fracture resistance. The design methodology behind the CTOA is that it is a material property and can be used to describe fracture resistance. It has been shown that the CTOA will remain constant during crack propagation in pipeline steels (Wang & Shuai, 2012).

The CTOA has already been approved by the International Standards Organization (ISO) for the use of quantifying a metallic materials resistance to stable crack extension (ISO 22889, 2013). Moreover, the American Society of Testing and Materials (ASTM) have published a standard for measurement of CTOA. The CTOA methodology is currently being developed for use as a design criterion in the pipeline industry. This section will introduce the method in which the CTOA is measured, as well as discuss the effect of constraint and fracture velocity on the CTOA.

#### **2.3.1 CTOA Measurement - Optical Method**

The optical method is a common and convenient method for determining the surface CTOA as demonstrated in the work of (Darcis, McCowan, Wondhoff, McColskey,

& Siewert, 2008). The optical method involves examining images taken during the experiment and calculating the CTOA graphically. The optical method is discussed in detail in the work of (Darcis, McCowan, Wondhoff, McColskey, & Siewert, 2008) with a comparison of four different methods. Of the four methods presented, what was deemed as method 2 in the original work showed the most promise for accurate and repeatable determination of the CTOA and will be presented here.

This method does not directly include the use of the crack tip; it fits lines from behind the crack tip along the crack profile. This method is illustrated in Figure 2.1 and the CTOA is calculated from the following equation.

$$CTOA = \frac{\Delta_i - \Delta_o}{r_i} \quad \text{Eq. 2.1}$$

where  $CTOA$  is the crack tip opening angle,  $\Delta_i - \Delta_o$  is the relative vertical distance between two points along the flank, and  $r_i$  is the relative horizontal distance between the two points. Though this method is rather simple, it can be very time consuming to examine a large number of images. As well, it can only examine the surface CTOA of the specimen; to be used to examine the mid-thickness CTOA the specimen would be required to be cut through the mid-thickness.

In this work, 2-D plane strain models were used to investigate the effect of loading mode and crack velocity on the CTOA. The aforementioned method was used to determine the CTOA from the model's used in this work. The CTOA was measured by selecting two nodes behind the crack tip to create a distance vector along the flank. This vector was

defined in the global coordinate system and the components of the vector were used to calculate the CTOA as demonstrated in Eq. 2.2. The method is illustrated in Figure 2.2.

$$CTOA = 2 \left( \frac{CTOA}{2} \right) = 2 \left( \tan^{-1} \left( \frac{x}{y} \right) \right) \quad \text{Eq. 2.2}$$

where  $x$  is the distance component in the global X-axis, and  $y$  is the distance component in the Y-axis. The measurement technique was used to extract the CTOA from all models used in this work. The specific distance between the two nodes were 1-2 mm for the SSY model, SENT model and DWTT model. Due to the change in mesh size for the plate model, the distance was increased to 3-4 mm.

### 2.3.2 CTOA Measurement - Simplified Single Specimen Method

The single specimen method was first presented in the work of (Martinelli & Venzi, 1996) to provide a method for determining the CTOA of a DWTT specimen based on the load-displacement curve and material properties. This method was later modified to what is now called the simplified single specimen method (S-SSM) in the work of (Xu, Bouchard, & Tyson, 2007). The modifications eliminated the necessity for the estimation of the flow stress, and reduced the method to only requiring the load-displacement curve. Furthermore, the work of (Xu, Bouchard, & Tyson, 2007) extended the use of the S-SSM to pipeline steels. The method in which the CTOA is determined from the S-SSM is calculated from the equation below.

$$CTOA = \frac{8(r_p)}{\zeta} \left( \frac{180}{\pi} \right) [^\circ] \quad \text{Eq. 2.3}$$

where  $r_p$  is the rotation factor typically taken as 0.57 for high strength steels and 0.54 for low strength steels, and  $\zeta$  is defined as the slope of the natural logarithm function of the load-LLD curve, as defined by the equation below.

$$\zeta = \frac{\Delta \ln\left(\frac{P}{P_{max}}\right)}{\Delta \ln\left(\frac{Y}{Y_{max}}\right)} \quad \text{Eq. 2.4}$$

where  $P$  is the instantaneous load,  $P_{max}$  is the maximum load,  $Y$  is the LLD, and  $Y_{max}$  is the maximum LLD. The instantaneous load and LLD are taken in the steady-state portion of the load-LLD curve. Figure 2.3 and Figure 2.4 illustrate the method to evaluate the CTOA. In (Xu, Tyson, & Bouchard, 2009) and (Xu S. , Tyson, Eagleson, & Park, 2011) the ability of the S-SSM to predict the CTOA was validated for X70 and X100. It is most noticeable how the S-SSM predicts the mid-thickness CTOA. Recently, the S-SSM has been accepted as a standard method for determining the CTOA of pipeline steels and published in (ASTM E3039-16, 2016)

The S-SSM was used to determine the experimental CTOA of the materials examined in this work. The experimental CTOAs of the materials examined in this work were published in the work of (Xu S. , et al., 2010)

### **2.3.3 Effect of T-Stress (Constraint) on the CTOA**

T-stress is a non-singular stress term acting parallel to the crack plane of elastic-plastic solid materials (Anderson, 2011). T-stress is one of many parameters that can be used to quantify the level of constraint near the crack tip. The effect of T-stress on ductile

crack growth resistance was investigated in the work of (Tvergaard & Hutchinson, 1994). It was found that crack growth resistance was increased for increasingly negative values of T-stress, and was not significantly affected for increasingly positive values of T-stress in a plane strain model.

The effect of T-stress on the CTOA under quasi-static loading conditions was examined in the work of (Parmar, 2014). The effect of T-stress was systematically assessed through the examination of a modified boundary layer model. This model allowed for the incremental inclusion of positive and negative T-stress at the crack tip. It was found that the level of constraint at the crack tip had a secondary effect on the CTOA.

This work will follow up on the results of (Parmar, 2014) through the comparison of a tensile model and a bending model under quasi-static loading conditions. It is well known that the loading mode is a significant factor affecting the level of constraint at the crack tip. A tensile model will produce a negative T-stress decreasing the level of crack tip constraint, while a bending model will produce a positive T-stress increasing the level of crack tip constraint (Parmar, 2014).

#### **2.3.4 Effect of crack velocity on the CTOA**

The effect of crack velocity on the CTOA was investigated experimentally in the work of (Duan, Zhou, Shim, & Wilkowski, 2010a) and (Duan, Zhou, Shim, & Wilkowski, 2010b), using a standard and modified back-slot DWTT specimen. Typically, a standard DWTT would induce a crack velocity on the order of 8-30 m/s, depending on the apparatus. The modified back-slot specimen utilizes a larger specimen with an alteration to the ligament which can induce higher velocities on the order of 80 m/s. The results of this

study demonstrated that the CTOA decreased with increasing crack velocity. In the work of (Shim, Mohammed, Wilkowski, Duan, & Ferguson, 2014) the modified back-slot specimen was compared to the standard DWTT specimen. In this study, it was shown that the larger crack velocity of the modified specimen is indicative of unstable fracture. This fracture mode is not representative of the fracture behavior present in a long running crack in a pipe. Thus the original authors advised caution when using the experimental CTOA data from the modified DWTT specimen.

A dynamic loading apparatus was developed in the work of (Reuven, et al., 2008a) to induce higher fracture velocities in a modified double cantilevered beam (MDCB) specimen. X65 and X100 were examined in this work. The results of this study were published in the work of (Reuven, et al., 2008b). It was reported that there was no significant change in CTOA for either material at the displacement rates examined. It was recorded that a maximum fracture velocity of 29 m/s was achieved. The result of a rate independent CTOA was also recorded in the work of (Xu S. , et al., 2010). In this work, DWTT specimens of X70 and X100 were examined under quasi-static and impact loading conditions. The results did not display any significant difference between the CTOA for the two loading rates for either material. The effect of loading rate was further investigated in the work of (Xu, Sollen, Liang, Zavadil, & Tyson, 2014) with C7-X65 and C8-X70 steels. The results did not present any significant difference between the CTOA of the two loading rates for both steels. All experimental efforts produced crack velocities between 8-30 m/s, significantly lower than the expected fracture velocity in a pipeline.

There have been no experimental measurements of CTOA for velocities relevant to pipeline fracture (200-500 m/s). Though the exact nature of the CTOA is not completely

known with respect to crack velocity, there has been noticeable success with assuming the CTOA is constant with respect to crack velocity. In the work of (Ben Amara, 2015), a model using the critical CTOA criterion was implemented to study ductile fracture in a pipe geometry. The results show great promise in the ability of the model to produce essential design data such as the material resistance curve from the Battelle Two Curve Method (BTCM). Thus the idea of a constant CTOA model was adopted, such that the CZM parameters were chosen to produce a constant CTOA. The concept is to examine the effect of crack velocity on the TSL to produce a constant CTOA within the model.

#### **2.4 Pipeline Design for Dynamic Fracture**

The traditional and long standing design methodology for full scale pipelines is known as the Battelle Two Curve Method (TCM) (Maxey, Keifner, & Eiber, 1976). The TCM is a design criterion for predicting fracture speed and minimum arrest toughness for a full scale pipeline. This method empirically incorporates many influences such as fracture toughness, gas decompression behavior and backfill conditions. The basic idea behind the use of the TCM is to compare the material resistance curve to the gas decompression curve and examine the intersection points. A generic example is illustrated in Figure 2.5.

The two intersection points are marked 'A' and 'B' in Figure 2.5. The intersection point marked 'A' represents a stable equilibrium point. At this point if the pressure decreases the crack runs ahead faster than the gas can escape, and the pressure rises. If the pressure increases the opposite occurs. The intersection point 'B' represents an unstable equilibrium. If the pressure drops the gas escapes faster than the crack can propagate, and

should the pressure continue to drop this would lead to rapid arrest (Revie, 2015). One notable trend of the material resistance curve is the sharp upswing in driving force as the crack velocity is increased in the material resistance curve. Maxey empirically proposed that the cause of this upswing was to propagate a plastic wave ahead of the crack tip (Maxey, Keifner, & Eiber, 1976). It has also been proposed that the upswing is due to an inertial effect due to the requirement to accelerate the material ahead of the crack tip (Revie, 2015). A discussion of the effect of inertia on the toughness of materials is presented in the work of (Xu, Tyson, & Rothwell, 2015). In the discussion, it is stated that due to the effect of inertia large scale simulations will require an increase in driving force to increase crack velocity, with no change in the local toughness. This work will address the effect of inertia on a large scale model, with a rate independent fracture process zone.

It has been noted that the TCM in its original form is inadequate to be used for designing with the current high strength and high toughness materials (Duan, Zhou, Shim, & Wilkowski, 2010a). Historically, the material resistance data of the TCM was correlated through the use of CVN for materials exhibiting low levels of toughness. However, as shown in (Higuchi, Makino, & Takeuchi, 2009), characterization by use of the CVN for new steels, such as X70 and X100, prove to be inadequate due to the high level of toughness. This lead to the original TCM dangerously under predicting the crack propagation speed, as demonstrated in the work of (Ben Amara, 2015). To rectify this poor characterization, (Higuchi, Makino, & Takeuchi, 2009) attempted to relate the DWTT absorbed energy to the materials resistance data and adjust the original TCM. Attempts have been made to adjust the TCM based on the Charpy energy, see (Demofonti, Mannucci, Hillenbrand, & Harris, 2004) and (Leis, Eiber, Carlson, & Gilroy-Scott, 1998). Other

attempts have been made to refine the TCM for newer steels, see (Higuchi, Makino, & Takeuchi, 2009) and (Ben Amara, 2015). A comparison of these methods is presented in (Ben Amara, 2015).

In the work of (Ben Amara, 2015), a full scale pipe model was examined with the fracture process being modelled using the constant CTOA criterion. In the constant CTOA criterion, the CTOA is specified as the crack propagation condition, meaning that the crack will not advance until the newly formed crack face, a certain distance behind the crack tip, forms a specified angle. However, validation of many of these models has been hindered due to limited experimental data from full scale tests.

In this work, a tensile plate model will be developed as a simplification of the pipe geometry. The specific use of this model will be to examine the effect of inertia on the material resistance curve. Due to the change of the model geometry, the material fracture resistance data from this work will be referred to as the crack velocity driving force relation (CVDFR). For the purposes of this work the term ‘driving force’ is used with reference to the applied stress in the model.

## **2.5 DWTT Experimental Methods**

The experimental tests of the DWTT specimens used in this work were conducted at CanmetMATERIALS. The specimens tested were all manufactured to the dimensions outlined in the ASTM standard E436-03 (ASTM E436-03, 2014), illustrated in Figure 2.6. The quasi-static tests were conducted on a three-point bend fixture with anti-buckling jigs in a universal servo-hydraulic machine. The apparatus used is depicted in Figure 2.7. The hydraulic system would slowly press the hammer into the top of the specimen until the

crack propagated through the ligament. The instantaneous load (reaction load on the hammer) and displacement of the hammer (referenced from the top of the specimen downward) were recorded during the experiment. The correlation of these two measured quantities generated the load-load line displacement (Load-LLD) data.

The impact tests were performed using a drop weight tower, illustrated in Figure 2.8. The drop tower guided the impact of a 1152 kg hammer propelled at 5.1 m/s into the specimen. The drop weight tower has a kinetic energy capacity of 15 kJ and was connected to a high speed data acquisition system developed at CanmetMATERIALS. This system recorded the instantaneous load and load-line displacement of the hammer.

The Load-LLD data was corrected for compliance by the author's predecessors for X70 and X100, see (Dunbar, 2011) and (Parmar, 2014), using the non-dimensional analysis technique from (Anderson, 2011). The compliance correction analysis adjusts the experimental data accounting for elastic deformation in the testing structure, as well as the local indentation of the hammer in the specimen. This analysis involved correcting the experimental LLD data using an elastic error constant. The elastic error constant is a constant offset of the experimental slope (elastic region) and the desired slope. For a full overview of the analysis it is recommended to review the work of (Parmar, 2014). The elastic error constants, calculated in the previous works, were 90 kN and 132.3 kN for X70 and X100, respectively. The compliance corrected quasi-static and impact loading rate experimental load-load line displacement (Load-LLD) curves for X70 and X100 can be seen in Figure 2.9 and Figure 2.10, respectively. These experimental load-LLD curves will be revisited later for comparison with the FE data.

The CTOA of the materials examined in this work were determined by the S-SSM and are recorded in the work of (Xu S. , et al., 2010). Specifically, X70 had a CTOA of 12.4° (quasi-static) and 12.5° (impact). X100 had a CTOA of 10.4° (quasi-static) and 9.7° (impact).

## **2.6 Pipeline Steels**

The strength of steels used in the natural gas and pipeline industry has greatly increased over the past 60 years. Most existing pipelines were constructed using API standard steels ranging from X46 - X70 (the number indicates the yield strength in ksi) (Xu & Tyson, 2015). Currently, there are stronger steels such as X80 and X100 commercially available with even higher grades, such as X120, in development. The introduction of these higher strength steels is beneficial for a multitude of reasons. The higher strength allows for thinner wall thickness to be used, reducing the weight, installation cost, and amount of material required.

In this section the materials utilized throughout this work are presented along with their chemical composition, mechanical properties, stress-strain (SS) relationship, strain rate dependence and implementation in the numerical model. The two materials examined are API standard C2-X70 and C2-X100 pipeline steels. Both materials are high toughness steels, X70 is a high-strength steel, with a yield strength of 576 MPa, while X100 is an extra high strength steel with a yield strength of 805 MPa. The chemical composition of each steel is presented in Table 2.1.

### 2.6.1 Stress-Strain Relationship of Pipeline Steels

The stress-strain relationship for the line pipe steels were determined from a uniaxial tensile tests performed at CanmetMATERIALS (Xu S. , 2016a). The testing apparatus is equipped with a data acquisition system which measures the displacement and the instantaneous tensile load. From this data the engineering and true stress and strain were then calculated. The average tensile mechanical properties of the two steels are summarized in Table 2.2, and the quasi-static engineering stress-strain curves are illustrated in Figure 2.11. The quasi-static true stress-strain curves are illustrated in Figure 2.12.

### 2.6.2 Effect of Strain Rate on The Strength of Pipeline Steels

The effect of strain rate on the strength of the materials examined in this work was characterized experimentally in the work of (Xu & Tyson, 2015). In that work, various pipeline steels ranging from X70 to X120 were tested in a uniaxial tensile test, and it was found that they obeyed the master curve constitutive equation as shown below.

$$\sigma = \sigma_{(Quasi-static, 22^{\circ}C)} + \sigma_{(Dynamic)}$$
$$\sigma = \sigma_{(Quasi-static, 22^{\circ}C)} + \left( 27.86 - 0.00393 * Q * \ln \left( \frac{10^8}{\dot{\epsilon}} \right) \right)^2 \quad \text{Eq. 2.5}$$

Where  $\sigma_{(Dynamic)}$  is the thermal and dynamic stress term in MPa,  $Q$  is the temperature in kelvin,  $\sigma_{(Quasi-static, 22^{\circ}C)}$  is the quasi-static stress at room temperature in MPa, and  $\dot{\epsilon}$  is the mechanical strain rate in  $s^{-1}$ . In the work of (Xu & Tyson, 2015), a maximum strain rate of  $1 s^{-1}$  was assessed experimentally. Other work has been completed examining the

ability of Eq. 2.5 to model the response of steels. One notable use of Eq. 2.5 was in the work of (Tanguy, Besson, Piques, & Pineau, 2005) where it was observed that the yield strength of an A508 steel could be modelled well by Eq. 2.5 at strain rates as high as 4000 s<sup>-1</sup>.

In many commercial finite element codes several constitutive material models are implemented, such as the Johnson-Cook equation and the Zerilli-Armstrong relation. Both of these models are examined in depth in the work of (Valentin, Magain, Quik, Labibes, & Albertini, 1997). The Johnson-Cook relation is a commonly used FEA material model shown below (Johnson & Cook, 1983).

$$\sigma = \sigma_{(Quasi-static, 22^{\circ}C)} (1 + C_1 \varepsilon_p)^n \left[ 1 + C_2 \ln \left( \frac{\dot{\varepsilon}_p}{\dot{\varepsilon}_0} \right) \right] \left[ 1 - \left( \frac{Q - Q_R}{Q_M - Q_R} \right)^\alpha \right] \quad \text{Eq. 2.6}$$

Where the first bracket describes the work hardening term;  $C_1$  and  $n$  are material constants, and  $\varepsilon_p$  is the equivalent plastic strain. The square bracket describes the rate dependence, where  $C_2$  and  $\alpha$  are material constants,  $\dot{\varepsilon}_p$  is the plastic strain rate,  $\dot{\varepsilon}_0$  is the reference rate,  $Q_R$  is the reference temperature, and  $Q_M$  is the material melting temperature. The Johnson-Cook equation is empirically based. The most common method of implementing this model is through trial and error adjusting the material parameters to match experimental data. The large number of terms required for the model does not make it ideal for applying to a large number of materials. As well, the rate term is linearly proportional to the  $\ln(\dot{\varepsilon})$ , as opposed to the quadratic relation present in Eq. 2.5. In the work of (Xu & Tyson, 2015), it was shown that the quadratic relation to the rate term in the rate parameter provided a better approximation of the stress over a wider range of strain rates and temperatures, when

compared to the Johnson-Cook relation. For these reasons the Johnson-Cook model was not used in this work.

The present effort made use of Eq. 2.5 for its simplicity and applicability to multiple materials without the tedious calibration of a large amount of terms. The equation does include a temperature term, but it was set to room temperature (295 K) as this work does not consider any effect of temperature change.

### **2.6.3 Implementation of the Material Model in ABAQUS**

The material plasticity model was implemented into ABAQUS using the tabular plastic stress data method. This method assumes the material obeys an isotropic hardening rule. With the use of this method, the linear elastic region of the tensile stress-strain curve was modelled solely based on the Young's modulus and Poisson's ratio. The tensile experimental true stress and plastic strain data was dictated in a tabular manner into the plasticity model. As specific data points are dictated, the material model will linearly interpolate between specified points (ABAQUS, 2014). The true stress-plastic strain data was determined from experimental stress-strain data (Xu S. , 2016a).

The effect of rate hardening was implemented using the same tabular method. Another function is to define a strain rate along with the true stress and plastic strain data in a tabular format. The stress was determined using the equation presented in Eq. 2.5. Again, since discrete data points are required, the program will linearly interpolate between specified points and rate ranges. Due to the large number of data points required for the rate dependence the values used will not be presented. However, the strain rates which they were evaluated for will be. The rate stress term as a function of strain rate, from Eq.

2.5, is shown in Figure 2.13. As can be seen with strain rates below  $1000 \text{ s}^{-1}$  the relation is highly non-linear, with an increasingly linear profile developing after  $1000 \text{ s}^{-1}$ . The rates at which the dynamic stress term was defined in the rate plasticity model are listed in Table 2.4. The rates were chosen such that the change in strength was in the range of 5-20 MPa, these values were chosen based on trial and error, and minimizing the amount of interpolation required.

The material elasticity parameters utilized in all models are presented in Table 2.3, these values were determined from the uniaxial tensile tests (Xu S. , 2016a). The quasi-static true stress and plastic strain data for the X70 and X100 steels are tabulated in Table 2.5 and Table 2.6, respectively. The true stress and true strain data is also plotted in Figure 2.12.

#### **2.6.4 Verification of the Material Model in ABAQUS**

To verify the implementation of the material model, a model of a 3-D unit cell was developed and simulated at various loading rates. The unit cell geometry is shown in Figure 2.14. The dimensions were  $1\text{mm} \times 1\text{mm} \times 1\text{mm}$ . The boundary conditions are shown on the model in Figure 2.14. The boundary conditions involved constraining the bottom surface in the Y direction, constraining the bottom edge parallel to the Z-axis in the X direction, and vice versa with the bottom edge in the Z direction. The load was applied to the top surface through a displacement for the quasi-static model and a velocity for the higher loading rates.

The material model was verified by examining the stress and the strain for the unit cell model at three different loading rates, namely, quasi-static,  $1 \text{ s}^{-1}$ , and  $10 \text{ s}^{-1}$ . The true

stress and true strain are plotted for X70 and X100 in Figure 2.15 and Figure 2.16, respectively. As can be seen the results of the numerical model are in good agreement with the experimental/prescribed data set. This verifies the implementation of the material model.

## **2.7 Motivation for the Current Work**

Fracture propagation models are extensively used in engineering as a means to circumvent costly experimental tests, as well as to acquire data which cannot be recorded experimentally. The CZM is a useful, computationally efficient, and numerically stable tool for modelling ductile fracture. The CZM was implemented to analyze ductile fracture in various specimens in this work. The motivation for each analysis and how they contribute to the overall objectives is presented in this section.

### *Calibration of the TSL (Chapter 3)*

Literature was examined and the most promising methods for the calibration of a CZM for pipeline steels were assembled.

### *Effect of the TSL Shape on Crack Growth Resistance and Measured CTOA (Chapter 4)*

The shape of the TSL has been extensively investigated as will be discussed in Section 3.2.2. However, no literature has been published examining the effect of the plateau size in the trapezoidal TSL shape for the same parameters. Furthermore, the TSL shape was examined to assess the effect of changing the shape based on the propagation rate to provide insight for the dynamic chapters later in this work.

### *Effect of Loading Mode on the CTOA under Quasi-Static Loading Conditions (Chapter 5)*

In the pipeline industry, DWTT specimens are used to assess toughness of axial cracks in pipes. In the conventional test the load is applied in a three point bend loading mode, but in an actual pipeline an axial crack is loaded in tension. The purpose of this analysis was to examine the transferability of the CTOA from a bending loading mode to a tensile loading mode. This analysis also examines the effect of constraint on the CTOA, as the DWTT specimen would represent a condition of high constraint and the clamped SENT specimen would represent low constraint.

### *Comparison of DWTT FE Results with Experiments (Chapter 6 and 7)*

In the work of (Dunbar, 2011) and (Parmar, 2014), DWTT models were developed and compared to experimental results for X70 and X100 under quasi-static loading conditions. In both of these efforts the bilinear TSL was used to describe the fracture process. This work assumes a trapezoidal TSL shape and examines the dynamic loading conditions of the impact loading rate. The purpose of these analyses was to assess if the trapezoidal TSL can re-produce the experimental Load-LLD data, and the fracture velocity of the impact specimen. Moreover, these analyses also assess the use of the CTOA as a calibration parameter for the quasi-static CZM and update for higher loading rates.

### *Effect of Loading Rate on the CTOA (Chapter 7 and 8)*

As discussed in Section 2.3.4, the effect of loading rate on the CTOA is largely unknown at crack velocities above 100 m/s. The ability of the CZM to be used as a

predictive tool will be assessed through a comparison with DWTT experimental data under quasi-static and impact loading conditions. The influence of crack velocity on the cohesive energy is assessed for the TSL based on matching the experimental CTOA. The motivation of the examination of the crack velocity on the cohesive energy would be to provide insight for the development of a rate dependence term in the CZM to produce a constant CTOA model. Typically, a constant CTOA criterion model must be implemented in an implicit numerical solver. Some implicit solvers do not capture dynamic effects, such as inertia. The CZM can be implemented with an explicit numerical solver which captures all dynamic effects.

*Effect of Inertia on the Material Resistance Data and CTOA (Chapter 8)*

As discussed in Section 2.4, the cause of the sharp upswing of the material resistance data used in the TCM is largely unknown. The use of this analysis will be to examine the effect of inertia on the material resistance curve, or CVDFR for this work. Furthermore, this analysis will also examine the effect of utilizing a mass scaling technique on the CTOA.

**Table 2.1 - Chemical composition of X70 and X100 (%wt.) (Xu & Tyson, 2015).**

Steel	C	Mn	Si	Al	Nb	Ti	Cu	Cr	Ni
X70	0.04	1.56	0.24	0.039	0.069	0.013	0.31	0.07	0.11
X100	0.06	1.75	0.06	0.012	0.045	0.008	0.28	0.028	0.13
Steel	P	S	Mo	Ca	Sn	B	N	Ce	V
X70	0.01	<0.009	0.2	0.0021	0.014	0.0003	0.008	0.001	0.003
X100	<0.002	0.009	0.21	-	<0.002	<0.0005	0.006	-	0.0045

**Table 2.2 – Average tensile mechanical properties of X70 and X100 (2-3 trials) (Xu & Tyson, 2015).**

Steel	Yield Stress (MPa)	UTS (MPa)	Elongation (%)	RA (%)
X70	576	650	29.5	78.1
X100	805	853	19.7	76.3

**Table 2.3 - Simulation material model parameters (ABAQUS input).**

Material	Modulus of Elasticity $E$ (GPa)	Yield Stress - $\sigma_y$ (MPa)	Poisson's Ratio $\nu$	Density $\rho$ (kg/m <sup>3</sup> )
X70	195.4	576	0.3	7850
X100	203.2	805	0.3	7850

**Table 2.4 - Strain rates and dynamic stress terms from Eq. 2.5.**

Strain Rate (s <sup>-1</sup> )	Dynamic Stress Term (MPa)	Strain Rate (s <sup>-1</sup> )	Dynamic Stress Term (MPa)	Strain Rate (s <sup>-1</sup> )	Dynamic Stress Term (MPa)
0.0074	0.52	70	129.36	1000	209.30
0.1	14.09	100	138.97	1250	216.88
0.4	28.79	200	158.63	1500	223.17
1	41.37	300	170.74	2000	233.28
2	52.39	400	179.60	2500	241.28
6	72.52	500	186.62	3000	247.91
10	82.99	600	192.46	4000	258.56
15	91.81	700	197.47	5000	266.98
30	107.91	800	201.86	6000	273.95
50	120.61	900	205.77		

**Table 2.5 - X70 Quasi-static true stress - plastic strain data. (ABAQUS input)**

True stress (MPa)	Plastic strain								
576	0	674.3	0.0609	915.4	0.25792	1292.4	0.5659	1669.5	0.8741
579.6	0.0019	676.8	0.0629	927.6	0.26786	1304.6	0.5759	1681.6	0.8840
583.1	0.0039	679.2	0.0649	939.7	0.27779	1316.7	0.5858	1693.8	0.8939
586.7	0.0059	681.6	0.0669	951.9	0.28773	1328.9	0.5958	1705.9	0.9039
590.3	0.0078	684.1	0.0689	964	0.29767	1341.1	0.6057	1718.1	0.9138
593.8	0.0098	686.5	0.0708	976.2	0.30761	1353.2	0.6156	1730.3	0.9238
597.4	0.0118	688.9	0.0728	988.4	0.31755	1365.4	0.6256	1742.4	0.9337
601	0.0138	691.4	0.0748	1000.5	0.32748	1377.6	0.6355	1754.6	0.9436
604.5	0.0158	693.8	0.0768	1012.7	0.33742	1389.7	0.6454	1766.8	0.9536
608.1	0.0177	696.2	0.0788	1024.9	0.34736	1401.9	0.6554	1778.9	0.9635
611.7	0.0197	698.6	0.0808	1037	0.3573	1414	0.6653	1791.1	0.9734
615.2	0.0217	701.1	0.0828	1049.2	0.36723	1426.2	0.6753	1803.2	0.9834
618.8	0.0237	703.5	0.0848	1061.3	0.37717	1438.4	0.6852	1815.4	0.9933
622.4	0.0257	705.9	0.0867	1073.5	0.38711	1450.5	0.6951	1827.6	1.0033
625.9	0.0277	708.6	0.0889	1085.7	0.39705	1462.7	0.7051	1839.7	1.0132
629.5	0.0296	720.8	0.0989	1097.8	0.40699	1474.9	0.7150	1851.9	1.0231
633.1	0.0316	733	0.1088	1110	0.41692	1487	0.7249	1864.1	1.0331
636.6	0.0336	745.1	0.1187	1122.2	0.42686	1499.2	0.7349	1876.2	1.0430
640.2	0.0356	757.3	0.1287	1134.3	0.4368	1511.3	0.7448	1888.4	1.0529
643.8	0.0376	769.4	0.1386	1146.5	0.44674	1523.5	0.7548	1900.5	1.0629
647.3	0.0395	781.6	0.1486	1158.6	0.45667	1535.7	0.7647	1912.7	1.0728
650	0.0410	793.8	0.1585	1170.8	0.46661	1547.8	0.7746	1924.9	1.0828
652.4	0.0430	805.9	0.1684	1183	0.47655	1560	0.7846	1937	1.0927
654.9	0.0450	818.1	0.1784	1195.1	0.48649	1572.2	0.7945	1949.2	1.1026
657.3	0.0470	830.3	0.1883	1207.3	0.49643	1584.3	0.8045	1961.4	1.1126
659.7	0.0490	842.4	0.1982	1219.5	0.50636	1596.5	0.8144	1973.5	1.1225
662.2	0.0510	854.6	0.2082	1231.6	0.5163	1608.6	0.8243	1985.7	1.1324
664.6	0.053	866.7	0.2181	1243.8	0.52624	1620.8	0.8343	1997.8	1.1424
667	0.0549	878.9	0.2281	1255.9	0.53618	1633	0.8442	2010	1.1523
669.5	0.0569	891.1	0.2380	1268.1	0.54611	1645.1	0.8541	2022.2	1.1623
671.9	0.0589	903.2	0.2479	1280.3	0.55605	1657.3	0.8641	2034.3	1.1722

**Table 2.6 – X100 Quasi-static true stress - plastic strain data. (ABAQUS input)**

True stress (MPa)	Plastic strain								
805.0	0.0000	897.2	0.0382	1537.9	0.5075	2276.1	1.0475	3014.3	1.5875
811.6	0.0011	897.8	0.0391	1558.5	0.5225	2296.6	1.0625	3034.8	1.6025
815.0	0.0019	898.6	0.0400	1579.0	0.5375	2317.1	1.0775	3055.3	1.6175
817.2	0.0027	900.0	0.0407	1599.5	0.5525	2337.6	1.0925	3075.8	1.6325
819.9	0.0039	901.2	0.0418	1620.0	0.5675	2358.1	1.1075	3096.3	1.6475
822.3	0.0048	901.6	0.0425	1640.5	0.5825	2378.7	1.1225	3116.8	1.6625
825.7	0.0059	922.8	0.0575	1661.0	0.5975	2399.2	1.1375	3137.3	1.6775
827.4	0.0065	943.3	0.0725	1681.5	0.6125	2419.7	1.1525	3157.8	1.6925
831.1	0.0076	963.8	0.0875	1702.0	0.6275	2440.2	1.1675	3178.3	1.7075
832.8	0.0083	984.3	0.1025	1722.5	0.6425	2460.7	1.1825	3198.9	1.7225
835.4	0.0092	1004.8	0.1175	1743.0	0.6575	2481.2	1.1975		
836.7	0.0098	1025.3	0.1325	1763.5	0.6725	2501.7	1.2125		
839.6	0.0108	1045.8	0.1475	1784.0	0.6875	2522.2	1.2275		
843.1	0.0118	1066.3	0.1625	1804.5	0.7025	2542.7	1.2425		
845.6	0.0126	1086.8	0.1775	1825.0	0.7175	2563.2	1.2575		
847.8	0.0132	1107.3	0.1925	1845.5	0.7325	2583.7	1.2725		
849.7	0.0142	1127.8	0.2075	1866.0	0.7475	2604.2	1.2875		
851.5	0.0148	1148.4	0.2225	1886.5	0.7625	2624.7	1.3025		
854.3	0.0158	1168.9	0.2375	1907.0	0.7775	2645.2	1.3175		
855.9	0.0164	1189.4	0.2525	1927.5	0.7925	2665.7	1.3325		
858.2	0.0172	1209.9	0.2675	1948.0	0.8075	2686.2	1.3475		
859.8	0.0179	1230.4	0.2825	1968.6	0.8225	2706.7	1.3625		
862.4	0.0191	1250.9	0.2975	1989.1	0.8375	2727.2	1.3775		
864.9	0.0201	1271.4	0.3125	2009.6	0.8525	2747.7	1.3925		
866.4	0.0208	1291.9	0.3275	2030.1	0.8675	2768.2	1.4075		
867.8	0.0214	1312.4	0.3425	2050.6	0.8825	2788.8	1.4225		
870.0	0.0223	1332.9	0.3575	2071.1	0.8975	2809.3	1.4375		
871.0	0.0229	1353.4	0.3725	2091.6	0.9125	2829.8	1.4525		
886.9	0.0315	1373.9	0.3875	2112.1	0.9275	2850.3	1.4675		
887.5	0.0321	1394.4	0.4025	2132.6	0.9425	2870.8	1.4825		
889.4	0.0330	1414.9	0.4175	2153.1	0.9575	2891.3	1.4975		
890.7	0.0336	1435.4	0.4325	2173.6	0.9725	2911.8	1.5125		
891.4	0.0345	1455.9	0.4475	2194.1	0.9875	2932.3	1.5275		
893.0	0.0354	1476.4	0.4625	2214.6	1.0025	2952.8	1.5425		
894.1	0.0363	1496.9	0.4775	2235.1	1.0175	2973.3	1.5575		
895.9	0.0374	1517.4	0.4925	2255.6	1.0325	2993.8	1.5725		

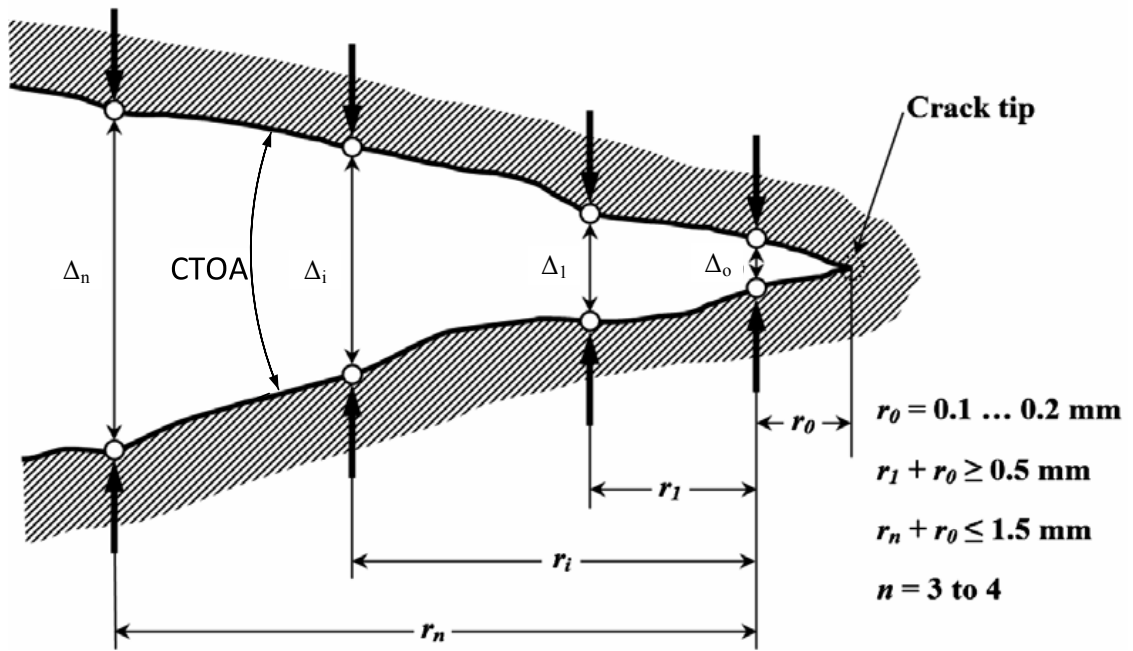


Figure 2.1 - CTOA optical measurement (Darcis, McCowan, Wondhoff, McColskey, & Siewert, 2008)(modified).

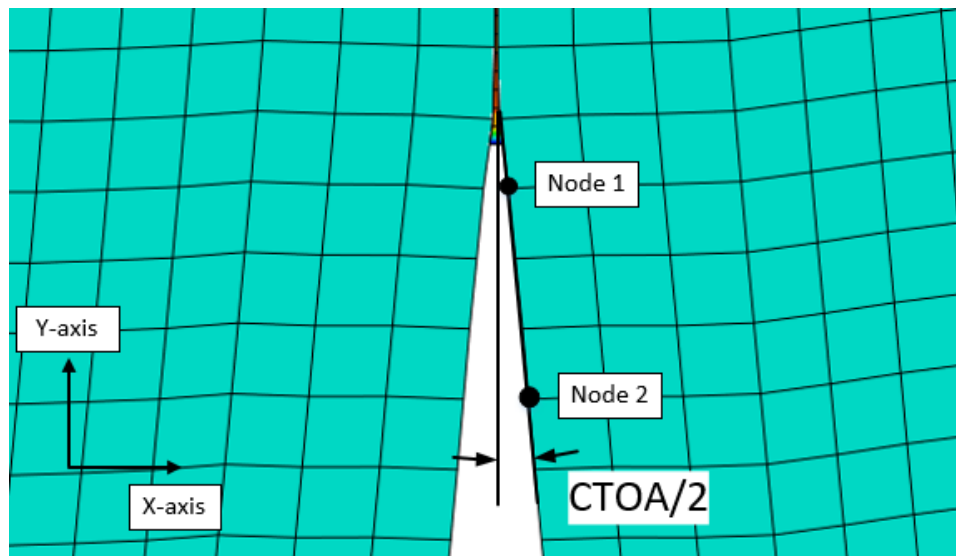


Figure 2.2 - FE CTOA measurement technique.

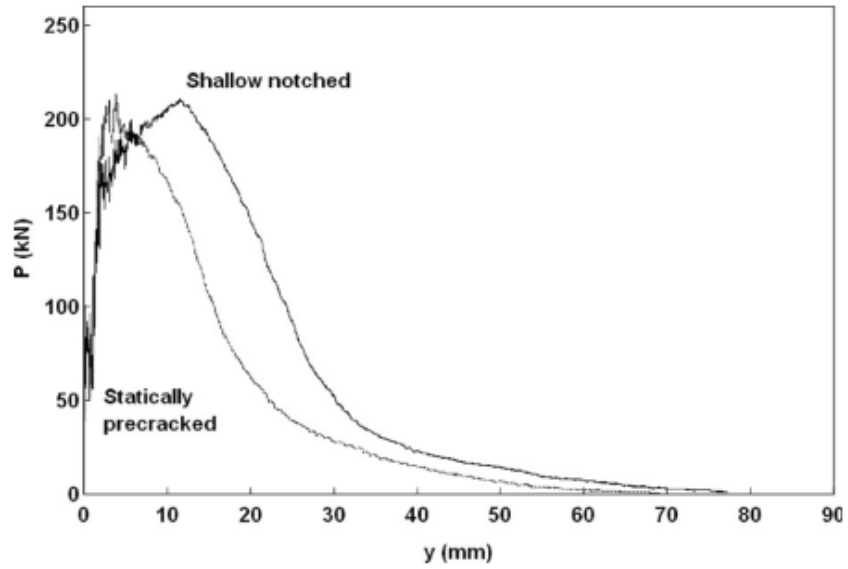


Figure 2.3 - Load vs. load-line displacement plots of shallow-notched DWTT specimens (Xu, Bouchard, & Tyson, 2007)

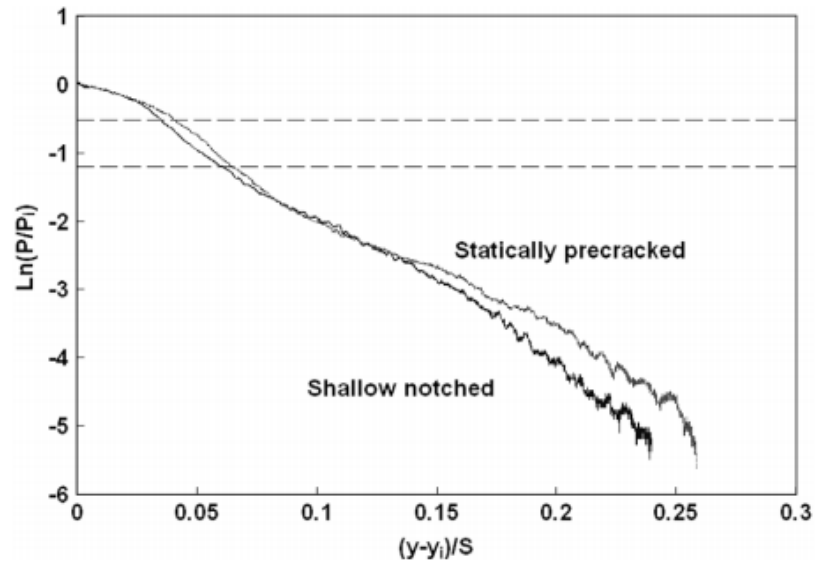


Figure 2.4 - Plots of  $\ln(P/P_i)$  vs.  $(Y-Y_i)/S$  relations and data range for determination of the Slope (Xu, Bouchard, & Tyson, 2007).

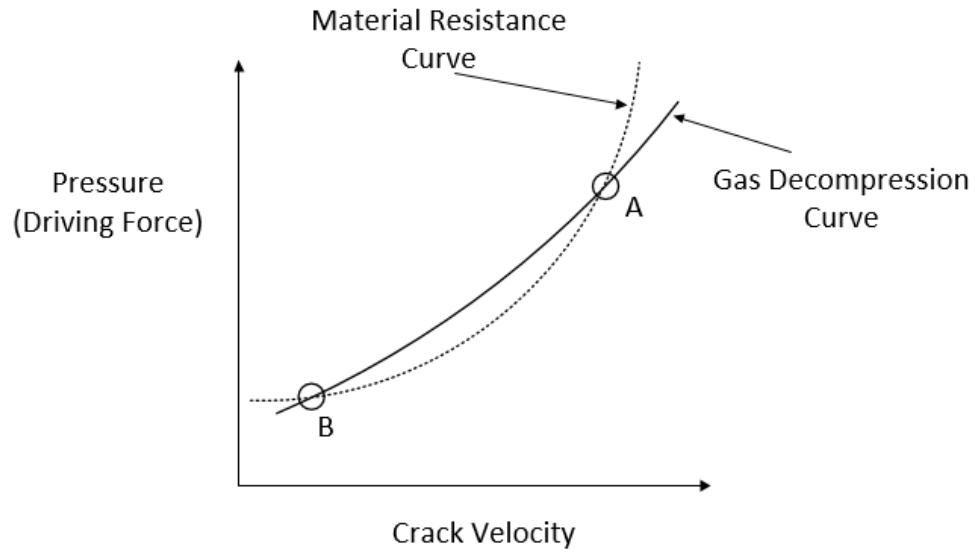


Figure 2.5 - Battelle two curve method.

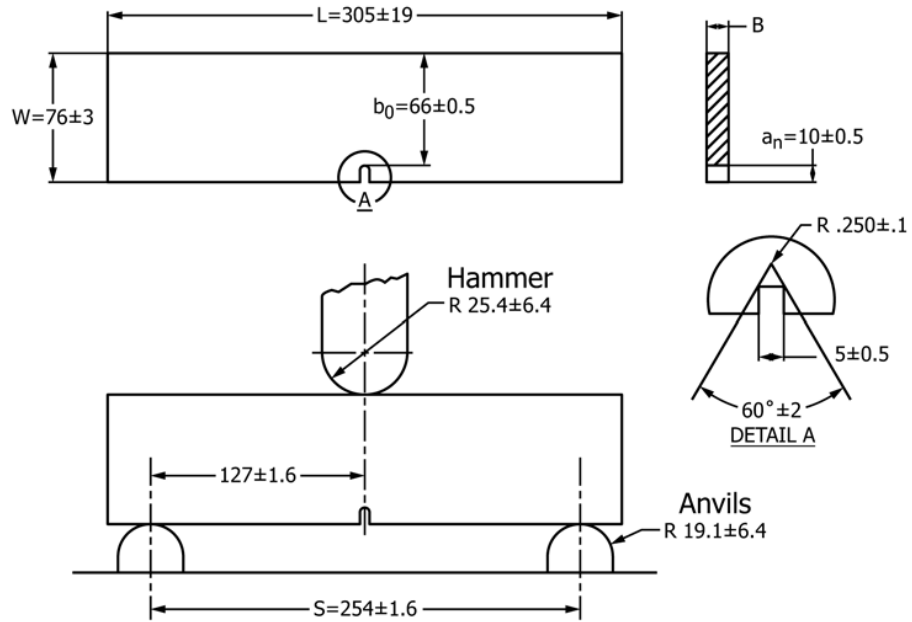


Figure 2.6 - Standard DWTT test specimen dimensions. (ASTM E436-03, 2014)

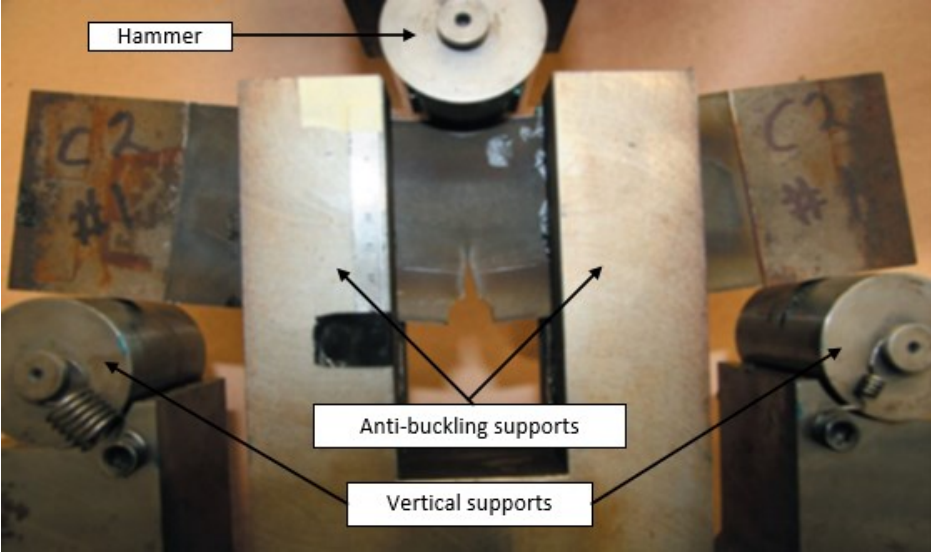


Figure 2.7 - Quasi-static DWTT apparatus at CanmetMATERIALS.

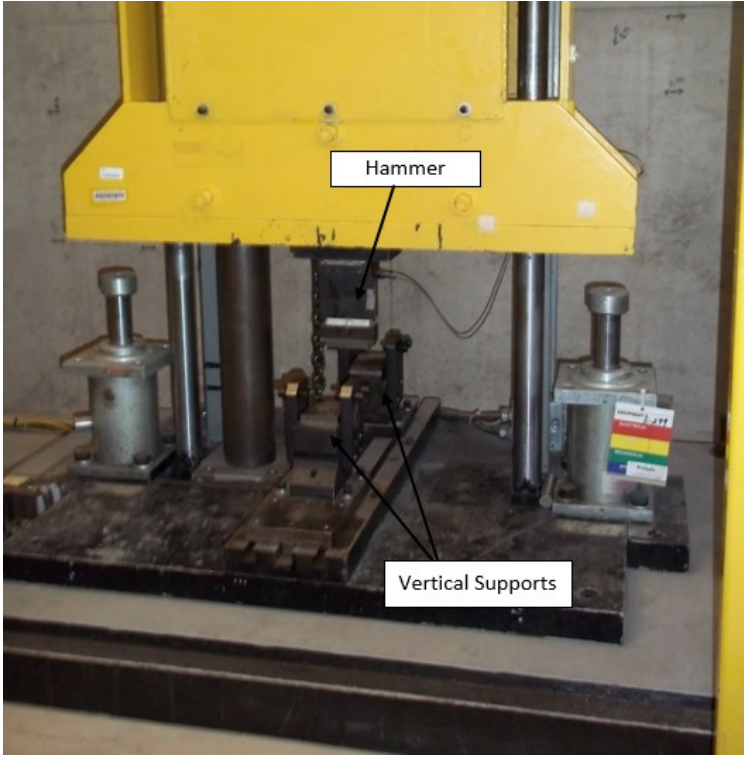


Figure 2.8 – DWTT impact tower at CanmetMATERIALS.

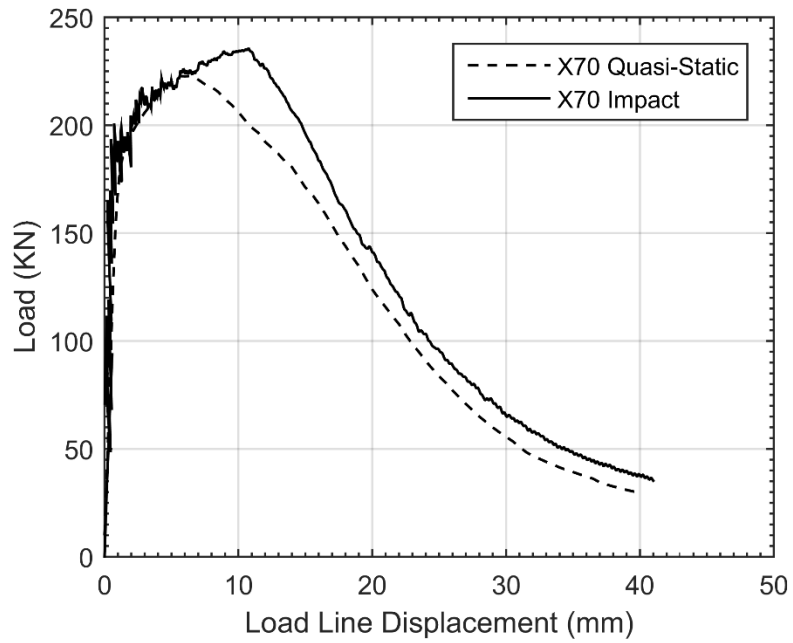


Figure 2.9 – Experimental Load-LLD data of X70 steel at quasi-static and impact loading rates.

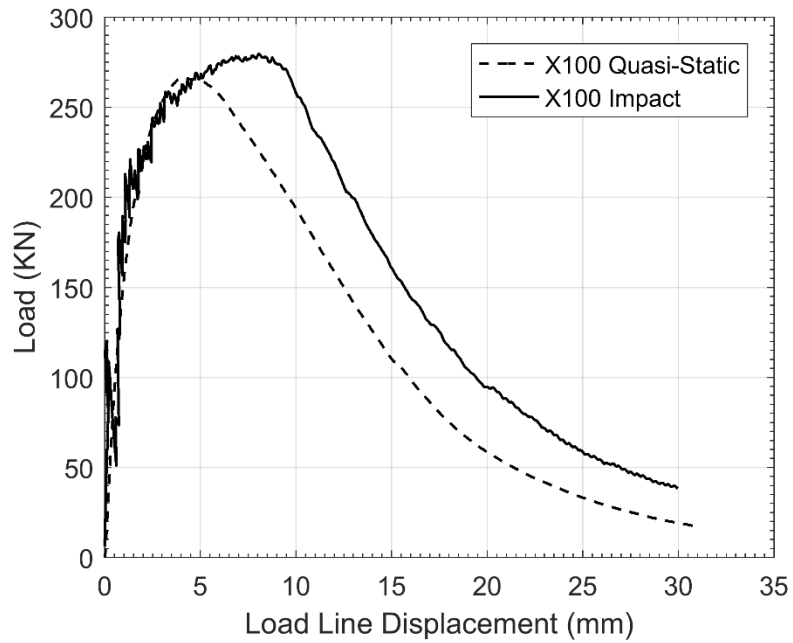


Figure 2.10 - Experimental Load-LLD data of X100 steel at quasi-static and impact loading rates.

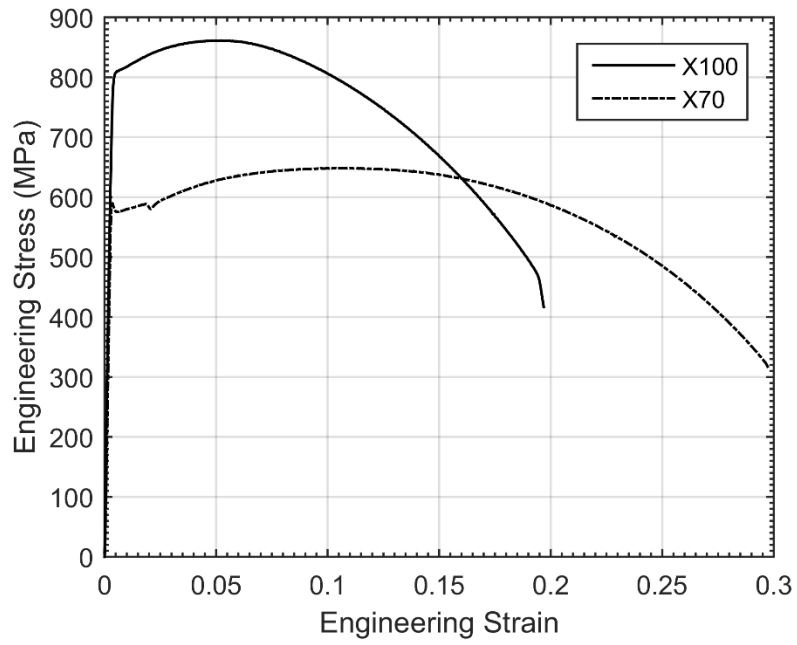


Figure 2.11 - X70 and X100 quasi-static engineering stress-strain curves.

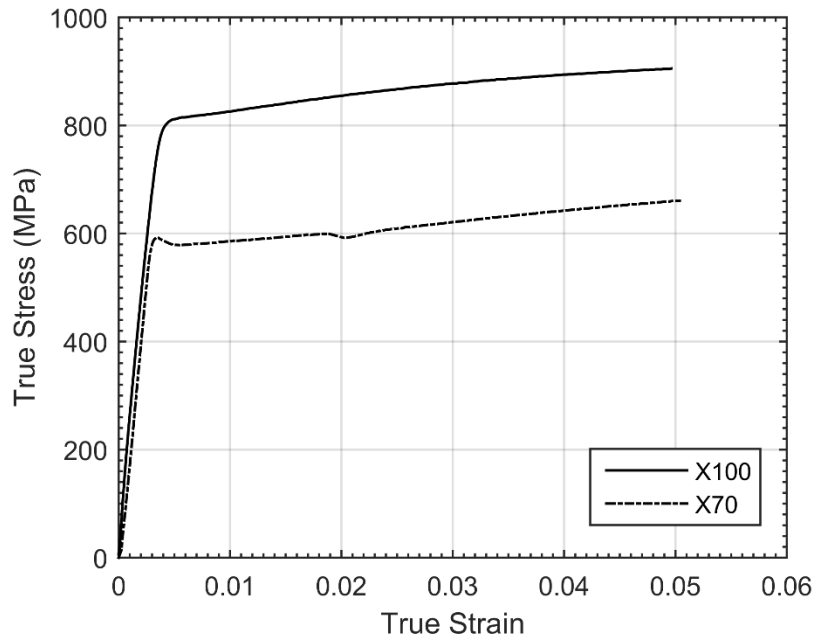
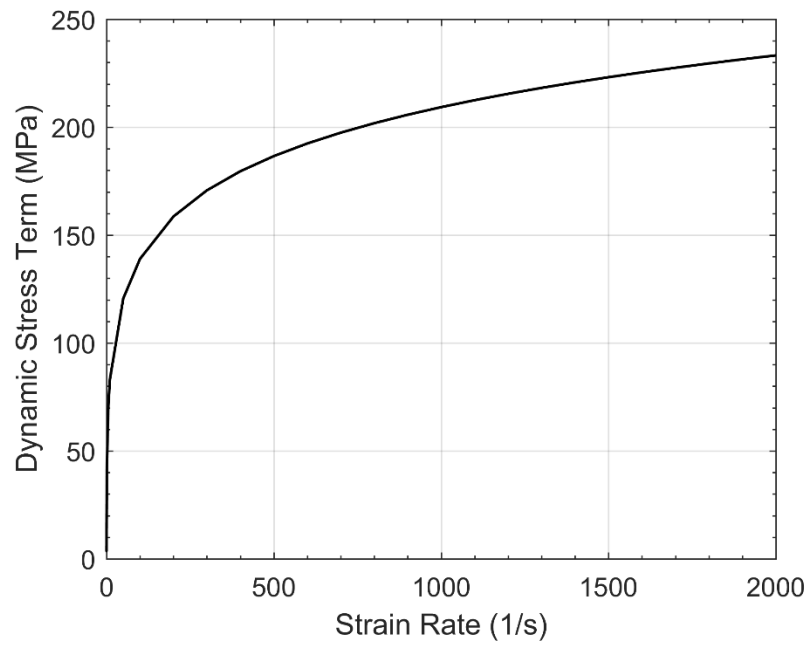
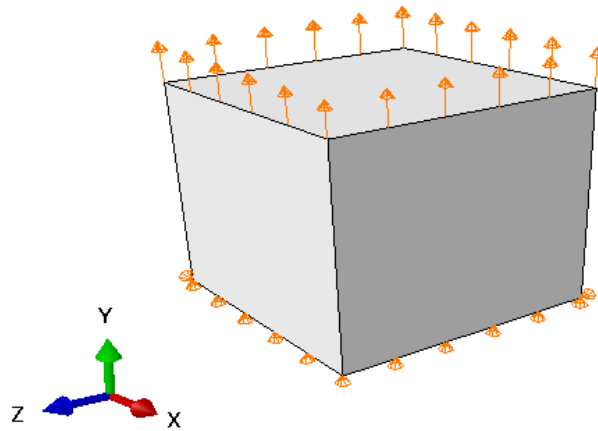


Figure 2.12 - Quasi-static true stress - true strain data. (X70 and X100)



**Figure 2.13 - Dynamic stress term as a function of strain rate from Eq. 2.4.**



**Figure 2.14 - Unit cell model for material verification.**

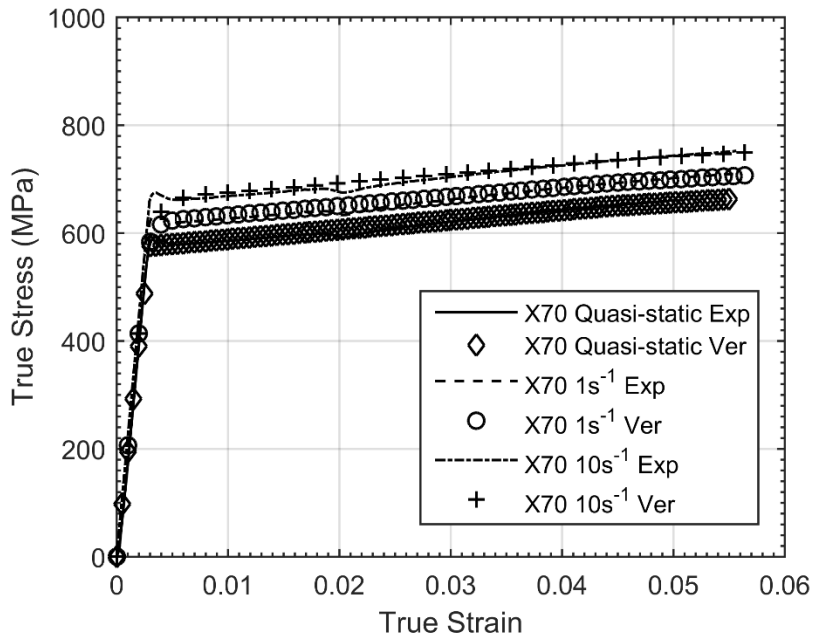


Figure 2.15 - Material rate verification - X70.

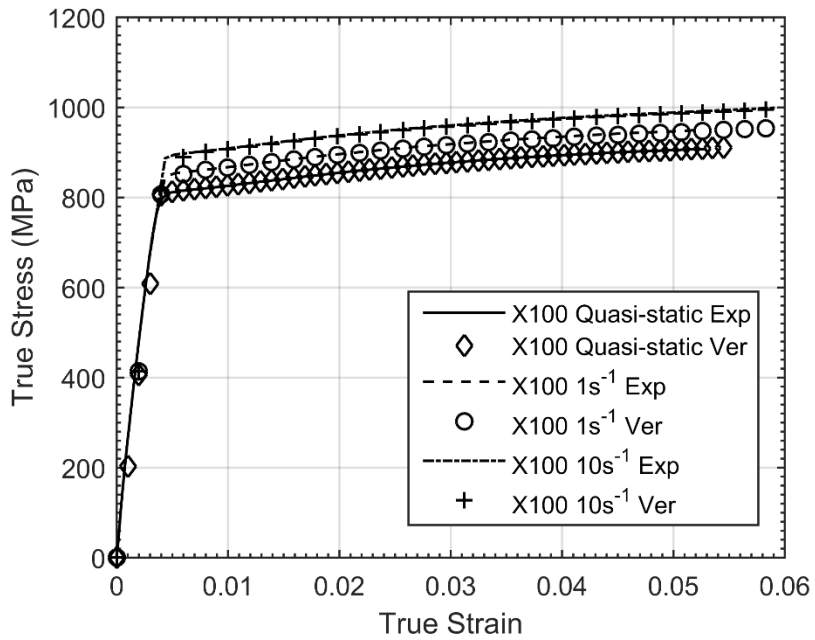


Figure 2.16 - Material rate verification - X100.

### **Chapter 3: The Cohesive Zone Model and Parameter Calibration**

The cohesive zone model (CZM) is a phenomenological model used to simulate crack propagation in mechanical structures. This model has been used extensively in the simulation of ductile fracture in engineering materials as well as in the delamination of adhesively bonded joints.

The cohesive zone model idealizes the fracture process along the crack path by separating the bulk material from the fracture process zone, this concept is illustrated in Figure 3.1. This simplification overcomes the problem of the singularity at the crack tip which arose with the use of classical linear elastic fracture mechanics (LEFM). In LEFM, the stress at a sharp crack tip theoretically approaches infinity, which from a modelling aspect presents a significant challenge. Elastic-plastic fracture mechanics (EPFM) provided a better approximation of the stress state at the crack tip with the inclusion of material non-linearity's due to plasticity. However, neither possess the capability of modelling a moving crack in a structure.

The fracture process zone is modelled by a traction separation law (TSL) and the bulk material is modelled by a tensile true stress-strain curve. This is illustrated in Figure 3.1. The TSL is a relation of the stress to the instantaneous separation of the nodes in the cohesive zone. This chapter introduces the mathematical constitutive behavior behind the cohesive zone model and details the method in which the CZM parameters were calibrated.

### 3.1 Traction-Separation based Modelling in ABAQUS

Damage modelling with the cohesive zone model is a capability programmed into the commercial finite element code ABAQUS. The constitutive behavior of the elements can be defined in a number of ways, for the purposes of this work the traction-separation based method was used. The traction separation behavior operates on three key criteria, namely, the linear elastic stiffness, damage initiation and damage evolution. A generic TSL is shown in Figure 3.2, with all the major parameters identified. The generic TSL will be referenced to illustrate the mathematical concepts presented. The following sections address the mathematical model behind each of the three criteria and the TSL parameters.

#### 3.1.1 Linear Elastic Behavior

The linear elastic behavior of the constitutive model follows Hooke's law for linear elastic materials. The stress in the element is linearly proportional to the extension/ strain through an elasticity matrix. The linear elastic behavior is depicted in the range of  $(0 < \delta < \delta_1)$  in Figure 3.2. This relationship is defined in Eq. 3.1 for a 3 dimensional analysis below (ABAQUS, 2014).

$$T = \begin{Bmatrix} T_n \\ T_s \\ T_t \end{Bmatrix} = \begin{bmatrix} K_{nn} & K_{ns} & K_{nt} \\ K_{ns} & K_{ss} & K_{st} \\ K_{nt} & K_{st} & K_{tt} \end{bmatrix} \begin{Bmatrix} \varepsilon_n \\ \varepsilon_s \\ \varepsilon_t \end{Bmatrix} = K\varepsilon \quad \text{Eq. 3.1}$$

Where  $T$  is the nominal traction vector,  $K$  is the cohesive stiffness matrix, and  $\varepsilon$  is the nominal strain vector. The subscripts  $n$ ,  $s$ , and  $t$  designate the direction of the parameter, indicating normal, shear, and tangential directions, respectively. For a 2 dimensional analysis only the diagonal of the stiffness matrix is required. The nominal strain of the

cohesive element is defined as the current displacement of the nodes relative to the initial thickness, as defined in Eq. 3.2 below.

$$\varepsilon_i = \frac{\delta_i}{g}, i = n, s, t \quad \text{Eq. 3.2}$$

Where  $\varepsilon_i$  is the strain component,  $\delta_i$  is the current displacement component,  $g$  is the initial thickness of the cohesive element. The default value of  $g$  is 1, this value was used for the simulations as it would simplify the strain to be equal to the instantaneous displacement of the cohesive element node. The response of the cohesive element will be that of a linear nature until the damage initiation criterion is satisfied.

### 3.1.2 Damage Initiation

The damage initiation criterion dictates the point when the cohesive element begins to experience non-linear or specially defined separation. This is illustrated as the plateau defined by  $T_i^o$  in Figure 3.2. The maximum nominal stress (MAXS) damage initiation criterion was used in this work. This criterion assumes that damage will begin once the nominal stress in the cohesive element has reached a prescribed value. Mathematically, this concept is applied through the equation below for three dimensions (ABAQUS, 2014).

$$\max \left\{ \frac{\langle T_n \rangle}{T_n^o}, \frac{\langle T_s \rangle}{T_s^o}, \frac{\langle T_t \rangle}{T_t^o} \right\} = 1 \quad \text{Eq. 3.3}$$

Where  $T_i^o$  indicates the maximum traction component in a respective direction,  $T_i$  is the instantaneous cohesive stress, and the Macaulay brackets indicates that the criterion can

only be fulfilled by tensile traction, not a compressive traction. The subscripts  $n$ ,  $s$ , and  $t$  designate the direction of the parameter, indicating normal, shear, and tangential directions, respectively. The variables  $T_i^o$  are user specified parameters, and will be discussed in the latter sections of this chapter.

### 3.1.3 Damage Evolution

Damage evolution is the mathematical response of the model once damage in the element has been initiated, this is typically a load sustaining response or a degradation response. The damage of the element is quantified in a scalar damage variable ( $D$ ) that is used in conjunction with the following equation to define the damage response of the model (ABAQUS, 2014).

$$T = \begin{cases} T_n = \begin{cases} (1 - D)T_n^* \\ T_n^* \end{cases} \\ T_s = (1 - D)T_s^* \\ T_t = (1 - D)T_t^* \end{cases} \quad \text{Eq. 3.4}$$

where  $D$  is the scalar damage variable, and  $T_i^*$  are the computed linear elastic stresses in the cohesive element assuming that there was no damage for the corresponding separation. In this work the bilinear and trapezoidal laws were exclusively used. The damage variable for the bilinear law is defined as a function of displacement in Eq. 3.5 (ABAQUS, 2014).

$$D = \frac{\delta_F(\delta - \delta_1)}{\delta(\delta_F - \delta_1)} \quad \text{Eq. 3.5}$$

where  $\delta$  is the instantaneous nodal displacement,  $\delta_1$  is the displacement at the initiation of damage, and  $\delta_F$  is the displacement at failure. The maximum traction of the trapezoidal

TSL is defined as a function of the nodal displacements by Eq. 3.6, note the displacements ( $\delta_1$ ,  $\delta_2$ , and  $\delta_F$ ) are used with reference to Figure 3.2.

$$T_i(\delta) = T_i^o \begin{cases} \frac{\delta}{\delta_1} & \text{for } \delta < \delta_1 \\ 1 & \text{for } \delta_1 < \delta_2 \\ \left(1 - \frac{\delta - \delta_2}{\delta_F - \delta_2}\right) & \text{for } \delta_2 < \delta_F \end{cases} \quad \text{Eq. 3.6}$$

where  $T_i(\delta)$  the traction vector as a function of the nodal displacement, and  $\delta_2$  is the nodal displacement at the loss of carrying capacity. The scalar damage variable was then calculated in terms of the nodal displacement using Eq. 3.7.

$$D = \begin{cases} 1 - \frac{\delta_1}{\delta} & \text{for } \delta_1 < \delta_2 \\ 1 - \frac{\delta_1}{\delta} \left(1 - \frac{\delta - \delta_2}{\delta_F - \delta_2}\right) & \text{for } \delta_1 < \delta_2 \end{cases} \quad \text{Eq. 3.7}$$

### 3.1.4 Element Based Cohesive Zone Modelling in ABAQUS

The element based approach to cohesive zone modelling was exclusively used for the purposes of this work. ABAQUS 6.14-2 offers a library of cohesive elements, and the element type COH2D4 (4 node, 2-dimensional element) was used (ABAQUS, 2014). The cohesive elements act as an interface between the parts of an analysis along the crack path, as illustrated in Figure 3.3. They are secured to the parts by using a surface-surface tie constraint. This function constrains the nodes of the cohesive elements to the surface of the surrounding structure. The implementation of the cohesive zone model in ABAQUS requires the user definition of several parameters, namely, the cohesive stiffness matrix

and the maximum traction vector. Moreover, the shape of the TSL and the sizing of the cohesive mesh must be assigned as well. The following sections detail the selection and justification of these parameters.

### **3.2 Calibration of the Cohesive Zone Model Parameters**

Calibrating the cohesive zone model is currently one of the most challenging aspects with the implementation of this model. In the work of (Schwalbe, Scheider, & Cornec, 2013) a succinct method was presented in which a Gurson material damage model was used in the simulation of a unit cell to obtain the shape of the TSL and the parameters. This has many advantages including its ability to adapt the shape to certain loading rates and levels of biaxiality as demonstrated in the work of (Anvari, Scheider, & Thaulow, 2006). However, the CZM is a phenomenological method of modelling crack propagation and using a material damage model as a calibration technique has some inherent disadvantages, such as requiring a high level constitutive model to calibrate the CZM.

In this chapter, calibration techniques are assembled and applied to high strength pipeline steels. The decision of the values for the CZM parameters are presented along with the justification based on available literature.

#### **3.2.1 Cohesive Stiffness**

The stiffness of the cohesive zone is the initial slope of the TSL curve, as illustrated in Figure 3.2. The cohesive stiffness was taken to be  $2 \times 10^6$  MPa/mm in the normal direction for all models. This value is approximately an order of magnitude larger than the typical young's modulus of steel. This value was chosen based on the research performed

by (Schwalbe, Scheider, & Cornec, 2013) and (Yuan & Li, 2014) . In the work of (Schwalbe, Scheider, & Cornec, 2013) it is stated that when using a cohesive zone model, the initial stiffness should be a very large value, approaching infinity. The work of (Yuan & Li, 2014) examined the effect of different cohesive stiffness values on the results of a propagation analysis in a compact tension specimen. Specifically, their analysis focused on the effect on the load-displacement data. It is evident by the results that having a stiffness 5-10 times the magnitude of the bulk material elastic modulus is ideal for simulating ductile fracture as it removes the sensitivity of the model response to the initial stiffness. As well, the results for the stiffness 5-10 time the magnitude of the bulk material modulus closely replicates the results of using an infinite stiffness.

In ABAQUS, a 2-dimensional analysis also requires a stiffness in the tangential ( $K_{tt}$ ) and the shear ( $K_{ss}$ ) direction as well, these values were calculated using the equation below.

$$K_{tt} = K_{ss} = \frac{K_{nn}}{2(1 + \nu)} \quad \text{Eq. 3.8}$$

This resulted in a stiffness of  $7.69 \times 10^5$  MPa/mm in the tangential and shear directions. All stiffness values used are summarized in Table 3.3.

### **3.2.2 Shape of the Traction Separation Law**

The shape of the TSL is the graphical representation of the TSL parameters and how they vary with separation. There are many different shapes, such as the bilinear,

trapezoidal, exponential, polynomial and constant. These shapes are illustrated in Figure 3.4.

There have been many works which have investigated the effect of different TSL shapes on the response of a CZM analysis, see (Alfano, 2006), (Volokh, 2004), (Li & Chandra, 2002). In the majority of these efforts comparisons were made between different shapes, such as in the work of (Alfano, 2006), where the bilinear, trapezoidal, and exponential were examined. However, in the aforementioned literature only a linear elastic material was used with no plasticity. In the work of (Scheider & Brocks, 2003), a trapezoidal TSL was compared to an exponential law and a polynomial law. The results demonstrate that the trapezoidal law produces a larger toughness than the other two shapes for the same parameters.

The trapezoidal law was exclusively used for the calibration of the main parameters in this work. The specific shape of the law chosen such that the  $\frac{\delta_2}{\delta_F} = 0.75$  and  $\frac{\delta_1}{\delta_F} = 0.015$  for X70, and  $\frac{\delta_2}{\delta_F} = 0.75$  and  $\frac{\delta_1}{\delta_F} = 0.02$  for X100. The displacement ratios are used with reference to Figure 3.2. This shape was chosen based on the work of (Schwalbe, Scheider, & Cornec, 2013), which recommended the trapezoidal shape for ductile materials. Enforcing the shape of the TSL then forces a relationship between the maximum traction and the cohesive energy. This was done to simplify the calibration of the model. The choice to enforce the shape of the model will be explained in the following sections.

In Chapter 4 of this work, the bilinear TSL and variations on the trapezoidal laws are examined and compared to determine the effect of the shape on the crack growth resistance and the CTOA. In Chapters 5, 6, 7, and 8 of this work the trapezoidal laws ( $\frac{\delta_2}{\delta_F} =$

0.75 and  $\frac{\delta_1}{\delta_F} = 0.015$  for X70 and and  $\frac{\delta_2}{\delta_F} = 0.75$  and  $\frac{\delta_1}{\delta_F} = 0.02$  for X100) were exclusively used to model ductile fracture of the pipeline steels.

### 3.2.3 Cohesive Energy

The area under the TSL curve represents the cohesive energy as shown in Figure 3.2. The most commonly used method, when a material damage model is not available, to determine the cohesive energy was proposed in (Schwalbe, Scheider, & Cornec, 2013). In (Schwalbe, Scheider, & Cornec, 2013), the authors suggest that the cohesive energy is equal to the value of the  $J$ -resistance curve of the material when the crack has propagated the length of the stretch zone width (SZW). The stretch zone width zone is a transition region between the fatigue pre-crack and the onset of stable crack growth. As the SZW is a value which can be determined experimentally, this method is very attractive with regular access to the material testing data. The  $J$ -resistance data of the material used in this work can be found in the work of (Xu & Tyson, 2015). However, since the SZW was not examined during the experiments, the initiation energy was taken as an upper limit of the cohesive energy. The initiation fracture toughness ( $J$  value at 0.2 mm of crack growth) of X70 and X100 were 345 kJ/m<sup>2</sup> and 209 kJ/m<sup>2</sup>, respectively (Xu & Tyson, 2015). The examination of the fracture toughness of these materials at the SZW is a possibility for future research.

In the work of (Yuan & Li, 2014), the effect of the maximum traction on the relationship between the  $J$ -integral initiation energy and the cohesive energy was examined. Their major finding was that when the maximum traction is greater than three times the yield stress of the material, the cohesive energy is significantly less than the

initiation energy of the  $J$ -integral. This presents a significant complication as it is commonly known for the modelling of pipeline steels that a maximum traction greater than three times the yield stress of the material is preferred. For this reason, the initiation energy of the  $J$ -integral was taken as the upper limit for the cohesive energy. A relation between the cohesive energy, and maximum traction was enforced through the shape of the TSL, as mentioned in the previous section.

#### **3.2.4 Maximum Traction**

The maximum traction is the largest stress which the cohesive element can sustain prior to a loss of carrying capacity; it is the maximum stress value as shown in Figure 3.2. When the CZM is used to model high strength and high toughness steels such as X70 and X100, the maximum traction should be taken as a multiple of the material yield stress in the range of 2.5-3.5 times the yield stress (Shim, Wilkowski, Rudland, Rothwell, & Merritt, 2008). Typically this is where a large amount of iteration is required; however, in this work a relation was used in order to explicitly derive the maximum traction based on specifying the exact shape of the TSL. This algorithm was written into a program where the shape would define the law, and a cohesive energy would yield a corresponding maximum traction and vice versa. Future work on the calibration of the maximum traction and cohesive energy for pipeline steels will need to be completed; however, for the purposes of this work the enforcement of the shape will suffice.

### 3.2.5 Effect of Separation Rate on the TSL

The effect of separation rate of the cohesive element on the TSL is briefly discussed in the work of (Schwalbe, Scheider, & Cornec, 2013). It is recommended to assess the effect of separation rate based on a relation between the separation rate and the maximum traction or the cohesive energy. For this work, the update to the TSL was assessed based on the steady-state crack velocity. The update to the TSL was made on a trial and error basis with different maximum tractions and cohesive energy, thus the determination of the function  $f$  will be presented in the later chapters.

$$\Gamma_{Dynamic} = f(CV) \quad \text{Eq. 3.9}$$

where  $\Gamma_{Dynamic}$  is the rate updated cohesive energy and  $f(CV)$  is a function of crack velocity. A more useful form of the function,  $f$  would be to define it in terms of separation rate of the cohesive element; however, as the separation rate of the cohesive element changes throughout crack propagation, a relation would be difficult to achieve and highly inaccurate. The choice to define the function in terms of crack velocity was to allow for a clearly defined independent variable. Thus the manner in which the relation is presented is only useful for examining the trend. As a result of the explicit relationship between the maximum traction and the cohesive energy, the maximum traction is adjusted in the same manner as the cohesive energy.

In this work, the effect of separation rate was assessed on a trial and error basis, higher loading rates were adjusted to match the CTOA of the material. The TSL of both materials were updated in the same manner. The function  $f(CV)$  will be developed in Chapter 7 for both materials to update the CZM for a constant CTOA.

A generic example of the TSL updated for crack velocity (rate) is illustrated in Figure 3.5. As can be seen, the shape of the TSL was kept constant and the maximum traction/cohesive energy were increased. The intention behind keeping the same shape of the TSL was based on the results of Chapter 4, which demonstrate that changing the shape of the TSL also has an effect on the CTOA for the same parameters.

### **3.2.6 Cohesive Zone Mesh Sizing**

In the work of the authors predecessors (Dunbar, 2011) and (Parmar, 2014), the sizing of the mesh used in the cohesive zone was assigned based on the work of (Diehl, 2008), which stated that at least three cohesive elements were required per adjacent bulk element. This lead to very fine meshes. As the intention of this work is to prelude a model of a long running crack in a pipeline, the mesh should be kept as large as possible while maintaining an adequate resolution of the fracture process zone.

There are two main parameters which must be considered when sizing the mesh of a CZM analysis; these are the aspect ratio of the cohesive mesh and the number of elements in the cohesive length.

The aspect ratio of the cohesive element is an important parameter in a CZ analysis. It has the potential to be a source of numerical instability if the deformation gradient becomes too large across an element. A typical cohesive element is illustrated in Figure 3.6. The aspect ratio of the element is defined as the ratio of the length ( $h$ ) to the thickness ( $g$ ). In the work of (Schwalbe, Scheider, & Cornec, 2013), it is recommended to use cohesive elements with a length ( $h$ ) on the order of 0.05mm-0.25mm, based on the overall size of the model. Furthermore, it is also recommended to have a high aspect ratio such

that  $h \gg g$ ; however, there were no specific guidelines assigned. For the purposes of this work, the length of cohesive element was assigned a minimum value based on the maximum separation of the TSL ( $\delta_F$ ). Through trial and error, it was found that having a value of ( $h$ ) that was less than the maximum separation of the TSL would increase the likelihood of numerical convergence issues due to large deformations. It was found that X100 was more sensitive to this than X70.

The other concern surrounding the mesh of the CZ analysis was the cohesive length. The cohesive length is the length ahead of the crack tip to the point where the maximum traction is first attained. The concept of a cohesive length was proposed by (Hillerborg, Modeer, & Peterson, 1976), during the study of crack propagation in concrete. Hillerborg proposed that the length of the cohesive zone was proportional to the material bulk modulus, cohesive energy, and the maximum traction. This length was characterized using the following equation (Hillerborg, Modeer, & Peterson, 1976).

$$L_{cz} = M \frac{E\Gamma_o}{(T_n^o)^2} \quad \text{Eq. 3.10}$$

where  $L_{cz}$  is the cohesive length,  $E$  is the bulk material elasticity modulus,  $\Gamma_o$  is the cohesive energy,  $T_n^o$  is the maximum traction in the normal direction, and  $M$  is an adjustment parameter. In the original paper, the author stated its validity for plane stress and as an approximation for plane strain. Since the original work, many other researchers have adopted this equation and altered it based on their individual models by adjusting the ‘ $M$ ’ parameter in Eq. 3.10. For this work, the value of  $M$  was assumed to be equal to 1.0. This is based on the fact that the ‘ $M$ ’ parameter is a plane stress adjustment parameter, and

all simulations in this work assume plane strain. As this equation describes the length of the zone in which cohesive damage is occurring, the main use of it is to assess the number of cohesive elements to be placed in the zone. This however, is still a largely unknown aspect of the CZM when used for modelling of ductile fracture propagation. When the CZM is used for the modelling of delamination, it is recommended in the work of (Moes & Belytschko, 2002), to have a minimum of 10 elements in the cohesive length. Other work, including that of (Falk, Needleman, & Rice, 2001), it is stated that as little as 2-5 elements were used in the cohesive length of their analysis.

In this work, a minimum of 10 cohesive elements were assigned to the cohesive length of the material. With regards to the sizing of the bulk material elements adjacent to the cohesive zone, there were a minimum of three cohesive elements per bulk material element. This was chosen based on the work of (Diehl, 2008). Thus the size of the cohesive elements dictated the size of the adjacent bulk material elements. The maximum allowable sizing of the meshes used in this work are summarized in Table 3.1, the specific sizes used for each model will be presented in their respective chapters. The values given in Table 3.1 are maximums based on the analysis and literature presented in this section. The structure of the cohesive mesh for all analyses in this work were single layered, structured, four node quadrilateral elements. This illustrated in Figure 3.6.

### **3.2.7 TSL Calibration with the DWTT Model**

The CZM parameters were calibrated as much as possible from experimental material testing and literature. However, the unknown nature of the cohesive energy and maximum traction for pipeline steels posed a significant challenge. In an effort to

overcome said challenge, a relationship between the maximum traction and the cohesive energy was forced by the shape of the TSL. To calibrate the final parameters of the CZM, the quasi-static DWTT model, presented in Chapter 6, was used for the final adjustments. The final adjustments were based on matching the CTOA of the model to the experimental CTOA of the material.

The maximum traction began as three times the yield stress, and was iterated until the CTOA data matched that of the experimental value for the DWTT specimen under quasi-static loading conditions. The major TSL parameters and the corresponding SS-CTOA are listed in Table 3.2. It was found that a maximum traction of approximately 3.2 times the yield stress produced a CTOA with good agreement to the experimental value for both materials. The specification for the DWTT model will be presented in Chapter 6. The final CZM parameters used are listed in Table 3.3

### **3.3 Verification of the Cohesive Zone Model**

To verify the implementation of the cohesive zone model in ABAQUS, a unit cell analysis of a single cohesive element was performed. A 2-dimensional square model of a cohesive element was analyzed under an axial load. The dimensions of the model were 1mmx1mm. The model is illustrated in Figure 3.7. The boundary conditions involved a vertical constraint along the bottom edge and a horizontal constraint on the bottom left node to prevent linear or rotational motion along the bottom edge. A displacement was assigned to the top surface that was ramped from 0 to a prescribed value past the maximum separation of the TSL. The model with the boundary conditions can be seen in Figure 3.7.

The normal stress in the element and the displacement of the top surface nodes were extracted, correlated and compared to the prescribed TSL. As seen in Figure 3.8 and Figure 3.9, both TSL's were successfully implemented into ABAQUS with the element response matching the prescribed TSL.

**Table 3.1 - CZM mesh parameters for SSY, SENT, DWTT and Plate models.**

Material	Cohesive length ( $L_{cz}$ ) (mm)	Maximum cohesive mesh length ( $h$ ) (mm)	Maximum bulk mesh size (mm)
X70	5.58	0.558	1.67
X100	4.38	0.438	1.31

**Table 3.2 - TSL calibration trials with quasi-static DWTT model.**

Material	Normal Maximum Traction (MPa)	Cohesive Energy (MPa-mm)	Average SS-CTOA (Degrees)
X70	1750	88.6	7.6
	1850	98.8	12.2
	1950	110.0	16.3
X100	2415	126.1	5.2
	2515	136.8	10.1
	2615	147.9	14.3

**Table 3.3 - Quasi-static CZM parameters for SSY, SENT, DWTT and Plate model's.**

Material	Cohesive Stiffness (MPa/mm)			Maximum Traction (MPa)			Cohesive Energy (MPa-mm)
	$K_{nn}$	$K_{ss}$	$K_{tt}$	$T_n^o$	$T_s^o$	$T_t^o$	$\Gamma_o$
X70	$2 \times 10^6$	$7.69 \times 10^5$	$7.69 \times 10^5$	1850	1387.5	1387.5	98
X100	$2 \times 10^6$	$7.69 \times 10^5$	$7.69 \times 10^5$	2515	1886.3	1886.3	136.8

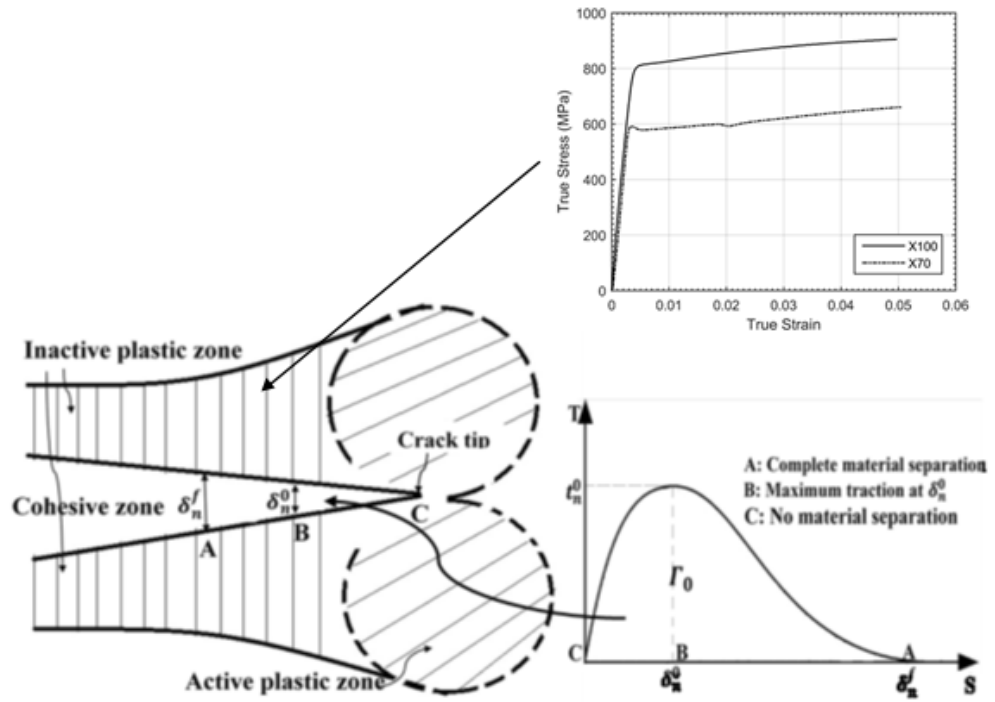
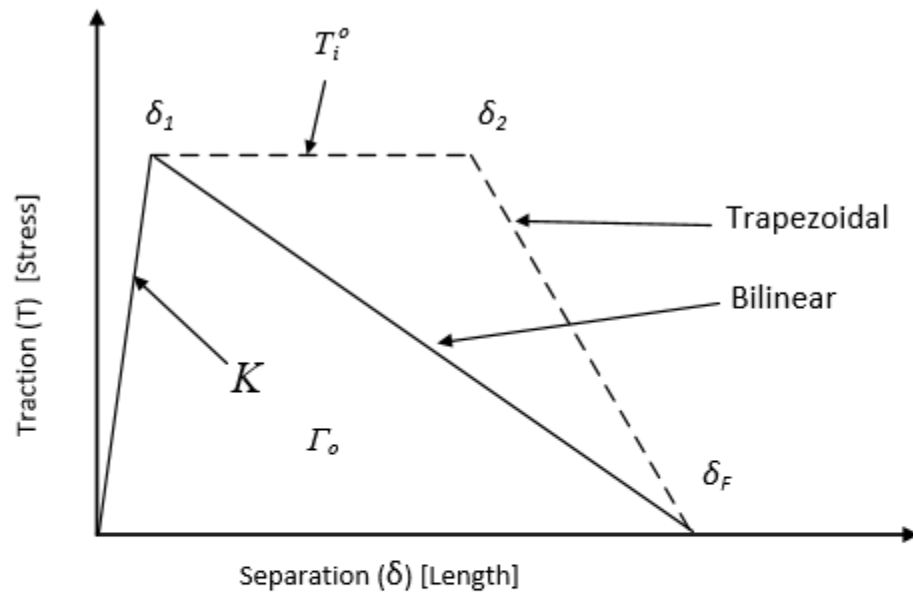


Figure 3.1 - Concept of the cohesive zone model (Li & Chandra, 2002)(modified).



- $T_i^o$ - Maximum traction.
- $\Gamma_o$ - Cohesive energy. (area under the TSL curve)
- $K$ - Initial stiffness of cohesive element. (initial slope of TSL curve)
- $\delta_1$ - Displacement at initiation of damage.
- $\delta_2$ - Displacement at initiation of degradation.
- $\delta_F$ - Displacement at failure of element.

Figure 3.2 - Generic traction separation law.

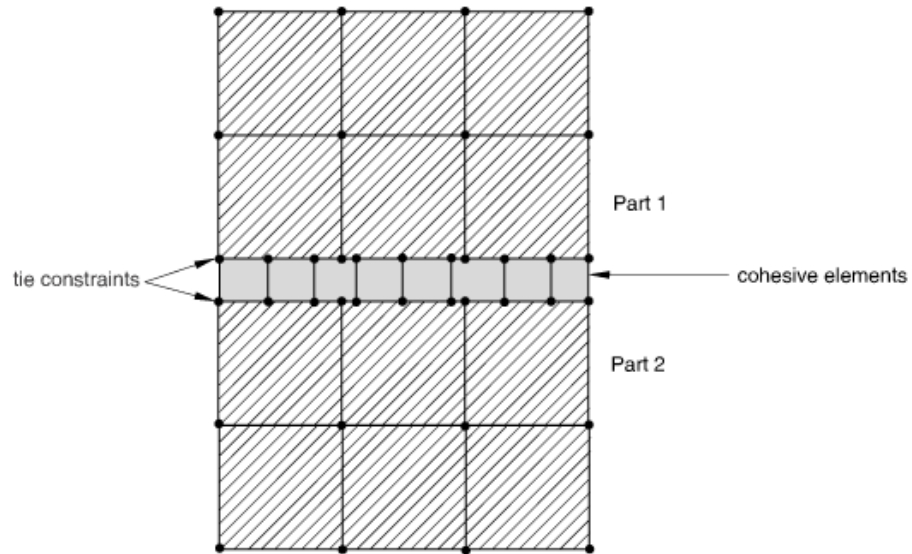


Figure 3.3 - Implementation of cohesive elements in ABAQUS (ABAQUS, 2014).

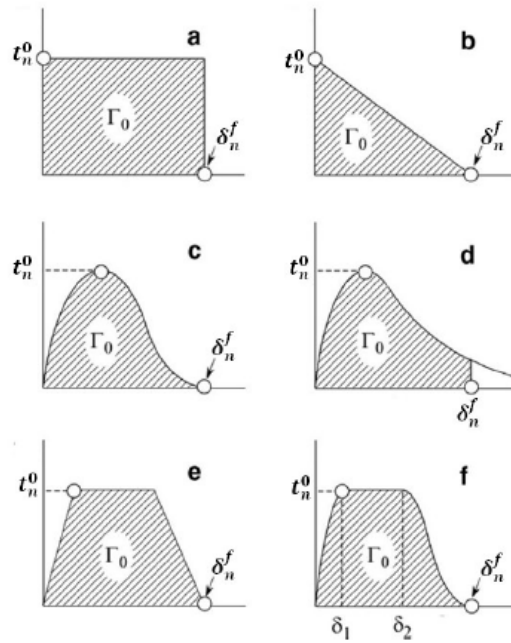


Figure 3.4 - Various TSL shapes: (a) Constant (Dugdale, 1960), (b) Bilinear (Barenblatt, 1962), (c) Polynomial (Needleman, 1987), (d) Exponential, (e) Trapezoidal (Tvergaard & Hutchinson, 1992), (f) Smooth trapezoidal (Schwalbe, Scheider, & Cornec, 2013).

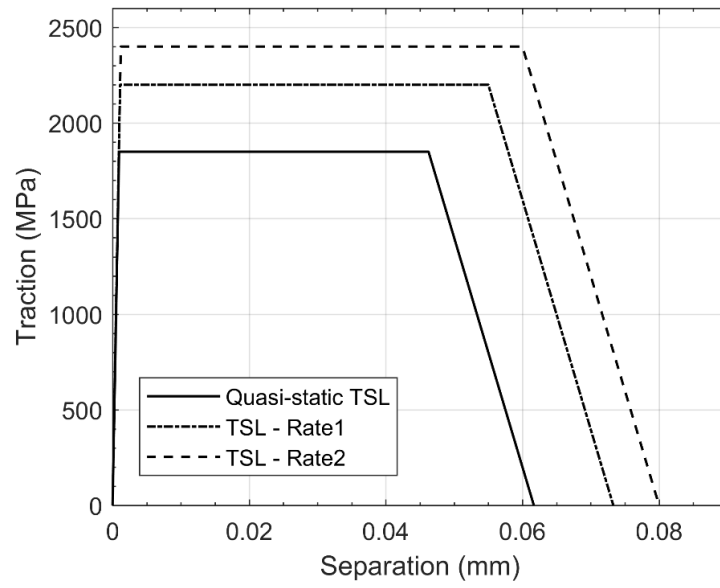


Figure 3.5 - TSL rate dependence (Rate2 > Rate1 > Quasi-static).

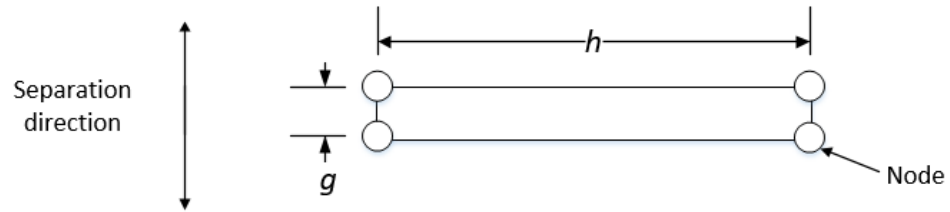
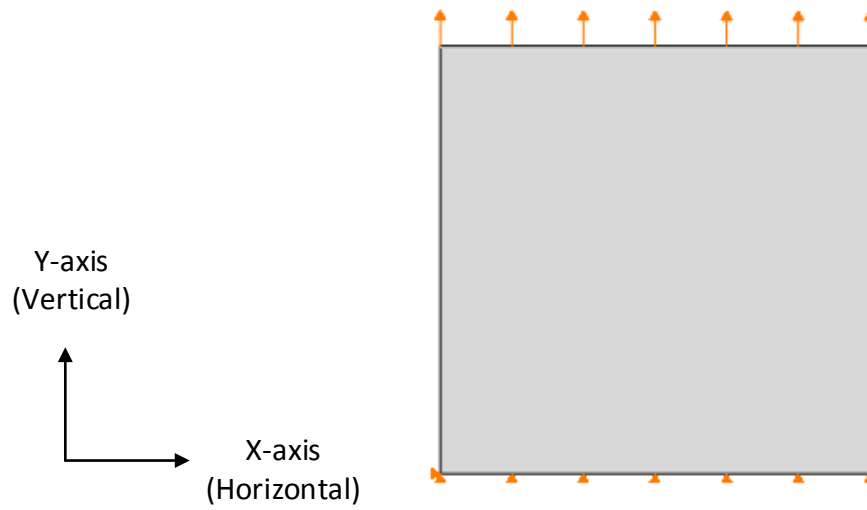
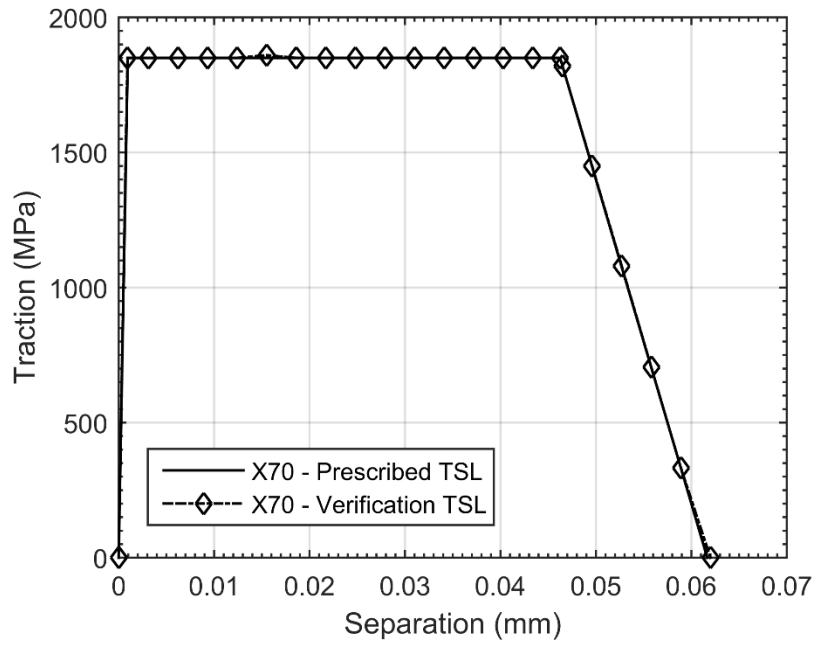


Figure 3.6 - Cohesive element.



**Figure 3.7 - Unit cell loading conditions.**



**Figure 3.8 - X70 TSL verification.**

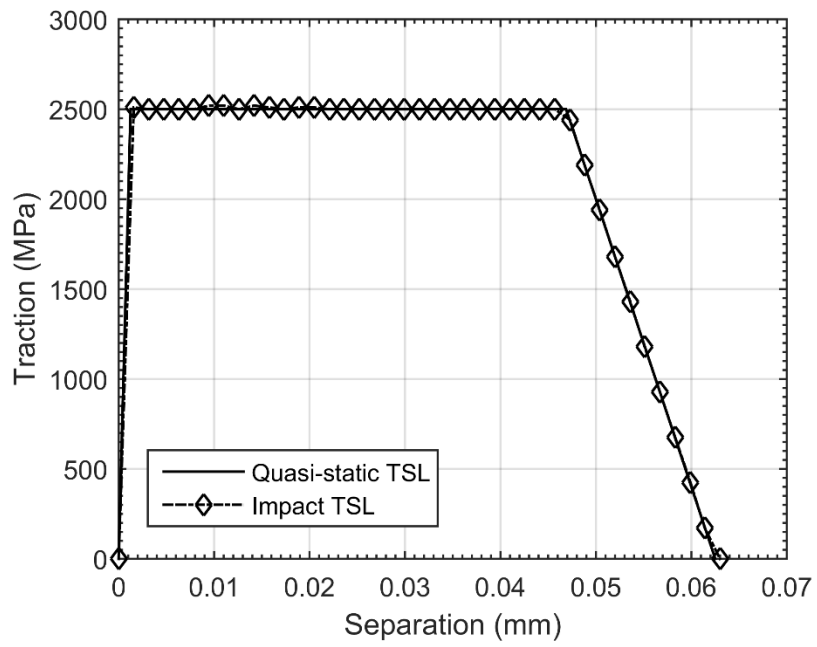


**Figure 3.9 – X100 TSL verification.**

## **Chapter 4: FE Simulation of Ductile Fracture Using a Small Scale yielding Model under Quasi-Static Loading Conditions**

This chapter presents a study conducted on a small scale yielding (SSY) model. In this work, the SSY model was utilized to examine the effect of the shape of the TSL on the results of a crack propagation analysis. As discussed in Section 3.2, there have been many works examining the effect of the TSL shape on the response of a crack propagation model. In this chapter, a specific focus will be placed on examining and comparing the bilinear shape and variations of the trapezoidal law. The specific shapes are outlined in Section 4.1. The effect of the TSL shape will be assessed using the crack growth resistance data and the measured CTOA.

### **4.1 Small Scale Yielding (SSY) Model**

A two dimensional plane strain SSY model was generated and analyzed using the commercial finite element code ABAQUS 6.14-2 (Dassault Systemes, 2014). This section presents the computational model including the geometry, loading conditions, material properties, cohesive properties and mesh design.

#### **4.1.1 Geometry and Computational Procedures**

The small scale yielding model is a theoretical model used to simulate the propagation of an initial edge pre-crack in an infinite plate. The SSY model used in this study was the same as the one utilized in (Tvergaard & Hutchinson, 1992), more specifically it approximates the infinite plate by a circular plate with a sharp notch

extending horizontally from the circles center to the outer edge. The general shape of the model is illustrated in Figure 4.1.

Two different sized SSY models were used in this work. The first was used for the verification of the model through comparison with the work of (Tvergaard & Hutchinson, 1992). This model was assigned a radius ( $r$ ) of 200 mm and an initial crack length ( $a_0$ ) of 200 mm. This was done to match the size of the model used in the original work. The second SSY model, used to analyze the X70 material, was assigned a radius ( $r$ ) of 1000 mm and an initial crack length ( $a_0$ ) of 1000 mm. This larger model was chosen to allow for a longer ligament for the crack to propagate. This larger model allowed for 40mm of propagation. The largest plastic zone simulated was 6.73 mm, which is less than 1% of the model radius at initiation. Moreover, the large model will ensure the conditions of small scale yielding are met and kept throughout propagation, namely, that the plastic zone size remains less than 5% of the radius of the model. This condition was assessed in all models to verify the SSY conditions were held.

The cohesive elements were inserted along the crack path between the two semicircles. This is illustrated in Figure 4.1. The cohesive layer was constrained to the two flanks using a surface-to-surface tie constraint. This constrained the nodes of the cohesive layer to the surface of the flank.

#### **4.1.2 Loading Conditions**

The stress intensity at the crack tip was induced through a displacement field applied at the outer edges of the model. The loading conditions are illustrated in Figure 4.2. The displacement field is applied to the outer edge of the model by specifying nodal

displacements. The specific nodal displacements were calculated using the equations presented below (Williams, 1957).

$$U_x = \frac{K_r}{2G} \sqrt{\frac{r}{2\pi}} \cos\left(\frac{\theta}{2}\right) \left[ (3 - 4\nu) - 1 + 2\sin^2\left(\frac{\theta}{2}\right) \right] \quad \text{Eq. 4.1}$$

$$U_y = \frac{K_r}{2G} \sqrt{\frac{r}{2\pi}} \sin\left(\frac{\theta}{2}\right) \left[ (3 - 4\nu) + 1 - 2\cos^2\left(\frac{\theta}{2}\right) \right] \quad \text{Eq. 4.2}$$

Where  $U_x$  is the nodal displacement in the X-axis,  $U_y$  is the nodal displacement in the Y-axis,  $K_r$  is the maximum far-field stress intensity factor,  $G$  is the material shear modulus,  $r$  is the radius of the circular model,  $\nu$  is the material Poisson's ratio, and  $\theta$  is the angle between the horizontal axis (counterclockwise) and the node of interest. The angle  $\theta$  is defined graphically in Figure 4.1.

The displacements calculated from Eq. 4.1 and Eq. 4.2 were applied to specified nodes on the outer edge of the model. The nodes were set to be  $5^\circ$  apart from one another. This was chosen based on the work of (Dunbar, 2011) and (Parmar, 2014) who utilized the same model as the one presented. The displacement was ramped from 0 to the prescribed nodal displacement over the course of the analysis. It was found that an average loading rate of 1mm/s was sufficient for the quasi-static analysis. The maximum magnitude of the applied stress field was iterated until the crack propagated through the intended propagation region (40 mm). It was found, through trial and error, that a  $K_r$  value of  $50000 \text{ MPa}\sqrt{\text{mm}}$ , approximately  $(11 K_o)$ , was sufficient to propagate the crack the desired distance in all models. All simulations with the SSY model were under quasi-static loading conditions.

### **4.1.3 Material Properties**

Two materials were analyzed in this chapter. The first was a typical high strength steel, which will be referred to as TH steel for the remainder of this work. This material was introduced in the work of (Tvergaard & Hutchinson, 1992). The material properties of TH steel are those typical of a high strength steel, specifically the modulus of elasticity, yield strength and poisson's ratio are 200 GPa, 600 MPa, and 0.3 respectively. The true stress-plastic strain data was acquired from the work of (Dunbar, 2011), the data is tabulated in Table 4.1 and can be seen plotted in Figure 4.3. The TH material was implemented in the model in the same manner as the X70 material, which was discussed in Section 2.3. This material was only used for the verification of the numerical model by comparison with FE data generated in (Tvergaard & Hutchinson, 1992).

The other material used in this chapter was the X70 steel presented in Section 2.3. It is important to note all simulations in this chapter are under quasi-static loading conditions. The material elasticity properties are listed in Table 2.3 and the true stress-plastic strain properties are listed in Table 2.5.

### **4.1.4 Cohesive Zone Properties**

Four traction separation laws were used in the original work of (Tvergaard & Hutchinson, 1992), which will be referred to as TH-1, TH-2, TH-3, and TH-4. The cohesive properties for the TH steel used in (Tvergaard & Hutchinson, 1992) were extracted from the work and implemented in ABAQUS. The TH materials TSL's are illustrated in Figure 4.4 and the cohesive parameters are listed in Table 4.2.

The cohesive zone model properties for the X70 material were presented and discussed in Section 3.2. The calibration of the cohesive parameters was for a TSL of a trapezoidal shape with the loss of carrying capacity occurring at three quarters of the final displacement ( $\frac{\delta_2}{\delta_F} = 0.75$ ). The naming convention for the four laws examined is based on the displacement at the loss of carrying capacity relative to the final displacement ( $\frac{\delta_2}{\delta_F}$ ). The variables defined in this ratio are illustrated in Figure 3.2. The naming convention for the TSL shapes is presented in Table 4.3. The cohesive properties used in the analysis are listed in Table 4.4 and illustrated in Figure 4.5.

#### **4.1.5 FE Mesh Design**

The two SSY models were meshed in the same manner; however, the element sizing was varied. The SSY model was partitioned into three separate regions; the ligament region, the transition region and the bulk region. These regions are illustrated in Figure 4.6. The mesh of half of the model can be seen in Figure 4.7; only half of the model was shown as the other half is the mirror image through the horizontal plane. The bulk zone was assigned four node plane strain quadrilateral elements using a sweeping technique. The sweeping path was assigned around the circumference of the model. The structure of the bulk elements can be seen in Figure 4.7. The mesh transition zone was assigned a combination of four node plane strain quadrilateral elements and three node plane strain triangular elements. This zone was integrated to facilitate a rapid transition in mesh sizing between the bulk zone and the ligament zone. The transition zone mesh can be seen in Figure 4.8. The ligament region was assigned structured four node plane strain quadrilateral elements. These elements were constructed for an aspect ratio of 1 to prevent

uneven deformation. The ligament mesh is illustrated in Figure 4.9. The specific details of the FE mesh are shown in Table 4.5.

## 4.2 Analysis Methodology

The TH material and respective TSL's were only used for the verification of the model through a comparison of the crack growth resistance data generated in this work to that of the original work (Tvergaard & Hutchinson, 1992). This comparison is made in Section 4.3.

The remainder of the chapter is focused on the analysis of the shape off the TSL. The methodology for the analysis of the SSY model, with the X70 material, was to use the parameters from the calibrated TSL and change the shape of the TSL. The parameters were originally calibrated with a shape of  $\frac{\delta_2}{\delta_F} = 0.75$ . Thus, to examine the effect of the shape of the TSL, the ratio of  $\frac{\delta_2}{\delta_F}$  was reduced to 0.5 and 0.25, as well as a bilinear law was used. The shapes are illustrated in Figure 4.5. The main points to examine the comparison were by that of the crack growth resistance data and the measured CTOA.

The crack growth resistance data was examined in a non-dimensional format using the stress intensity at initiation and the radius of the plastic zone. The critical stress intensity is related to the cohesive energy through the following equation (Tvergaard & Hutchinson, 1992).

$$K_o = \sqrt{\frac{E\Gamma_o}{1 - \nu^2}} \quad \text{Eq. 4.3}$$

Where  $K_o$  is the critical stress intensity value,  $E$  is the bulk material modulus of elasticity,  $\Gamma_o$  is the cohesive energy, and  $\nu$  is the bulk material poisson's ratio. When the conditions of small scale yielding are met the following equation can be used to approximate the plastic zone radius.

$$R_o = \frac{1}{3\pi} \left( \frac{K_o}{\sigma_y} \right)^2 \quad \text{Eq. 4.4}$$

where  $R_o$  is the plastic zone radius,  $\sigma_y$  is the material yield stress. Eq. 4.3 and Eq. 4.4 were utilized to normalize the toughness ( $K_r$ ) and the instantaneous crack length ( $a$ ). The crack length was determined from the model by examining the failure of the cohesive elements along the ligament.

### 4.3 Verification of the SSY Model

To verify the SSY model, the analysis presented in the work of (Tvergaard & Hutchinson, 1992) was repeated using the present model and compared to the results of the original work. The main point of comparison was that of the non-dimensional crack growth resistance curves. The critical stress intensity factor and plastic zone size for all models are listed in Table 4.6. The data generated in the original work can be seen compared to the data from the present effort in Figure 4.10. As can be seen, the data generated from the present model is in very good agreement with the original data. Of the four sets there is a maximum difference of 11% with the TH-1 model. The other three sets of data produced much more agreeable results with average differences less than 5%.

#### **4.4 Results and Discussion – Effect of the TSL Shape on Crack Growth Resistance and the CTOA**

The SSY model was used to examine the effect of the TSL shape on the response of the non-dimensional crack growth resistance curves and the CTOA. Only the X70 material was used in the analysis. The TSL parameters determined from the calibration in Section 3.2 were used for the analysis; however, the shape of the TSL was changed to the shapes discussed in Section 4.1.4. Specifically, the effect of the size of the maximum traction region (plateau size) was assessed. The TSL shapes examined were presented in Section 4.1.4, each of the shapes have the same cohesive stiffness, maximum traction, and cohesive energy, thus the only parameter effected is the length of the maximum traction region.

The non-dimensional crack growth resistance data is plotted in Figure 4.11. The critical stress intensity value ( $K_o$ ) and plastic zone size ( $R_o$ ) for all four models was 4587.3 MPa $\sqrt{\text{mm}}$  and 6.73 mm, respectively. The general trend of the results indicates that increasing the size of the plateau region causes an increase in the model's resistance to a propagating crack. Intuitively this makes sense as the cohesive elements can sustain the maximum traction for a larger displacement. This then requires a larger driving force to propagate the crack. The most noticeable increase is observed when comparing the bilinear data to the trapezoidal-1/4 data. Once the maximum traction is maintained the resistance to crack growth is noticeably increased.

The trend of increasing crack growth resistance with increasing plateau size was also seen with the CTOA. The CTOA was extracted from the model using the method presented in Section 2.3.1. The CTOA as a function of crack extension can be seen in

Figure 4.12. The average steady-state CTOA from the models are tabulated in Table 4.7. The average steady-state CTOA is increased with increasing the plateau size. The most noticeable change is observed between the bilinear shape and the trapezoidal-1/4 shape. Once the maximum traction is maintained (trapezoidal-1/4), instead of immediate loss of carrying capacity (bilinear), the CTOA is increased quite noticeably from 7.3° to 11.4°. Moreover, it is also noticeable the small amount the CTOA changed after the maximum traction was maintained. This is observed by comparing the trap-1/4, trap-1/2 and trap-3/4. Once the maximum traction is maintained, there is little difference between the measured CTOA's.

The significance of these results pertains to the implementation of the update for the TSL with respect to increasing loading rate. It was shown that changing the shape of the TSL can have an effect on the crack growth resistance and the CTOA. It was decided that the update to the TSL would only affect the magnitude of the cohesive energy and the maximum traction, while maintaining the same shape.

#### **4.5 Conclusions**

The purpose of this chapter was to examine the effect of the shape of the TSL on crack growth resistance and the CTOA. This was achieved through the examination of an SSY model with different TSL shapes, but identical parameters ( $\Gamma_0=98$  MPa-mm and  $T_n^0=1850$  MPa). Prior to the use of the model, it was verified by repeating the crack growth resistance data from the work of (Tvergaard & Hutchinson, 1992). The data generated from the model presented herein was in good agreement with that of the original work. The results of this study demonstrate that given the same TSL parameters, the shape of the

TSL has a significant effect on the results of the analysis. The specific trend was that increasing the plateau size would cause an increase in the crack growth resistance and the CTOA. The most noticeable of changes in the results was observed by comparing the bilinear shape to the trapezoidal-1/4.

In conclusion, it was found that the shape of the TSL (increasing the plateau size) will cause an increase in crack growth resistance and an increase in CTOA for the same parameters.

**Table 4.1 – TH steel stress and plastic strain data. (ABAQUS input)**

True stress (MPa)	Plastic strain	True stress (MPa)	Plastic strain	True stress (MPa)	Plastic strain
600	0.00000	800	0.05027	1000	0.49315
610	0.00054	810	0.05732	1010	0.54505
620	0.00116	820	0.06519	1020	0.60180
630	0.00189	830	0.07398	1030	0.66378
640	0.00272	840	0.08378	1040	0.73142
650	0.00368	850	0.09468	1050	0.80517
660	0.00478	860	0.10680	1060	0.88552
670	0.00604	870	0.12025	1070	0.97299
680	0.00749	880	0.13518	1080	1.06814
690	0.00914	890	0.15171	1090	1.17156
700	0.01101	900	0.17000	1100	1.28387
710	0.01315	910	0.19021	1110	1.40576
720	0.01558	920	0.21252	1120	1.53795
730	0.01832	930	0.23713	1130	1.68120
740	0.02143	940	0.26423	1140	1.83632
750	0.02494	950	0.29406	1150	2.00418
760	0.02890	960	0.32685	1160	2.18571
770	0.03335	970	0.36287	1170	2.38188
780	0.03836	980	0.40239	1180	2.59374
790	0.04398	990	0.44570	1190	2.82239

**Table 4.2 - TH TSL parameters for verification analysis.**

TSL Name	Cohesive Stiffness (MPa/mm)			Cohesive Strength (MPa)			Cohesive Energy (MPa)
	$K_{nn}$	$K_{ss}$	$K_{tt}$	$T_n^o$	$T_s^o$	$T_t^o$	
TH-1	$6.0 \times 10^5$	$2.31 \times 10^5$	$2.31 \times 10^5$	1850	1350	1350	24.3
TH-2	$7.0 \times 10^5$	$2.69 \times 10^5$	$2.69 \times 10^5$	2100	1575	1575	28.35
TH-3	$7.2 \times 10^5$	$2.77 \times 10^5$	$2.77 \times 10^5$	2160	1620	1620	29.26
TH-4	$7.5 \times 10^5$	$2.88 \times 10^5$	$2.88 \times 10^5$	2250	1687.5	1687.5	30.375

**Table 4.3 - X70 TSL naming convention.**

TSL Name	$\frac{\delta_2}{\delta_F}$
Bilinear	N/A
Trapezoidal -1/4	0.25
Trapezoidal -1/2	0.5
Trapezoidal -3/4	0.75

\*the  $\frac{\delta_2}{\delta_F}$  ratio is with reference to Figure 3.2.

**Table 4.4 - X70 TSL parameters.**

Material	Cohesive Stiffness (MPa/mm)			Maximum Traction (MPa)			Cohesive Energy (MPa-mm)	
	Symbol	$K_{nn}$	$K_{ss}$	$K_{tt}$	$T_n^o$	$T_s^o$		$T_t^o$
X70		$2 \times 10^6$	$7.69 \times 10^5$	$7.69 \times 10^5$	1850	1387.5	1387.5	$\Gamma_o$
								98

**Table 4.5 - SSY model FE mesh specifications.**

Material	Part	Zone	Element Types	Number of Elements	Nominal Size (mm)
TH	SSY	Ligament	CPE4R	48000	0.33x0.33
		Transition	CPE4R/ CPE3	27728	N/A
		Bulk	CPE4R	1724	N/A
	Crack	Cohesive Layer	COH2D4	4500	0.2x0.001
X70	SSY	Ligament	CPE4R	6000	0.3x0.3
		Transition	CPE4R/ CPE3	4812	N/A
		Bulk	CPE4R	6080	N/A
	Crack	Cohesive Layer	COH2D4	12987	0.077x0.001

**Table 4.6 - TH steel parameters.**

Material	$T_n^o/\sigma_y$	Cohesive Energy (MPa-mm)	$K_o$ (MPa $\sqrt{\text{mm}}$ )	$R_o$ (mm)
TH-1	3	24.3	2311.0	1.574
TH-2	3.5	28.35	2496.2	1.836
TH-3	3.6	29.26	2535.9	1.895
TH-4	3.75	30.375	2583.8	1.968

**Table 4.7 - SSY model average steady-state CTOA.**

TSL Shape	Average Steady-State CTOA (Degrees)
Bilinear	7.3
Trapezoidal -1/4	11.4
Trapezoidal -1/2	12.1
Trapezoidal -3/4	12.6

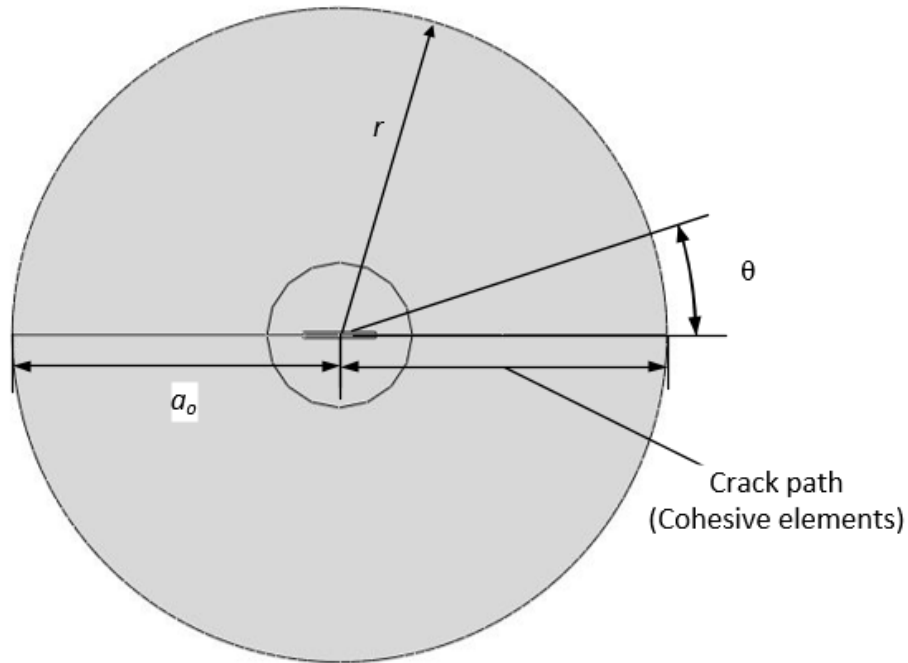


**Figure 4.1 - SSY model geometry.**

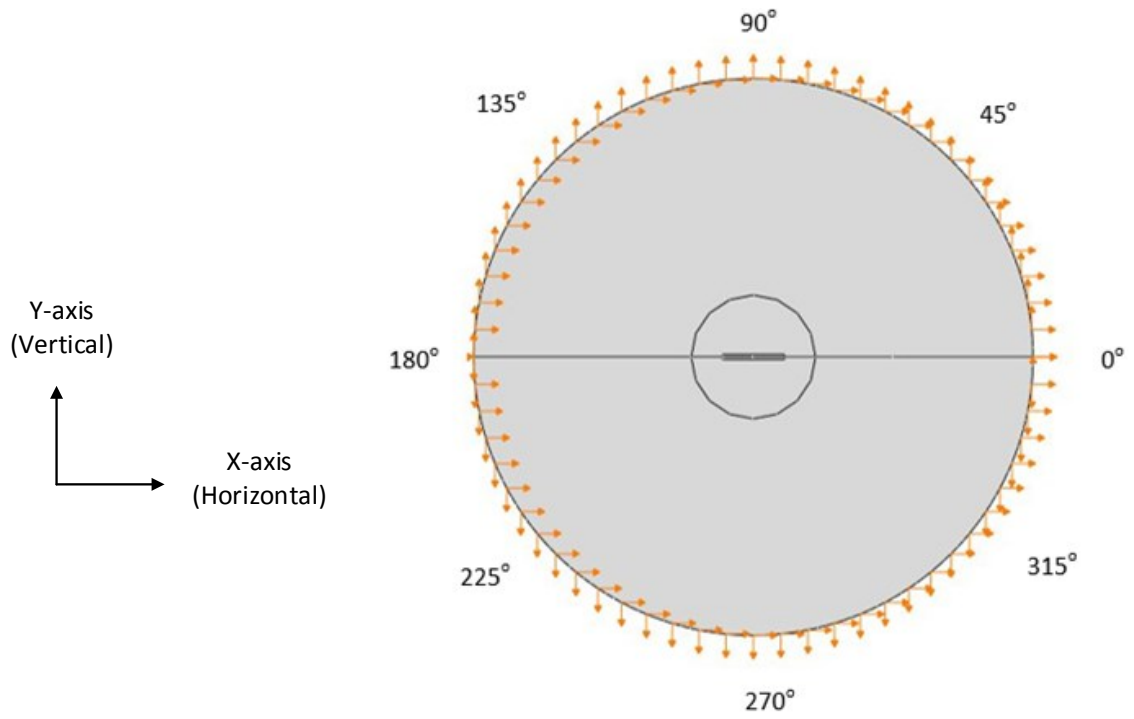


**Figure 4.2 - SSY model loading conditions.**

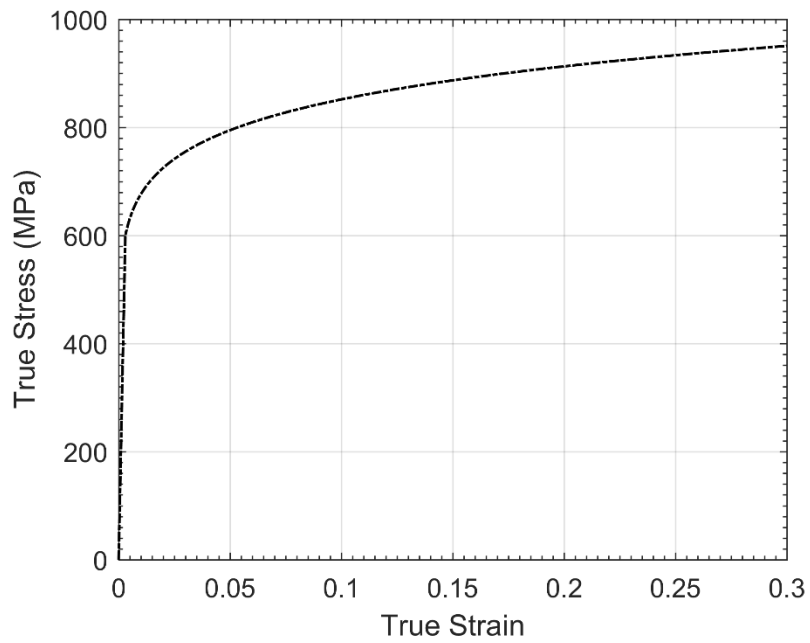


**Figure 4.3 - TH steel true stress-true strain data.**

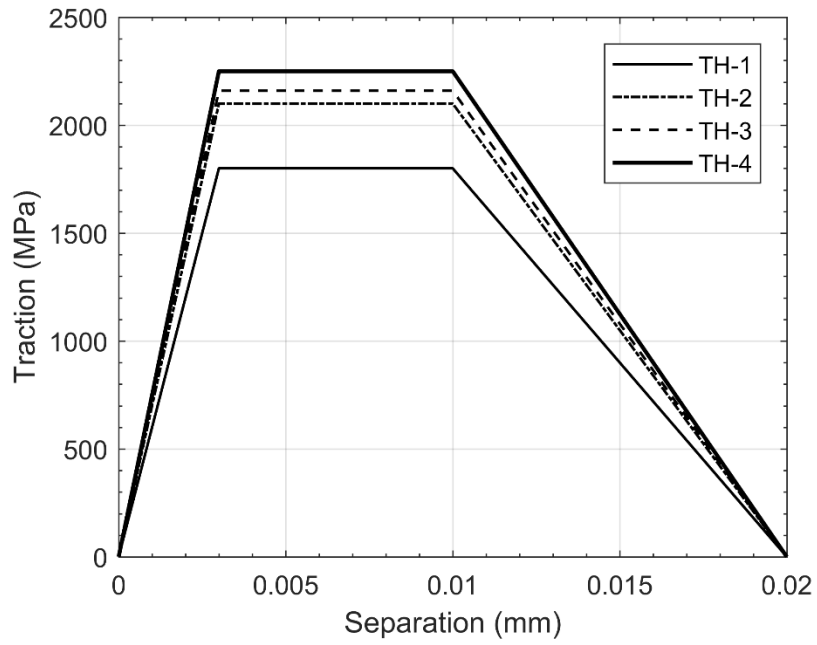


**Figure 4.4 - TSL used for verification analysis.**

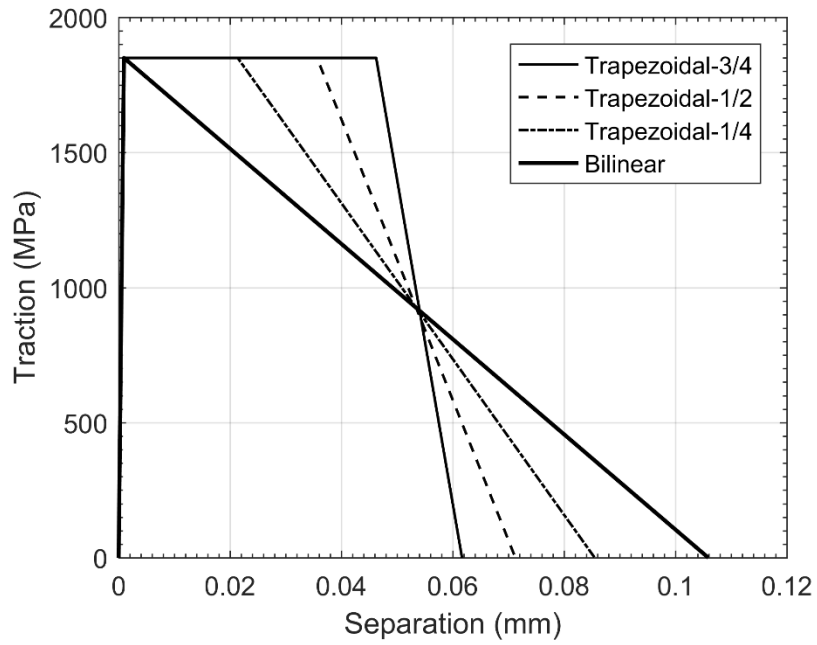


**Figure 4.5 - X70 TSL's.**

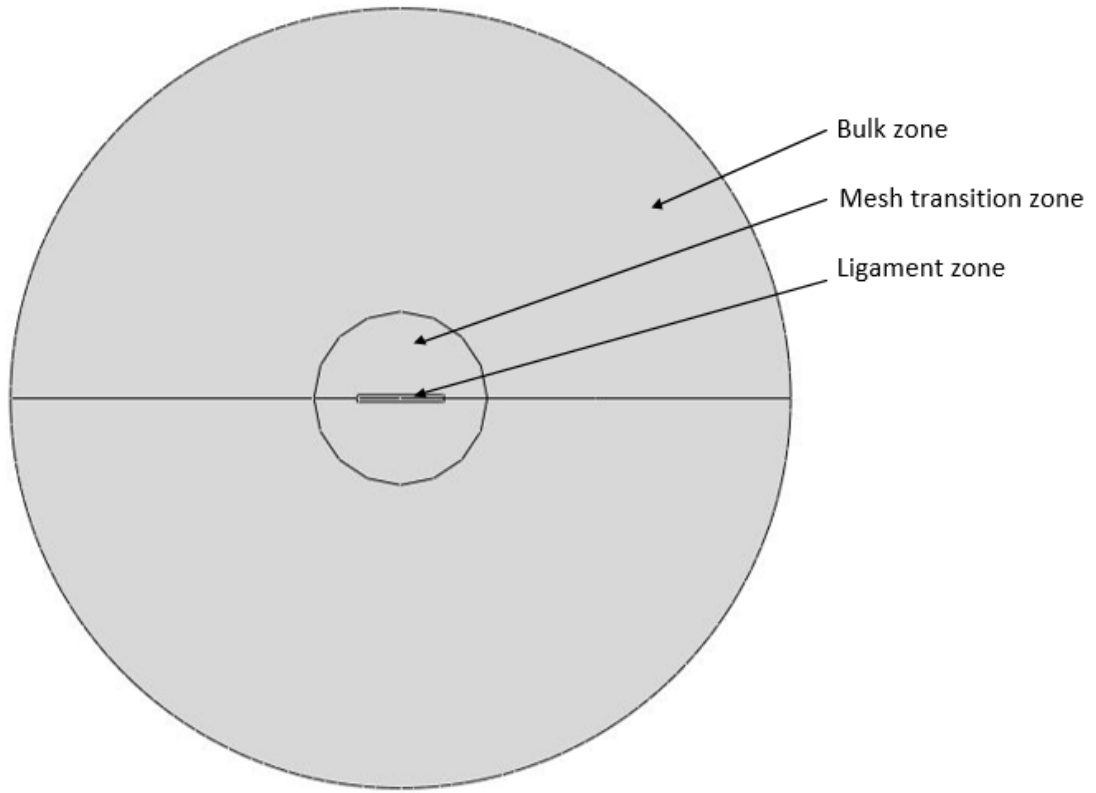


**Figure 4.6 - SSY model FE mesh zones.**

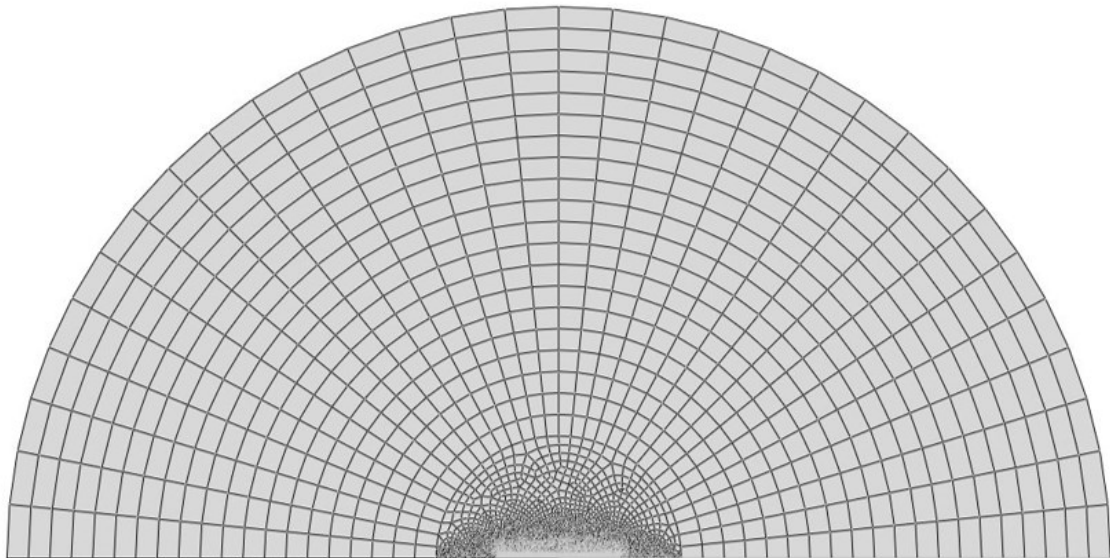


**Figure 4.7 - SSY model FE mesh - half model.**

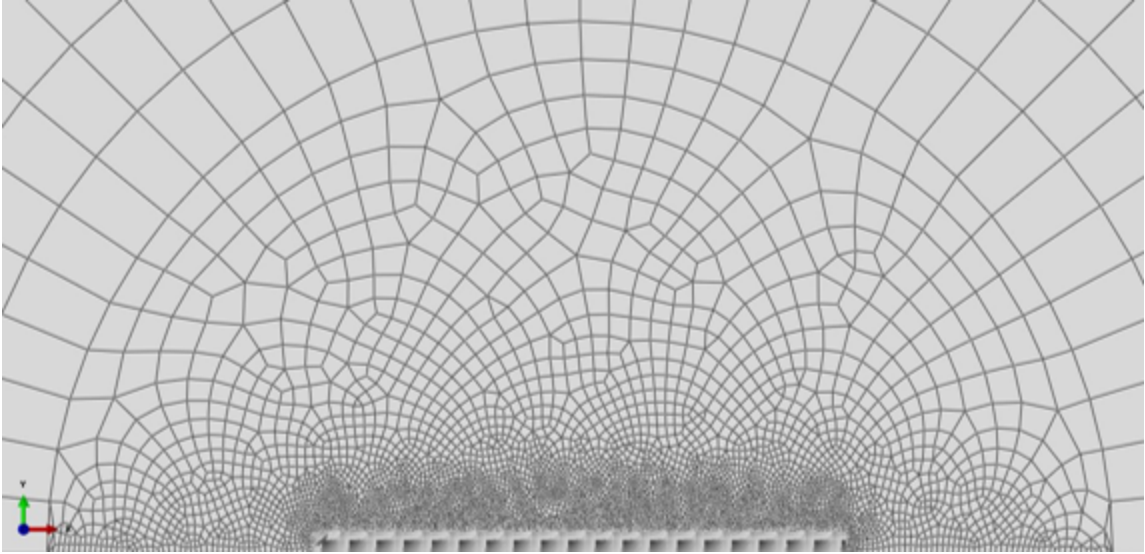


**Figure 4.8 - SSY model mesh transition zone.**

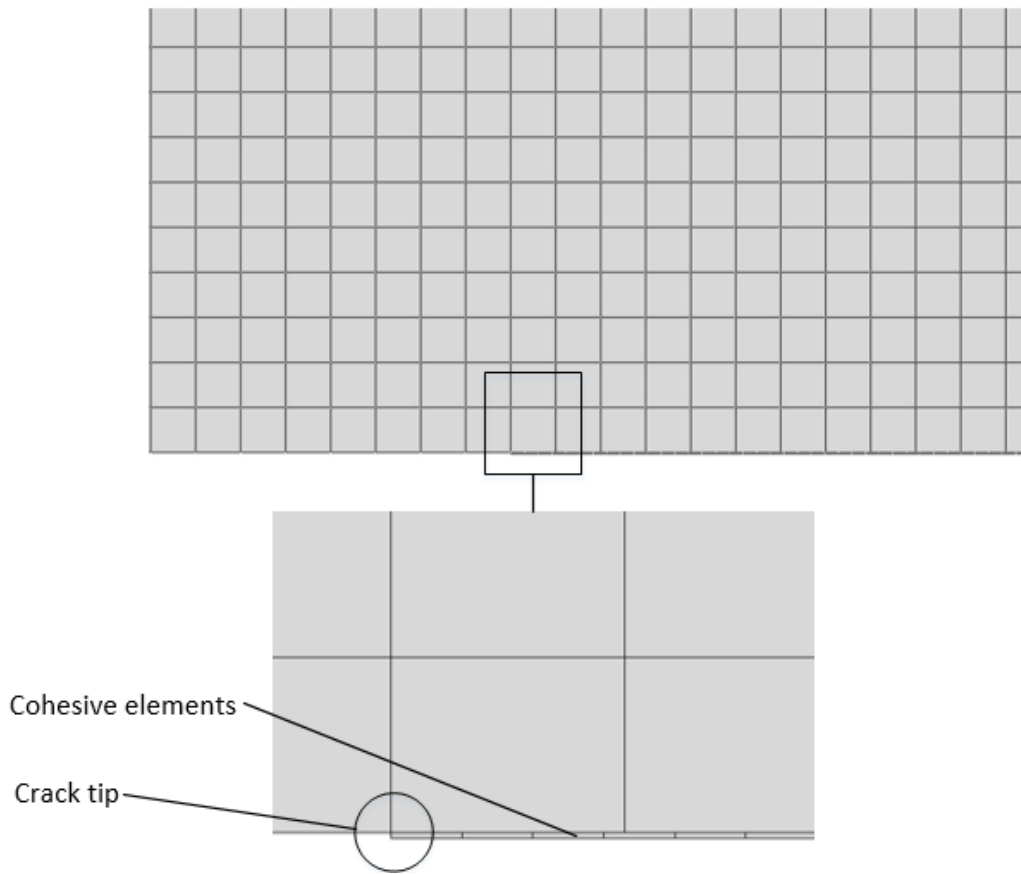


**Figure 4.9 - SSY model ligament mesh.**

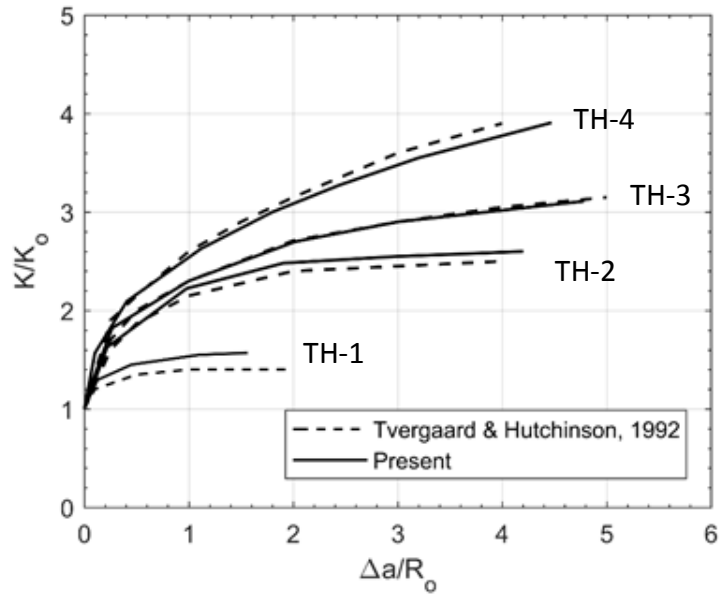


Figure 4.10 - SSY model verification using TH steel.

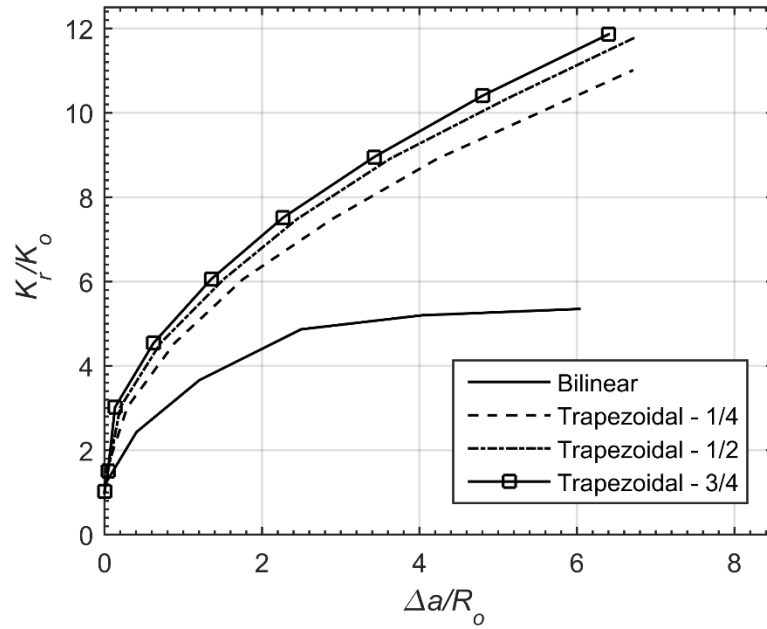
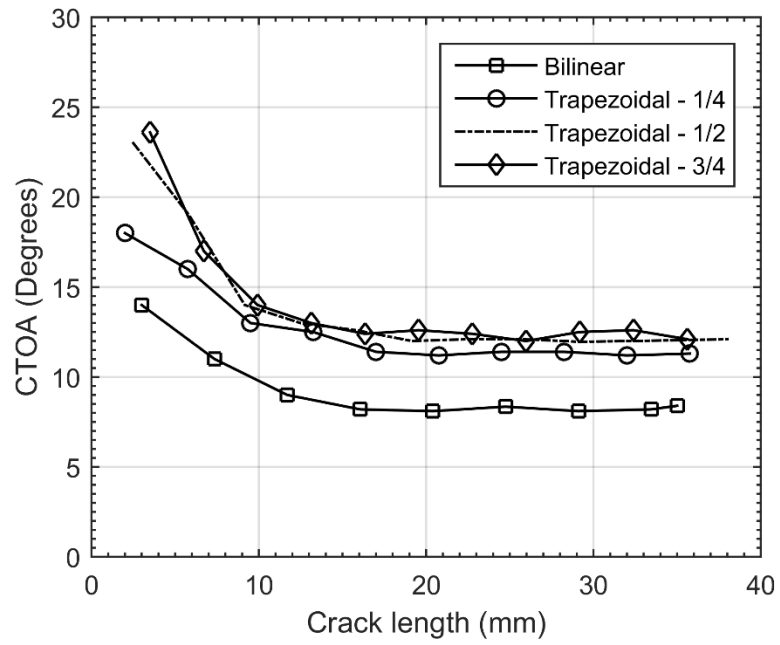


Figure 4.11 - Non-dimensional crack growth resistance data examining the effect of the plateau size.



**Figure 4.12 - CTOA as a function of crack extension - X70.**

## **Chapter 5: FE Simulations of a Single Edge Notch Tension Specimen under Quasi-static Loading Conditions**

The level of constraint at the tip of a crack is a parameter long known to effect the manner in which a crack propagates. It is well known that various factors affect the crack tip constraint, such as specimen geometry, material parameters, and loading mode. It is the objective of this chapter to address the effect of loading mode on the CTOA. This was achieved through a comparative analysis between a clamped single edge notched tension (SENT) model presented in this chapter, and the quasi-static DWTT model presented in Chapter 6. The clamped SENT specimen was chosen for the tensile specimen as it was shown in the work of (Shen, Bouchard, Gianetto, & Tyson, 2008) that this specimen with an  $H/w$  ratio of 10, replicates the constraint seen in a circumferentially flawed pipe. All simulations performed and analyzed in this chapter were under quasi-static loading conditions.

### **5.1 Clamped Single Edge Notch Tensile (SENT) Specimen Model**

A two-dimensional plane strain clamped SENT model was generated and analyzed using the commercial finite element code ABAQUS 6.14-2 (Dassault Systemes, 2014). This section presents the computational model including the geometry, loading conditions, material properties, cohesive properties and mesh design.

#### **5.1.1 Geometry and Computational Procedures**

The geometry of the SENT model is illustrated in Figure 5.1. The model was divided into two parts and the cohesive elements were inserted along the crack path,

illustrated in Figure 5.4. The width of the model and the initial crack length were kept the same as the DWTT model, namely,  $W=76$  mm and  $a_0=10$  mm, respectively. The thickness of the specimen was kept the same as the thickness of the pipe which the material operates in practice, specifically X70 had a thickness of 13.7 mm and X100 had a thickness of 14.6 mm. This thickness was the out of plane thickness of Figure 5.1. The height of the model was chosen such that the daylight (distance between the fixed end constraints) was equal to  $10W$ . Specifically, the height of half the model was  $H=360$  mm, for a total daylight of  $2H=760$  mm.

The clamped regions, marked  $H^*$  in Figure 5.1, were assigned an arbitrary length of 20 mm. This length is irrelevant as the clamped region is fully constrained to the reference point as illustrated in Figure 5.2.

### **5.1.2 Loading Conditions**

To model the clamped end conditions, the top and bottom sections of the model, marked with length  $H^*$  in Figure 5.1, were constrained to a reference point within the model assembly using a rigid body constraint. This is illustrated in Figure 5.2. The loading conditions were then applied to the reference point. A fixed boundary condition was placed on the bottom reference point. This boundary condition restricted linear motion in the X and Y axes, as well as restricted rotation about the Z axis (out of plane axis). A boundary condition restricting linear motion in the X-axis and rotation about the Z-axis was placed on the top reference point. To induce fracture a vertical displacement was placed on the top reference point. The displacement was ramped from 0 to 20 mm over the analysis step.

A displacement rate of 5 mm/s was used. The boundary conditions are illustrated in Figure 5.2.

### **5.1.3 Material Properties**

The material properties used in the analysis were presented and discussed in Section 2.3. As this is only a quasi-static analysis, the material parameters implemented into the model were listed in Table 2.3. The true stress and plastic strain data was tabulated in Table 2.5 and Table 2.6 for X70 and X100, respectively.

### **5.1.4 Cohesive Zone Properties**

The cohesive zone properties used in the analysis were presented and discussed in Section 3.2. The specific parameters used in this analysis are presented in Table 3.3. These are the same parameters used in the quasi-static DWTT analysis.

### **5.1.5 SENT FE Mesh Design**

The SENT model was partitioned into three zones, the ligament zone, a mesh transition zone and the bulk zone. These zones are illustrated in Figure 5.3. The mesh design of the SENT model is shown in Figure 5.4. The bulk zone was meshed using structured 4 node plane strain quadrilateral elements. The mesh transition zone was meshed using a free technique with a combination of four node plane strain quadrilateral elements and three node plane strain triangular elements. The ligament zone was assigned structured four node plane strain elements with an aspect ratio of 1 to prevent uneven deformation. The details of the mesh for both materials are listed in Table 5.1 including

element type, number of elements and nominal sizing. Though the two materials examined utilized different sized meshes, both models were meshed in the same manner.

## **5.2 Analysis Methodology**

The methodology used to examine the effect of the loading mode on the CTOA was to compare a bending model to a tensile model under quasi-static loading conditions. The tensile model, presented in the previous section, was compared to a bending model supplemented by the quasi-static DWTT model presented in Section 6.1.

Both models were specified the same material model, mesh sizing, and cohesive parameters. The only difference between the two models was the mode in which they were loaded. The effect of the loading mode on the crack tip constraint was quantified through the level of stress triaxiality at the crack tip. It is commonly known that a tensile model will produce a state of low triaxiality, and a bending model will produce a state of high triaxiality. For the purposes of the discussion the triaxiality at the crack tip is defined as the ratio of the hydrostatic stress to the material yield stress.

## **5.3 Results and Discussion – Effect of Loading Mode on the CTOA**

The effect of loading mode was examined through a comparative analysis between a tensile model (SENT) and a model which was subjected to a bending loading mode (quasi-static DWTT). For the purposes of the discussion the SENT model will be referred to as the tensile model and the DWTT model will be referred to as the bending model. The following sections present and discuss the results for the two materials examined. The CTOA was extracted from the models as presented in Section 2.3.1.

### *X70 Results*

The crack tip triaxiality as a function of crack extension can be seen in Figure 5.5 for both the bending model and the tensile model. As would be expected the tensile model produces a lower state of stress triaxiality at the crack tip throughout propagation than the bending model. This trend is seen throughout the propagation of the crack through the ligament.

The CTOA as a function of crack extension is plotted in Figure 5.6. The extension of the crack is the length extended through a ligament of 66 mm. The CTOA was extracted from the models in the same manner as discussed in Section 2.3.1. As expected the CTOA is initially large and decreases steadily towards the steady-state value. The steady-state region begins after 20mm of crack extension. The CTOA extracted from the bending model is consistently lower than the CTOA extracted from the tensile model. The bending model has an average steady-state CTOA of  $12.2^\circ$  and the tensile model had an average steady-state CTOA of  $13.3^\circ$ . This slight offset was seen throughout the propagation of the crack through the ligament. This shows that the loading mode (constraint) has a secondary effect on the CTOA measured from the model.

### *X100 Results*

The crack tip triaxiality as a function of crack extension can be seen in Figure 5.7. Similar to the X70 results, the bending model produced a state of high triaxiality and the tensile produced a state of lower triaxiality. The CTOA as a function of crack extension is plotted in Figure 5.8. Similar to the X70 results, there is a slight effect of crack tip triaxiality on the CTOA, as the tensile model produced a slightly higher CTOA than the

bending model. The average steady-state CTOA of the bending model was 10.1°. The average steady-state CTOA of the tensile model was 12.6°. This dissimilarity to the X70 material indicates that the CTOA of the higher strength steel is more sensitive to the level of constraint at the tip of the crack.

It is interesting to note that the CTOA appears to be affected by the level of triaxiality at the crack tip. As seen with the X100 material, shortly after crack initiation ( $a < 20$  mm) the triaxiality at the crack tip begins relatively low and increases, as shown in Figure 5.7. Over the same range the CTOA begins at a high value and rapidly decreases, as seen in Figure 5.8. Once the model reaches a steady-state propagation region the triaxiality begins to stabilize, and the CTOA does the same. This same trend was observed with the X70 material as well. This offset of triaxiality, throughout the steady-state region, also explains the slight offset of the CTOA.

However, the measured CTOA for both loading modes are still in a relatively close range of one another. It can be deduced that the level of constraint at the crack tip has a secondary effect on the CTOA, with respect to loading mode. A similar result was observed for the X70 material as well. This analysis reinforces the notion that the CTOA is transferrable between loading modes.

## **5.4 Conclusions**

This chapter analyzed the effect of loading mode on the CTOA. This was achieved through a comparative analysis between a bending model (high constraint) and a clamped tensile model (low constraint). The analysis was performed on both X70 and X100. Both

models were assigned the same material properties, cohesive properties and mesh design to highlight the effect of the different loading mode.

The CTOA of the bending model and the tensile model were comparable for both materials examined. There was a slight offset of CTOA observed for both X70 and X100; however, they were both in good agreement. The CTOA of X100 displayed a higher level of sensitivity to the level of constraint at the crack tip. This work reinforces the notion that the CTOA is transferrable between loading modes.

**Table 5.1 - SENT Mesh Details.**

Material	Part	Zone	Element Types	Number of Elements	Nominal Size (mm)
X70	SENT Specimen	Ligament	CPE4R	5060	0.3X0.3
		Transition	CPE4R/ CPE3	2258	N/A
		Bulk	CPE4R	184	6X10
	Crack	Cohesive Layer	COH2D4	799	0.077x0.01
X100	SENT Specimen	Ligament	CPE4R	872	0.48X0.48
		Transition	CPE4R/ CPE3	1206	N/A
		Bulk	CPE4R	184	6X10
	Crack	Cohesive Layer	COH2D4	289	0.15X0.01

-Note: the number of elements listed is for a full model.

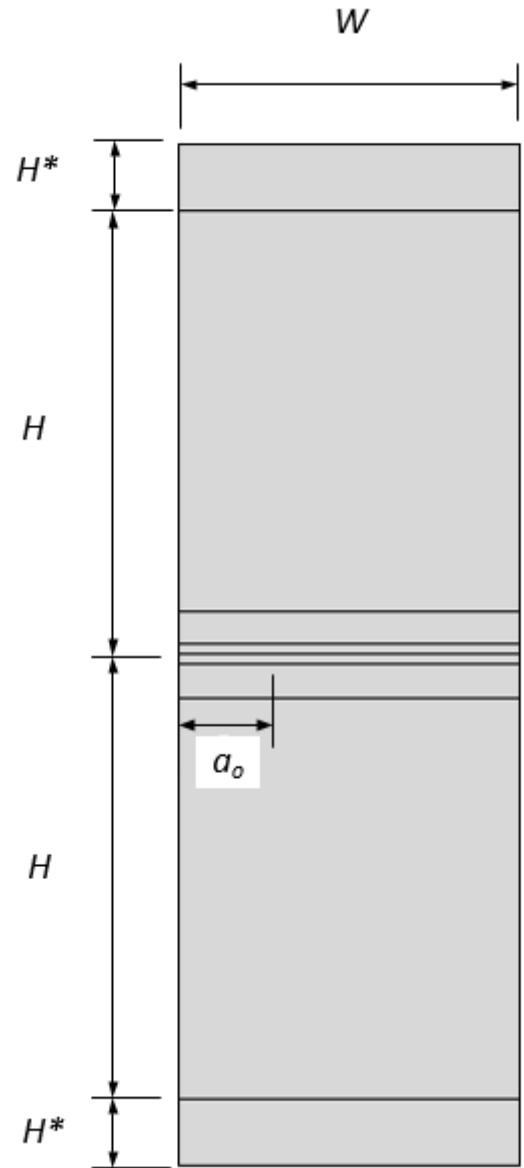


Figure 5.1 - SENT model dimensions - Not to scale.

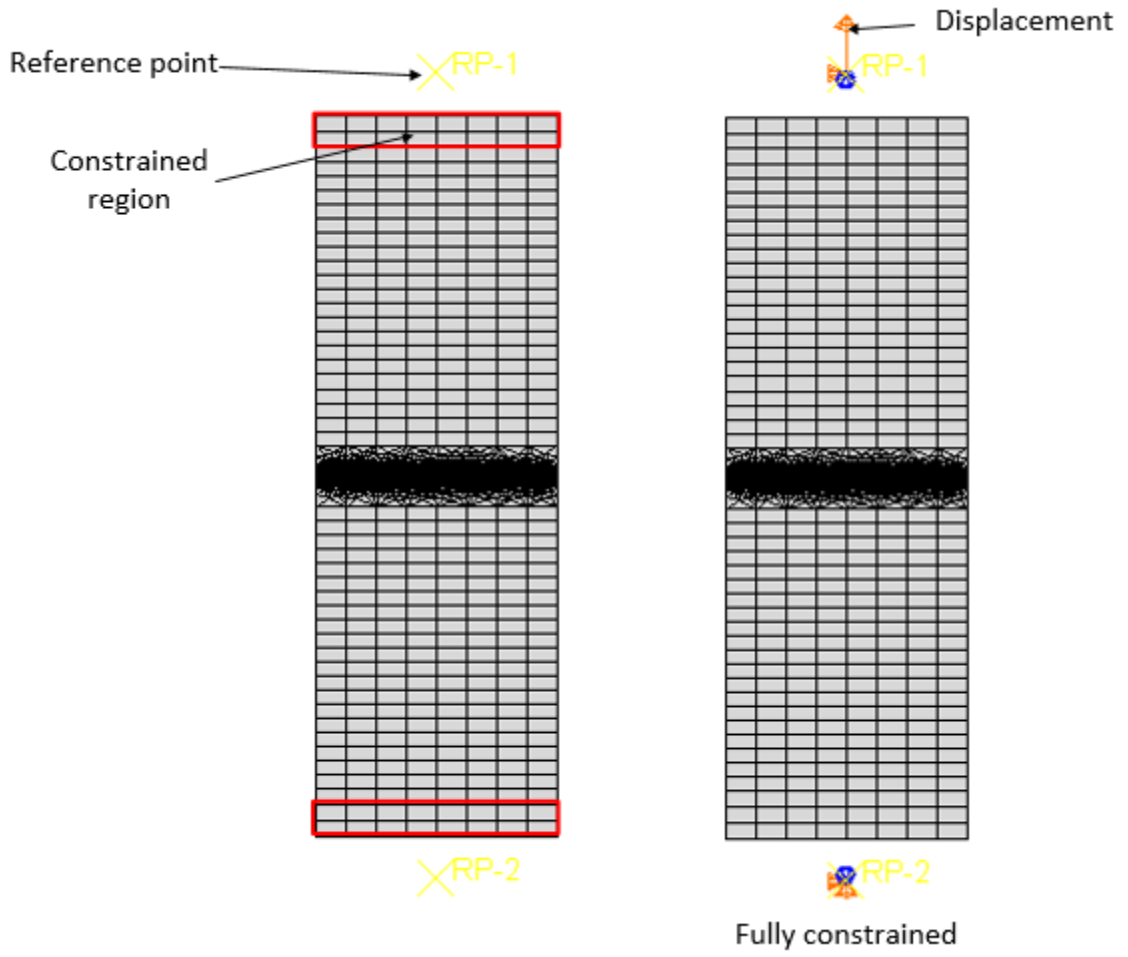
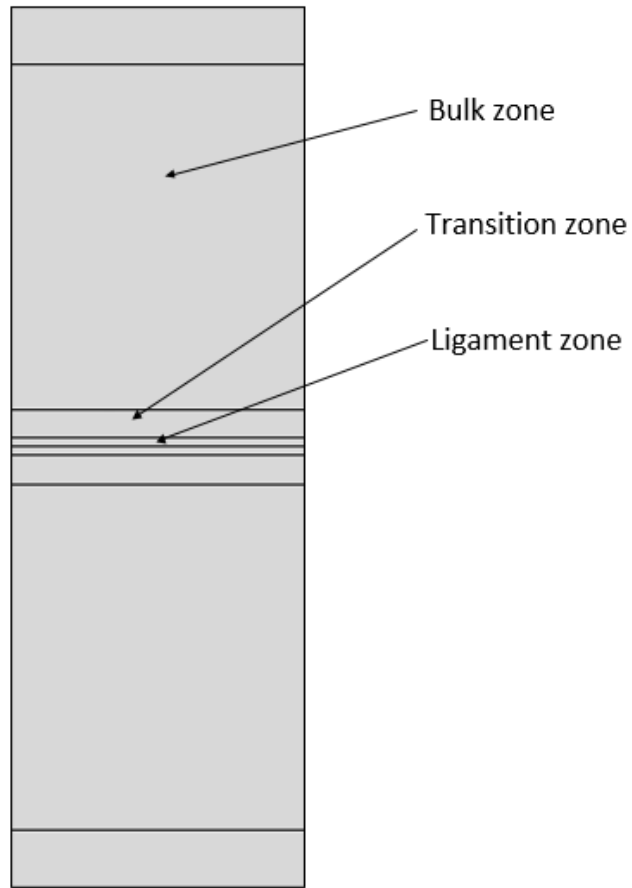
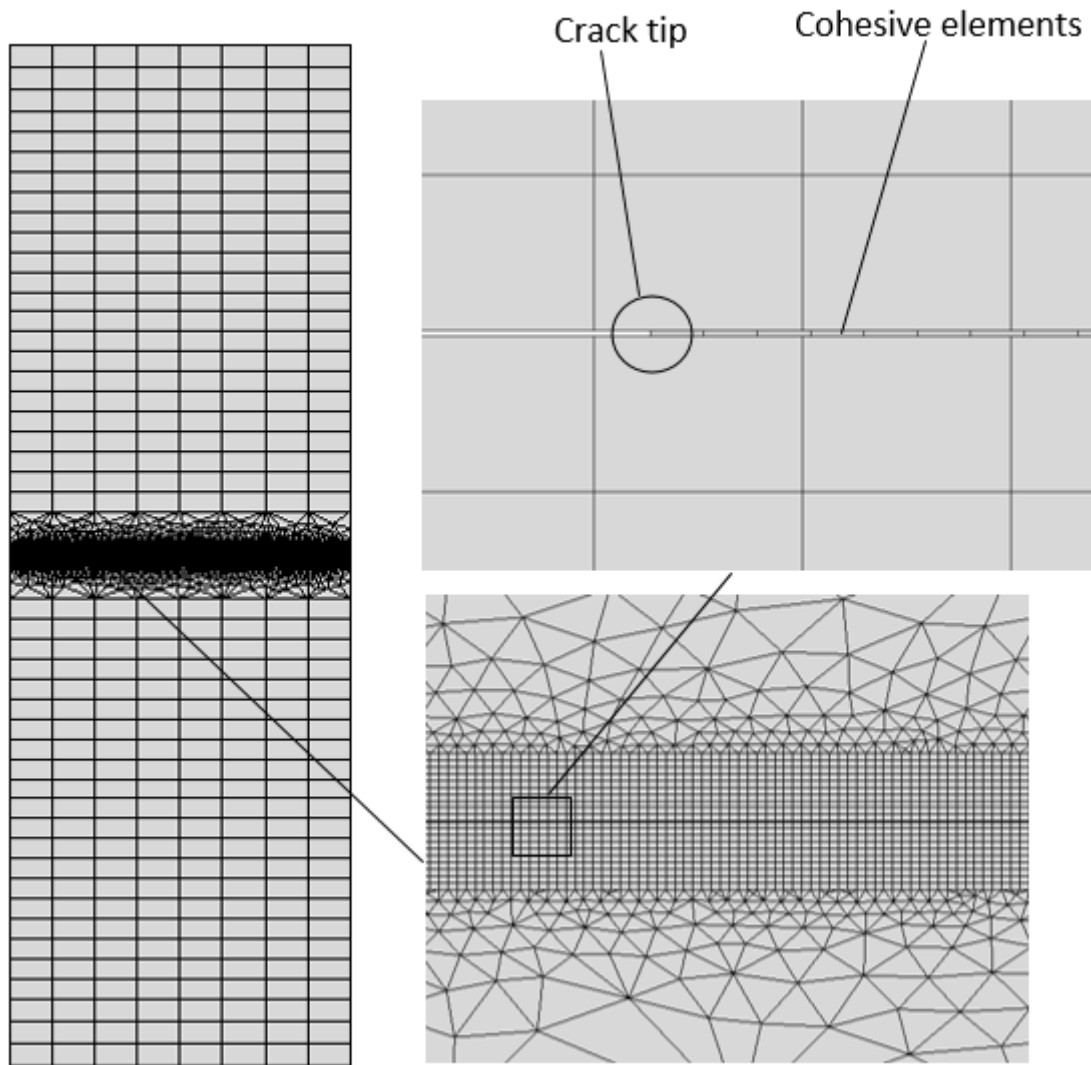


Figure 5.2 - SENT model loading conditions - Not to scale.



**Figure 5.3 - SENT FE mesh zones.**



**Figure 5.4 - SENT model FE mesh design.**

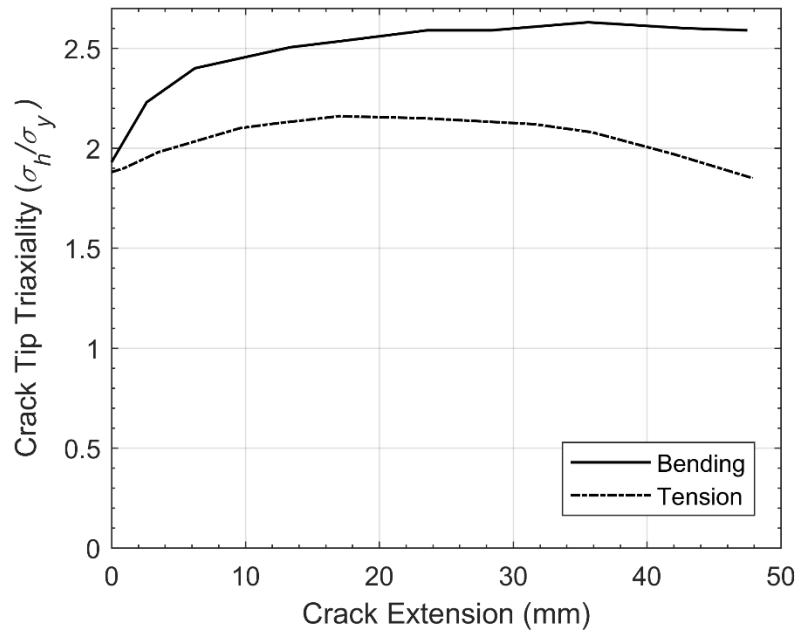


**Figure 5.5 - Crack tip triaxiality as a function of crack extension - X70.**

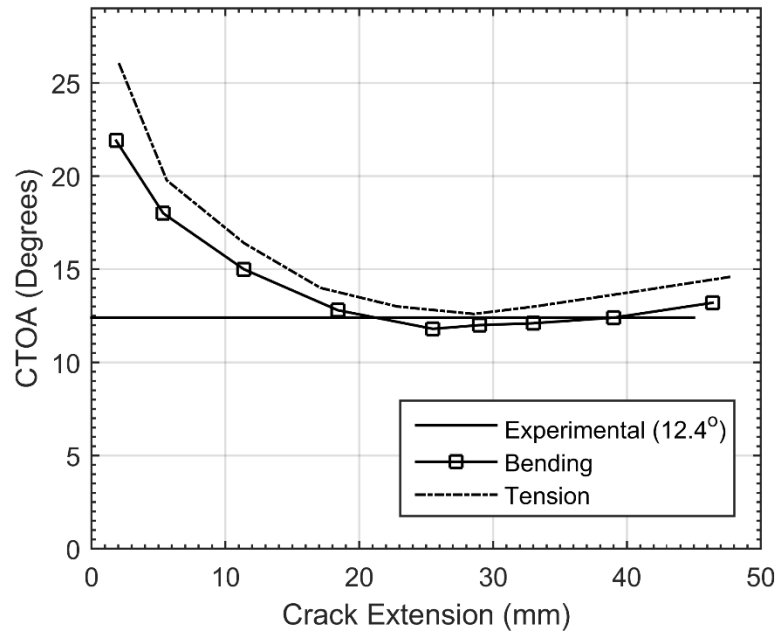


**Figure 5.6 - CTOA as a function of crack extension - X70.**

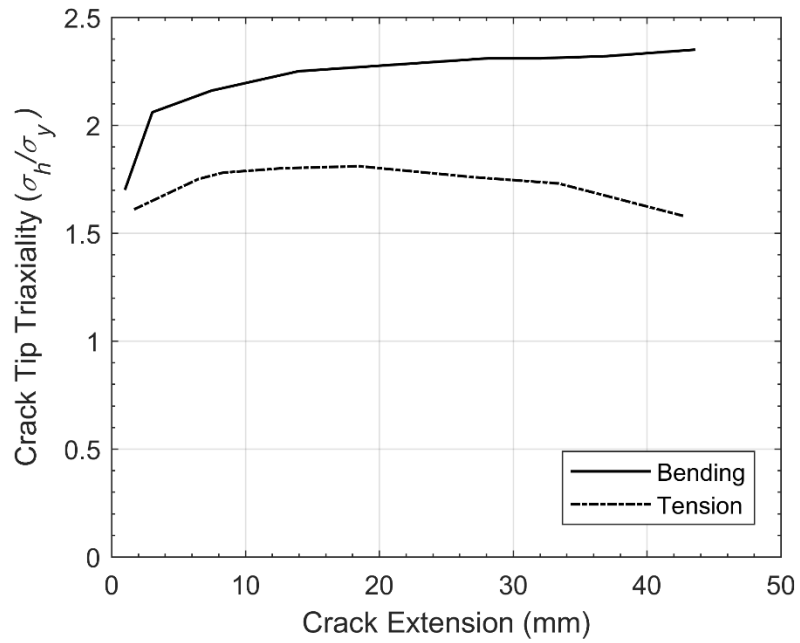


Figure 5.7 - Crack tip triaxiality as a function of crack extension – X100.

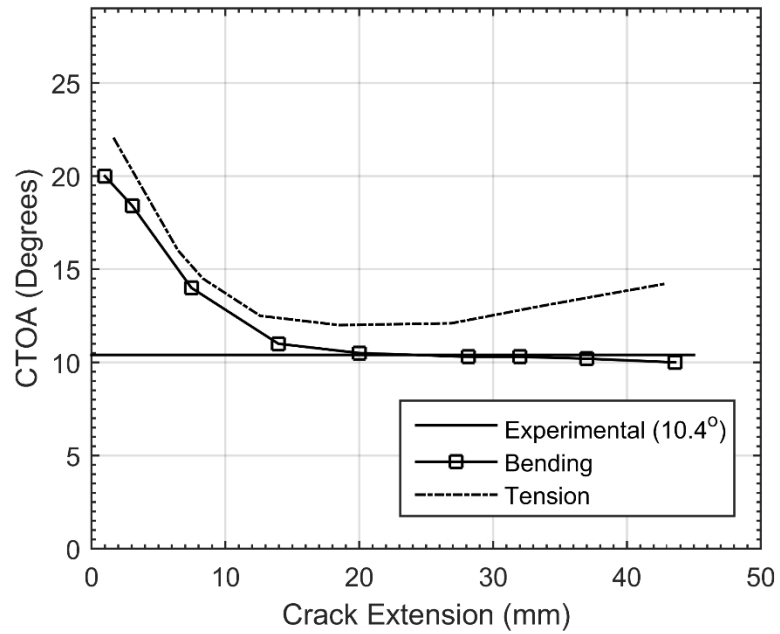


Figure 5.8 - CTOA as a function of crack extension – X100.

## **Chapter 6: FE Simulations of a Drop Weight Tear Test Specimen under Quasi-static Loading Conditions**

This chapter presents the finite element simulations of a DWTT specimen under quasi-static loading conditions. The DWTT model was examined at two different rates of loading; a quasi-static loading rate and an impact loading rate. This chapter focuses on the quasi-static loading conditions, the following chapter will address the impact loading rate. Both loading rates were characterized experimentally at CanmetMATERIALS (Xu S. , 2016b). The experimental data was provided for comparison with the FE results and will be discussed later. This chapter presents the computational model including geometry, computational methods, assumptions, loading conditions, and mesh design. The results of the analysis are presented and compared to the experimental results.

### **6.1 Drop Weight Tear Test (DWTT) Model**

Two-dimensional plane strain simulations of a DWTT specimen were performed using ABAQUS Explicit 6.14-2 (Dassault Systemes, 2014). The purpose of this analysis was to examine the DWTT model under quasi-static loading conditions with the CZM calibrated in Chapter 3. Furthermore, the use of the trapezoidal TSL shape to simulate ductile fracture was examined. As well this analysis also assesses the use of the CTOA as a calibration parameter for the CZM. This section outlines the computational model including geometry, computational procedures, material properties, loading conditions and mesh design.

### **6.1.1 Geometry and Computational Procedures**

The geometry of the specimen examined was consistent with that presented in the ASTM standard E436-03, as seen in Figure 2.6. Specimens were the full thickness of the pipe in which they operate in service; X70 and X100 had a thickness of 13.7 mm and 14.6 mm, respectively. The height, width and initial length of the notch were 76 mm, 305 mm and 10 mm, respectively. The model is illustrated in Figure 6.1. The machined notch tip was ignored and replaced with a sharp notch for the simulations presented herein. This simplification is illustrated in Figure 6.2. This was done to simplify the mesh design as well to prevent complications from large amount of plastic strain prior to propagation. As the intention of this model is to study crack propagation, it was determined through a comparison with 3-D FE simulations that the notch tip affected the extent of plastic deformation prior to crack propagation and not the steady-state portion i.e. the slope of the post-initiation section of the Load-LLD curve.

The hammer was modeled as an analytical rigid surface constrained to a reference point within the model assembly. This is illustrated in Figure 6.1. The contact interaction between the specimen and the hammer was modelled as ‘hard contact’ in the normal direction and frictionless in the tangential direction. The vertical supports were modelled as a boundary condition on the specimen by constraining 6 nodes (6 mm in total length) on the bottom surface in the vertical direction. This was done to simplify the computational model and remove the necessity to model the contact interaction between the specimen and the vertical supports.

Cohesive elements were inserted along the ligament; between the two flanks, as illustrated in Figure 6.1. The cohesive layer was constrained to the two flanks using a

surface-to-surface constraint. This constrained the nodes of the cohesive layer to the surface of the flank.

### **6.1.2 Material Properties**

The material properties of X70 and X100 and their implementation in the numerical model were presented and discussed in Section 2.6. The true stress-strain curves can be seen in Figure 2.12. The material properties used in the numerical analysis are presented in Table 2.3, the stress-plastic strain data was presented in Table 2.5 and Table 2.6 for X70 and X100, respectively.

### **6.1.3 Cohesive Zone Properties**

The cohesive parameters and their calibration were presented in Chapter 3. The quasi-static cohesive zone properties are presented in Table 6.1 for X70 and X100.

### **6.1.4 Loading Conditions**

The boundary conditions of the DWTT model are illustrated in Figure 6.1. The vertical supports were modelled as boundary conditions on the specimen. The boundary condition involved constraining motion in the Y-direction and rotation about the Z-axis (out of plane direction). The quasi-static loading rate was modeled using a displacement controlled simulation. A displacement was applied to the reference point and transmitted through the hammer. The loading rate was required to be sufficiently low such that inertial forces were considered negligible. A ramped displacement rate of 5mm/s was determined

to be adequate for the simulation, this was determined through trial and error comparing the results (CTOA and Load-LLD data).

### **6.1.5 Finite Element Mesh Design**

The mesh of the DWTT model was constructed specifically around the ligament. The model was partitioned into three regions; the ligament, a transition zone and the bulk remainder of the model. These sections are shown in Figure 6.3. Only half of the model's mesh is discussed as the other half was simply a mirror image through the vertical plane. The large bulk of the model was assigned four node plane strain quadrilateral elements. These elements utilized hourglass control to prevent undesirable deformation. The mesh transition zone utilized a combination of four node quadrilateral elements and three node tetrahedral elements. This mesh transition zone was integrated to accommodate a rapid change in mesh sizing between the ligament elements and the remainder of the model. The ligament elements were assigned structured four node plane strain quadrilateral elements with an aspect ratio of 1. The mesh of the entire model can be seen in Figure 6.4.

The specific details of the mesh including element type, number of elements and nominal sizing are presented in Table 6.2. The size of the cohesive elements was kept as small as possible. It is important to note that the mesh of the cohesive layer was the determining factor for the mesh sizing of the DWTT model, as discussed in Chapter 3. The mesh sizing and structure of the cohesive layer was discussed in Chapter 3.

## **6.2 Analysis Methodology**

The methodology used for this study was the same for both materials. The CZM was calibrated using the method presented in Section 3.2. The models were then analyzed under quasi-static loading conditions. Specifically, the CTOA as a function of extension and the Load-LLD data for each material was examined and compared with the experimental data.

## **6.3 Results and Discussion – Quasi-Static Loading Conditions**

This sections presents and discusses the results for the CTOA, and Load-LLD data for the quasi-static models.

### **6.3.1 CTOA**

The CTOA was determined from the models using the method presented in Section 2.3.1. Specifically, the nodes along the ligament behind the last failed cohesive element, were used to calculate a displacement vector. The displacement vector was calculated between two nodes. The components of the vector were used to calculate the CTOA.

#### *X70 Results*

The CTOA as a function of crack extension of the quasi-static model can be seen in Figure 6.5. The average CTOA determined from the model in the steady-state region was 12.2°. This value is in good agreement with the experimental value of 12.4°. As expected the CTOA is very high immediately after the crack initiates and then quickly declines to the steady-state value.

### *X100 Results*

The CTOA as a function of crack extension can be seen in Figure 6.6. The average CTOA determined from the model in the steady-state region was  $10.1^\circ$ . This value is in good agreement with the experimental value of  $10.4^\circ$ . Similar to the X70 material, the CTOA is initially large and descends to the steady-state value.

### **6.3.2 Load-Load Line Displacement**

The load-load line displacement (Load-LLD) data for the FE models were produced by extracting and correlating the instantaneous reaction load and vertical displacement of the hammer throughout the simulation.

### *X70 Results*

The quasi-static Load-LLD data for X70 can be seen in Figure 6.7. The Quasi-static model produces a curve which underestimates the maximum load of the experimental data. This is primarily due to the exclusion of the machined notch tip and the use of a plane strain model. The exclusion of the notch omits a significant portion of the plastic deformation prior to propagation. Furthermore, the plane strain assumption again does not account for the third dimensional deformation along the thickness of the ligament. The significant portion of this model however, is the ability to accurately reproduce the slope of the propagation portion of the Load-LLD curve.

Another mentionable quality of the model was the method in which it was calibrated. The TSL was calibrated by matching the experimental CTOA of the material.

It is interesting to note that calibrating the TSL so as to match the experimental CTOA produces a Load-LLD curve which matches the post-initiation slope (over the range of 10mm-20mm of LLD) of the experimental Load-LLD data. Agreement was verified visually through superimposing the FE data over the experimental data. The same result was seen for the X100 material.

### *X100 Results*

The quasi-static Load-LLD data for X100 can be seen in Figure 6.8. The quasi-static model produces an accurate curve matching the experimental data. Unlike the X70 material, the plane strain model does not under predict the maximum load. This inconsistency is likely due to the assumption of the shape of the TSL or due to the selection of the TSL parameters for X100. However, the model produces a CTOA matching the experimental and for the purposes of this study will suffice. Further calibration work with the high strength X100 material will need to be done to fully understand the inconsistency.

## **6.4 Conclusions**

In this chapter a DWTT model was analyzed under quasi-static loading conditions. A specific focus was placed on examining the Load-LLD data of the models in this chapter. It was shown that using the trapezoidal TSL shape, the CZM can produce experimental Load-LLD data (post-initiation) and simultaneously produce a CTOA matching the value calculated from the S-SSM.

**Table 6.1 - Quasi-Static Cohesive Properties for X70 and X100.**

Material	Cohesive Stiffness (MPa/mm)			Maximum Traction (MPa)			Cohesive Energy (MPa-mm)
	Symbol	$K_{nn}$	$K_{ss}$	$K_{tt}$	$T_n^o$	$T_s^o$	
X70	$2 \times 10^6$	$7.69 \times 10^5$	$7.69 \times 10^5$	1850	1387.5	1387.5	98
X100	$2 \times 10^6$	$7.69 \times 10^5$	$7.69 \times 10^5$	2515	1886	1886	136.8

**Table 6.2 – DWTT Mesh Details.**

Material	Part	Zone	Element Types	Number of Elements	Nominal Size (mm)
X70	DWTT Specimen	Ligament	CPE4R	807	0.3X0.3
		Transition	CPE4R/ CPE3	5723	N/A
		Bulk	CPE4R	1075	3X3
	Crack	Cohesive Layer	COH2D4	799	0.077x0.001
X100	DWTT Specimen	Ligament	CPE4R	504	0.48X0.48
		Transition	CPE4R/ CPE3	3368	N/A
		Bulk	CPE4R	1075	3X3
	Crack	Cohesive Layer	COH2D4	410	0.15X0.01

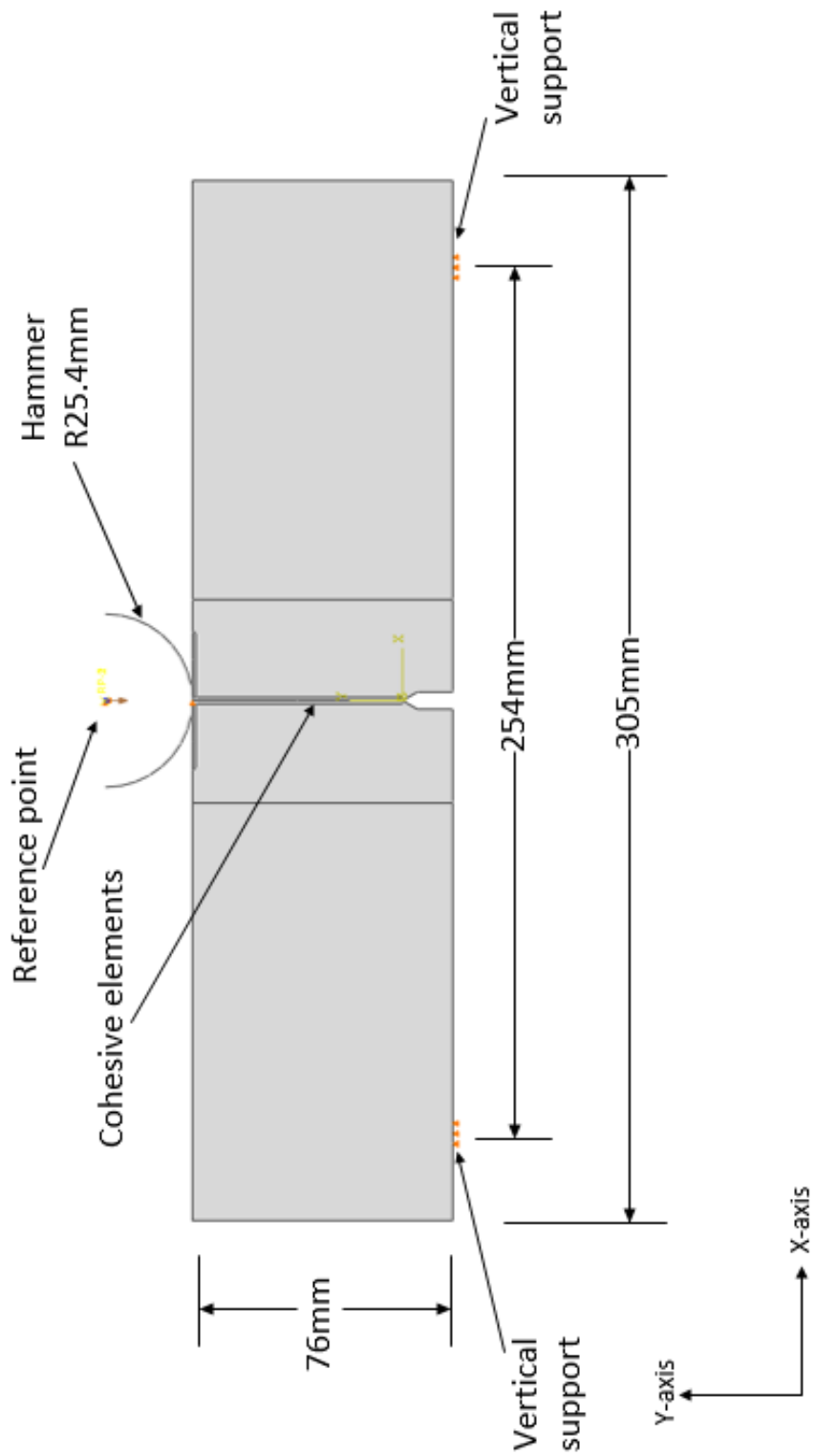
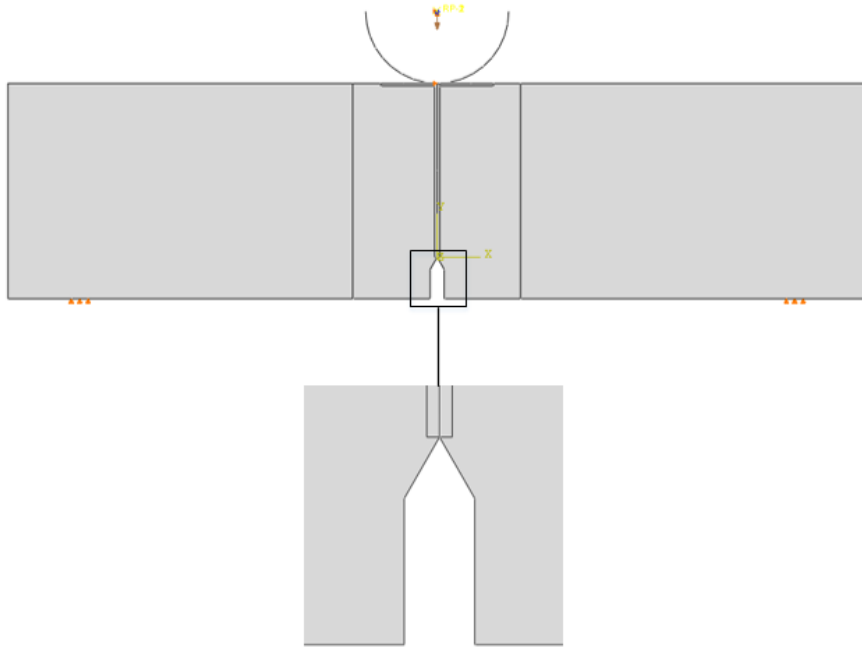
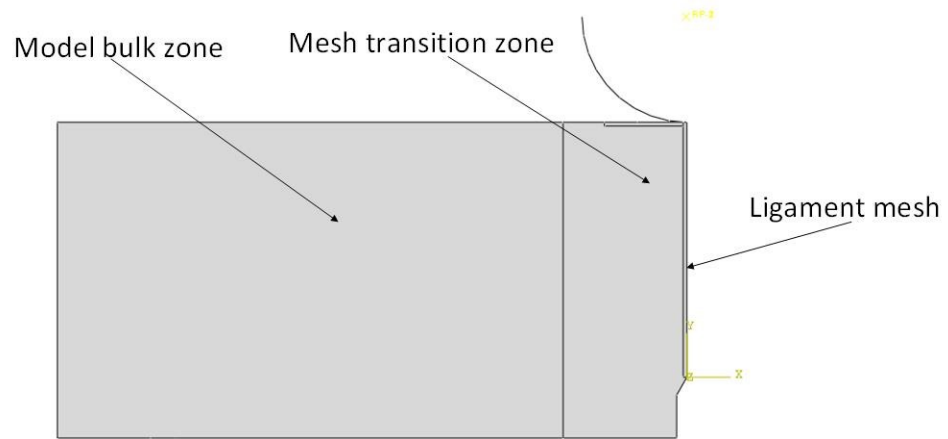


Figure 6.1 - Geometry of DWTT model.



**Figure 6.2 - DWTT model notch tip simplification.**



**Figure 6.3 - Mesh zones (half model).**

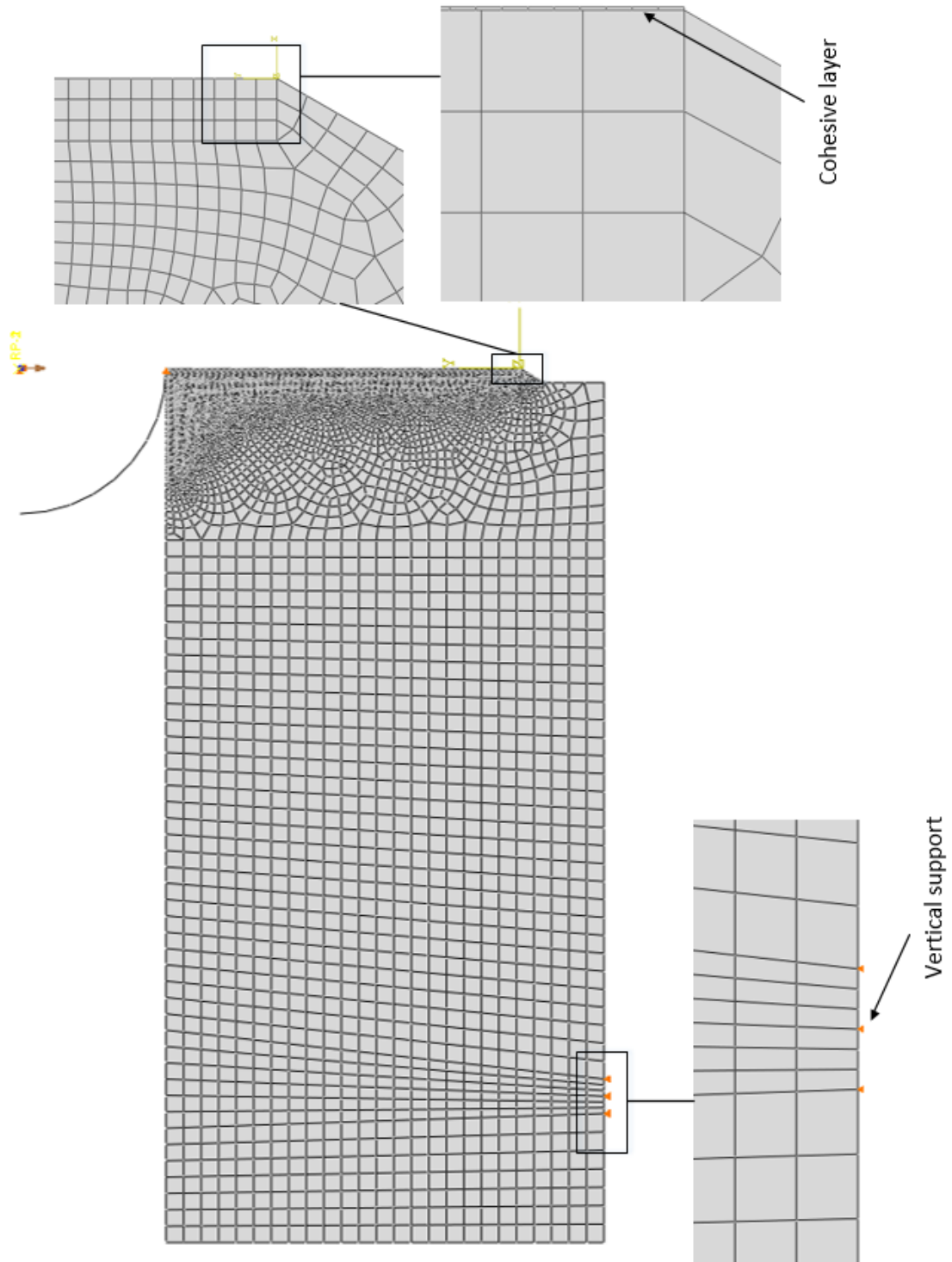


**Figure 6.4 - DWTT model mesh (half model).**

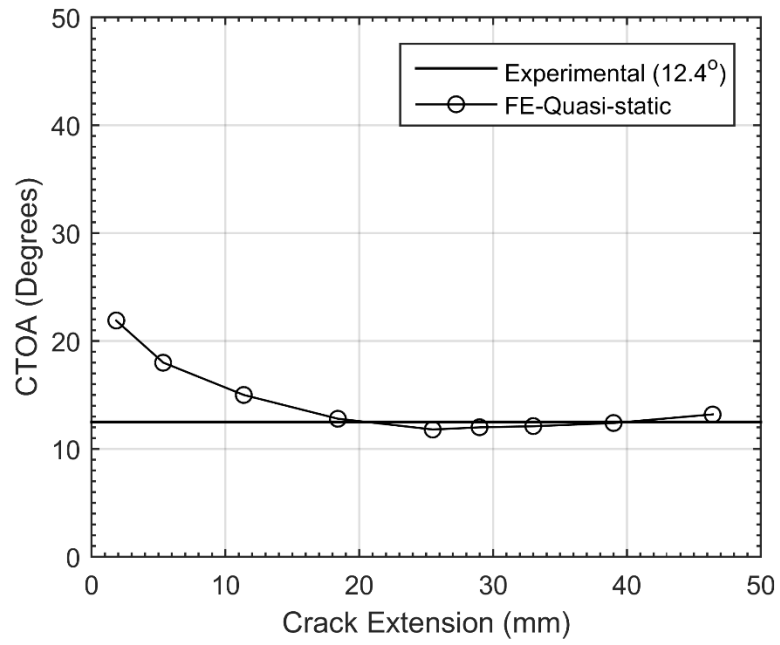


Figure 6.5 – X70 quasi-static model CTOA as a function of crack extension.

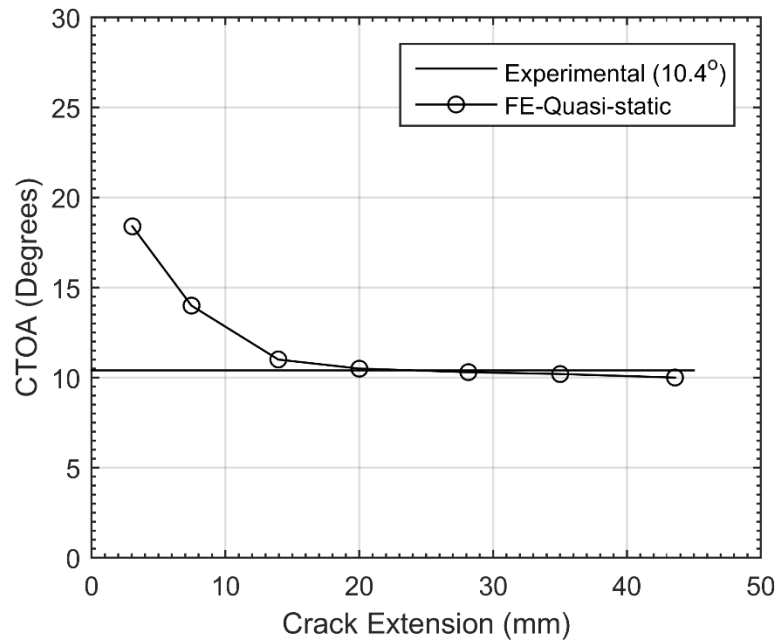
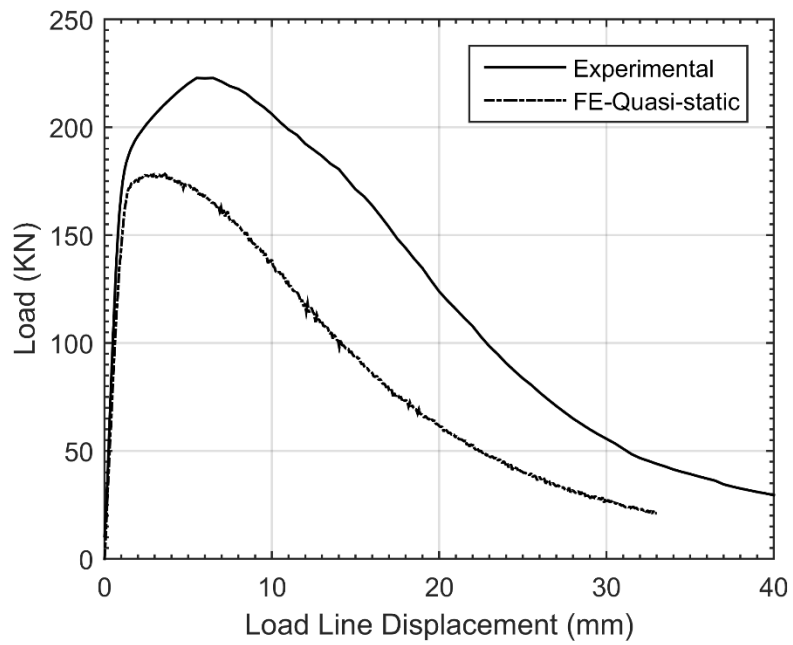
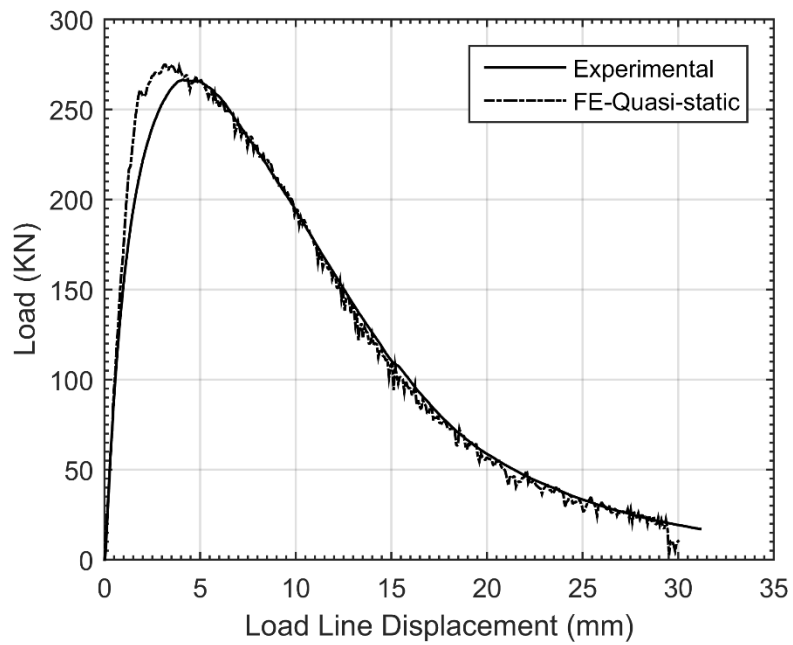


Figure 6.6 - X100 quasi-static CTOA as a function of crack extension.



**Figure 6.7 - X70 FE and experimental quasi-static Load-LLD.**



**Figure 6.8 – X100 FE and experimental quasi-static Load-LLD.**

## **Chapter 7: FE Simulations of a Drop Weight Tear Test Specimen under Impact Loading Conditions**

This chapter presents the finite element simulations of a drop weight tear test specimen under impact loading conditions. The DWTT model was examined at two different loading conditions; a quasi-static loading condition (Chapter 6) and an impact loading condition. Both loading rates were characterized experimentally at CanmetMATERIALS (Xu S. , 2016b). The experimental data was provided for comparison with the FE results and will be discussed later. This chapter presents the computational model including geometry, computational methods, assumptions, loading conditions, and mesh design. The results of the analysis are presented and discussed, and a relationship between the crack velocity and the cohesive energy is assessed based on a rate independent CTOA.

### **7.1 Drop Weight Tear Test (DWTT) Model**

Two-dimensional plane strain simulations of a drop weight tear test specimen were performed using ABAQUS Explicit 6.14-2 (Dassault Systemes, 2014). The purpose of this analysis was to examine the DWTT model with the CZM calibrated in Chapter 3 at an impact loading rate. Furthermore, to assess the use of the CTOA as a loading rate update parameter and examine the use of the trapezoidal TSL shape to simulate ductile fracture. This section outlines the computational model including geometry, computational procedures, material properties, loading conditions and mesh design.

### **7.1.1 Geometry and Computational Procedures**

The geometry and computational procedures of the specimen examined were identical to that presented in Section 6.1.1.

### **7.1.2 Material Properties**

The material properties of X70 and X100 and their implementation in the numerical model were presented and discussed in Section 2.3. The true stress-strain curves can be seen in Figure 2.12. The material elasticity properties used in the numerical analysis are presented in Table 2.3. The true stress-plastic strain data was presented in Table 2.5 and Table 2.6 for X70 and X100, respectively. The rate sensitivity of the material model was introduced as discussed in Section 2.6.3.

### **7.1.3 Cohesive Zone Properties**

The cohesive parameters and their calibration were presented in Chapter 3. The quasi-static cohesive zone properties are presented in Table 6.1 for X70 and X100. The update of the cohesive parameters was implemented as described in Section 3.2.5, based on matching the experimental dynamic CTOA.

### **7.1.4 Loading Conditions**

The boundary conditions of the DWTT model are illustrated in Figure 6.1. The vertical supports were modelled as boundary conditions on the specimen. The impact loading rate was modelled as closely to the experimental set-up as possible. The reference point was assigned a point mass of 1152 kg and an initial velocity of 5.1 m/s to accurately

re-create the initial kinetic energy of the hammer (15 kJ). The velocity of the hammer was prescribed as an initial condition on the reference point. The horizontal displacement of the reference point and rotation about the Z-axis (out of plane axis) was constrained to prevent linear and rotational motion of the hammer. There was no constraint placed on the reference point in the vertical direction to allow the hammer to freely impact the specimen.

### **7.1.5 Finite Element Mesh Design**

The mesh of the DWTT model was identical to the mesh of the quasi-static model, presented in Section 6.1.5. The mesh of the entire model can be seen in Figure 6.4. The specific details of the mesh including element type, number of elements and nominal sizing are presented in Table 6.2.

## **7.2 Analysis Methodology**

The methodology used for this study was the same for both materials. The CZM was calibrated using the method presented in Section 3.2. The models were first analyzed under quasi-static loading conditions in Chapter 6. In this chapter, the model will be examined at an impact loading rate. Bulk material rate hardening was introduced to the material models. The dynamic models were first analyzed using the quasi-static TSL. The quasi-static TSL was then updated as specified in Section 3.2.5. A focus was placed on comparing the updated model data to the dynamic experimental data. As well comparisons are made between the model with an updated TSL and the one without a TSL update.

Following the comparison with experimental data, the effect of loading rate on the TSL was assessed. This was achieved through simulating the dynamic DWTT model

higher hammer impact velocities to induce higher fracture velocities. The TSL was then iteratively updated to match the experimental dynamic CTOA of the material.

### **7.3 Results and Discussion – Impact Loading Rate**

The impact loading rate was first assessed with a rate sensitive material model and the quasi-static TSL. It was found that there was a drastic drop in CTOA, a large, unrealistic increase in crack velocity, and a large drop in the post-initiation slope of the Load-LLD data. The TSL of the models were then iteratively adjusted so as to match the experimental dynamic CTOA. The following sections present and discuss the effect on the CTOA, crack growth rate, and the Load-LLD data.

#### **7.3.1 CTOA**

##### *X70 Results*

The CTOA as a function of crack extension can be seen in Figure 7.1. Under the dynamic loading rate, including rate hardening in the bulk material and the quasi-static TSL, the CTOA was drastically reduced to an average steady-state value of 3°. The experimental value of the dynamic CTOA is 12.5°. This drop in CTOA is due to the increase in yield stress at the crack tip reducing the strain of the flanks and ultimately reducing the CTOA. An update to the TSL was introduced based on trial and error of matching the dynamic CTOA of the model to the experimental value. The average SS-CTOA of the model with the updated TSL was 12.6°. The update to the TSL required to match the CTOA can be seen in Figure 7.2. The updated TSL parameters are  $\Gamma_0=149.9$  MPa-mm and  $T_n^0=2275$  MPa. The impact TSL was scaled from the quasi-static TSL maintaining the same shape,

but increasing the maximum traction and the cohesive energy. One notable observation of the updated CTOA as a function of crack extension is the delay in steady-state crack extension region, as defined on the approximate stabilization of the CTOA. The CTOA stabilized around 18 mm of crack extension, while in the updated TSL impact model the CTOA stabilized around 23 mm of crack propagation. This was observed for the X100 material as well.

### *X100 Results*

The CTOA as a function of crack extension can be seen in Figure 7.3. The Under the dynamic loading with rate hardening in the bulk material and no alteration to the TSL, the CTOA was reduced to an average steady-state value of 4°. The experimental value of the dynamic CTOA is 9.7°. This again is due to the increase in yield stress at the crack tip reducing the strain of the flanks and ultimately reducing the CTOA. The update to the TSL was introduced based on trial and error of matching the dynamic CTOA to the experimental value. The average SS-CTOA of the model with the updated TSL was 10.1°. The update to the TSL required to match the CTOA can be seen in Figure 7.4. The updated TSL parameters are  $\Gamma_0=169.5$  MPa-mm and  $T_n^0=2800$  MPa.

### **7.3.2 Crack Growth Rate**

The crack growth rate was determined by examining the failure of the cohesive elements during the simulation. The failure of the elements and the simulation time were extracted and correlated to determine the crack length as a function of time. The steady-state crack velocity of the model was determined by fitting a linear trend line to the steady-

state portion of the crack extension time curve for the model. The steady-state portion was determined to be when the CTOA was approximately constant. An example of the calculation of the crack velocity is shown in Figure 7.5. The steady-state region of the X70 model begins after 20 mm of propagation. A least squares polynomial method was employed to fit the linear equation to the data set ranging from 20 mm-30 mm of crack extension over a time period of approximately 1.2 ms for the given example. The range was chosen based on the correlation coefficient associated with the linear regression, optimizing so it approached a value of 1. This technique was used for all calculations of the crack velocity in the remainder of this work.

Simulations for both materials presented the same general shape with a transient portion leading into a linear region (indicating steady-state crack propagation) and lastly a transient portion indicating the crack is slowing. The steady-state velocities for each material, with the updated TSL are discussed below.

### *X70 Results*

The crack extension as a function of time for the X70 model, with the updated TSL, can be seen in Figure 7.5. The impact loading rate model with an updated TSL presented a steady-state crack velocity of 8.3 m/s. This steady-state crack velocity is comparable to a crack velocity of 8.46 m/s calculated from a damage mechanics model of the same material at the same loading rate (Simha, Xu, & Tyson, 2014). This indicates that though the Load-LLD curve does not completely match the experimental data, calibrating the TSL so as to reproduce the experimental CTOA can still produce a realistic crack velocity.

### *X100 Results*

The crack extension as a function of time data for the X100 model can be seen in Figure 7.6. The impact loading rate model with an updated TSL presented a steady-state crack velocity of 13.7 m/s. There are no other models of the X100 material or experimental data of the crack velocity for comparison; however, the crack velocity is in the expected range of 8-30 m/s.

### **7.3.3 Load-Load Line Displacement (Load-LLD)**

#### *X70 Results*

Simulations of the DWTT model at the impact loading rate, with the inclusion of material rate hardening and the quasi-static TSL, showed a significant increase in negative slope post crack initiation as shown in Figure 7.7. This is due to the effect of including material rate hardening in the bulk material, which causes an increase in yield stress near the crack tip. This increase in yield stress introduces significant complications as the Load-LLD curve shows a sharp descent during crack propagation and a large decrease in CTOA. This indicates that the increase in yield stress due to the rate effect requires a modification to the TSL to reproduce the experimental CTOA and load-LLD curve from experiments. Figure 7.7 shows the load-LLD curve with an updated TSL to match the experimental CTOA of the drop weight loading rate. The alterations to the TSL shows improved agreement with the experimental load-LLD curve, these results further verify those of Chapter 6 that the CTOA is a calibration parameter.

### *X100 Results*

The Load-LLD data for the X100 model is plotted in Figure 7.8. Similar to the X70 results, when the model was simulated under the impact loading rate, with the inclusion of material rate hardening and no alteration to the TSL, a significant increase in negative post-initiation slope was observed. The model including rate hardening and an update to the TSL produces a post-propagation slope extremely close to the experimental data. Again, the initial noise and large overshoot of the updated model is due to the assumption of the TSL shape and the selection of the parameters, which will require further investigation.

#### **7.4 Crack Velocity – Cohesive Energy Relationship**

It is evident that when accounting for the effects of rate hardening there is a requirement to adjust the TSL based on the level of yield stress at the crack tip. However, with the knowledge of experimental parameters, such as the CTOA, at higher crack velocities ( $>100\text{m/s}$ ) being minimal this makes the advancement of this model quite limited. For this reason, to extend this work and assess the effect of crack velocity on the TSL, it was assumed that the CTOA remains constant with increasing crack velocity.

In this section a relationship between the crack velocity and cohesive energy, which adjusts the steady-state cohesive energy of the model to produce a constant CTOA, will be presented. The purpose of this analysis was to examine the change in cohesive energy required at higher velocities to maintain a constant CTOA. The material models included rate hardening. To achieve this the DWTT model was simulated with artificially elevated hammer impact velocities to induce higher crack velocities and the TSL was iteratively

adjusted until the SS-CTOA matched the experimental values within a range of  $\pm 1^\circ$ . For the purposes of this study the cohesive energy relationship is only represented in terms of the crack velocity. A more useful form would be in terms of separation rate of the cohesive element; however, this is a likely avenue for further research and will not be presented here.

The most useful form of this relation would be through relating the cohesive energy and the separation rate of the cohesive elements. This would allow for the implementation of a rate hardening parameter in the CZM. However, relating the steady-state crack velocity to the cohesive energy allows for the examination of the trend of the cohesive energy for increasing loading rate.

#### **7.4.1 X70**

The hammer velocity was adjusted from the impact loading rate (5.1 m/s) to 10 m/s and then from 10 m/s to 50 m/s on 10 m/s increments. 50 m/s was chosen as the final loading rate as it was found that the higher velocities would cause large plastic strains along the ligament and prematurely affect the CTOA.

The crack extension as a function of time curves for the adjusted impact velocities can be seen in Figure 7.9 and Figure 7.10. The CTOA as a function of crack extension can be seen in Figure 7.11 and Figure 7.12 for each hammer velocity. The hammer velocity, crack velocity, cohesive energy, and average SS-CTOA are tabulated in Table 7.2. The crack velocity and the cohesive energy necessary to produce a CTOA of  $12.5^\circ \pm 1^\circ$  are plotted in Figure 7.13. The general trend indicates that the cohesive energy increases with increasing crack velocity. The cohesive energy appears to increase to a horizontal

asymptote. Simply put, this allows for a power law equation to be fit to the cohesive energy and the steady-state crack velocity. The resultant equation is the one presented as  $f(CV)$  in Eq. 3.9. The equation was fit to the data using a least squares polynomial technique and is presented below.

$$\Gamma_{Dynamic, X70} = 143.64(CV)^{0.0236} \quad \text{Eq. 7.1}$$

where  $\Gamma_{Dynamic, X70}$  is the dynamic cohesive energy and  $CV$  is the steady-state crack velocity. It is important to note the equation is only valid for  $CV > 20$  m/s, as with the limited data set, below 20m/s the equation does not capture the data. The trend will be discussed at the end of the X100 results.

#### 7.4.2 X100

The hammer velocity was adjusted from the impact loading rate (5.1 m/s) to 10 m/s, and from 10 m/s to 40 m/s on 10m/s increments. An impact velocity of 40 m/s was the final as it was found that the higher velocities would cause large plastic strains along the ligament and affect the CTOA. The crack extension time curves for the adjusted impact velocities can be seen in Figure 7.14 and Figure 7.15. The CTOA as a function of crack extension can be seen in Figure 7.16 for each hammer velocity. The crack velocity and the cohesive energy necessary to produce a CTOA of  $9.7^\circ \pm 1^\circ$  are shown in Figure 7.17. The hammer velocity, crack velocity, cohesive energy, and average SS-CTOA are tabulated in Table 7.2. A similar trend to the X70 material was observed, namely, that the plot of cohesive energy as a function of steady-state crack velocity approached a horizontal asymptote with increasing crack velocity. This allows for a power law equation to be fit

to the cohesive energy and the steady-state crack velocity. The resultant equation is the one presented as  $f(CV)$  in Eq. 3.9. The power law, presented below, was fit to the data using a least squares polynomial technique

$$\Gamma_{dynamic, x100} = 169.1(CV)^{0.02} \quad \text{Eq. 7.2}$$

It is important to note the equation is only valid for  $CV > 20$  m/s. Both materials presented the same trend, namely, a non-linear increase in cohesive energy below crack velocities of 30m/s, with the trend becoming more linear as the crack velocity increased. This analysis presents insight into a TSL update algorithm, namely, that it is likely a power law relation or some variant will be required to relate the TSL parameters to the loading rate. As well it is also demonstrated that the inclusion of bulk material hardening requires an update to the cohesive energy with a similar trend as the change of the material yield stress with respect to rate. The observed trend bares a similar resemblance to the dynamic yield stress at increased strain rates. This was briefly examined in this work; however, no relation was observed for the assumed TSL shape and parameters. A parametric study examining the maximum traction, cohesive energy, TSL shape and strain rate must be conducted to further investigate this trend. This is further discussed in Section 9.3 for future recommendations. Further work on this relation will be required along with experimental validation for the crack velocity relation of the CTOA.

## 7.5 Conclusions

The effect of loading rate and crack velocity on the CTOA was examined using a DWTT specimen. This was achieved through examining a DWTT specimen at an impact loading rate. To validate the model a comparison with experimental data from DWT testing was carried out to determine the ability of the model to capture the fracture process.

The inclusion of bulk material hardening in dynamically loaded models has presented a significant challenge with the cohesive zone model. It was found that the CZM calibrated for quasi-static loading conditions cannot be used for analyses on the impact loading rate without an alteration to the TSL. This observation was present for both X70 and X100. The TSL was updated based on matching the dynamic CTOA of the model to that of experimentation. The updated TSL model produced better agreement with the experimental load-LLD data and crack velocity. The results further confirm the major conclusion of Chapter 6, that the CTOA can be used as a calibration parameter of the CZM.

To extend this work and examine the effect of loading rate on the TSL, a relationship between the crack velocity and the cohesive energy was developed assuming that the CTOA remains constant with increasing crack velocity. This relationship is purely theoretical and still requires validation via experimental comparison.

In conclusion, this chapter highlighted a significant challenge with the use of the CZM to model ductile fracture at higher loading rates. However, it was also demonstrated that the effect of rate hardening can be overcome with the implementation of a rate hardening relation based on matching the experimental CTOA.

**Table 7.1 - TSL parameters updated for impact loading rate (matching experimental CTOA).**

Material	Cohesive Stiffness (MPa/mm)			Maximum Traction (MPa)			Cohesive Energy (MPa-mm)
	Symbol	$K_{nn}$	$K_{ss}$	$K_{tt}$	$T_n^o$	$T_s^o$	
X70		$2 \times 10^6$	$7.69 \times 10^5$	$7.69 \times 10^5$	2275	1706	1706
X100		$2 \times 10^6$	$7.69 \times 10^5$	$7.69 \times 10^5$	2800	2100	2100

**Table 7.2 - Steady-state crack velocities.**

Material	Hammer velocity (m/s)	Steady-state crack velocity (m/s)	Updated Cohesive Energy (MPa-mm)	Average steady-state CTOA (Degrees)
X70	5.1	8.3	149.9	12.6
	10	17.2	152	13
	20	34.9	156	13.3
	30	57.6	158	12.9
	40	84.7	161	12.6
	50	96.7	162	13.0
X100	5.1	13.7	169.5	10.1
	10	24.2	181	9.8
	20	57.1	185	10.3
	30	84.2	188	10.2
	40	124	189	10

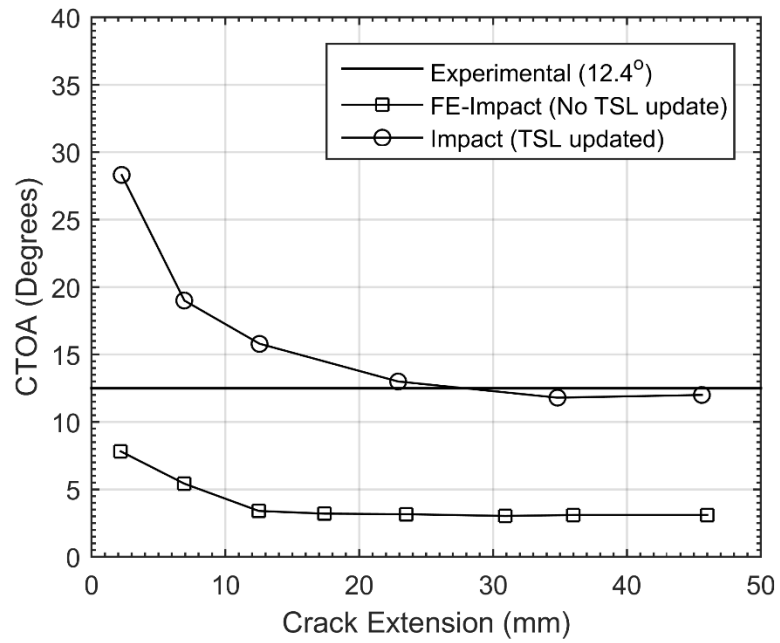


Figure 7.1 - X70 impact model CTOA as a function of crack extension.

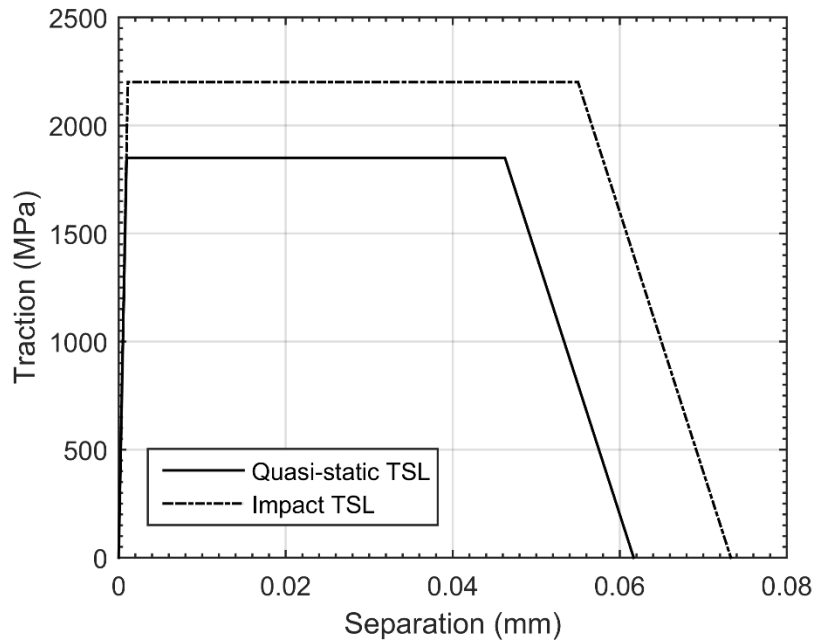


Figure 7.2 - X70 quasi-static and updated impact TSL.

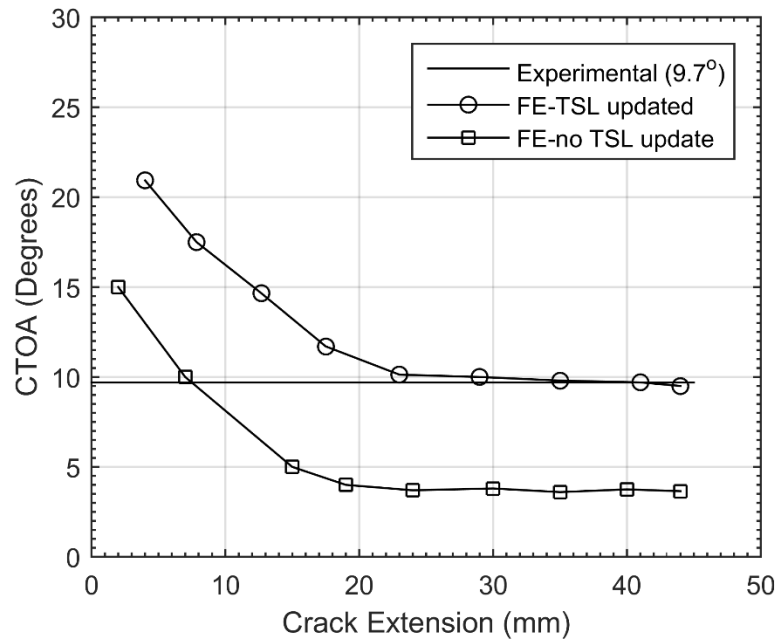


Figure 7.3 - X100 impact model CTOA as a function of crack extension.

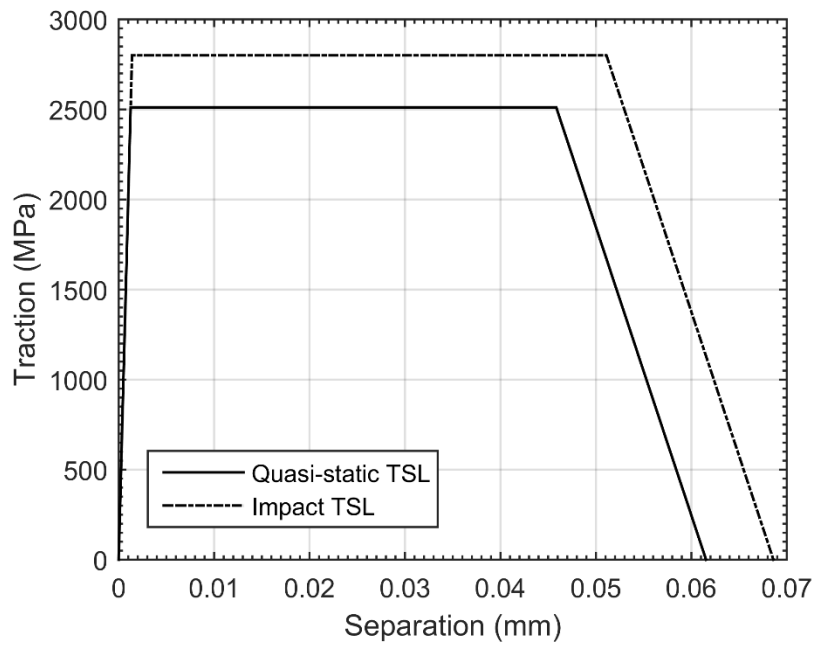


Figure 7.4 - X100 quasi-static and updated impact TSL.

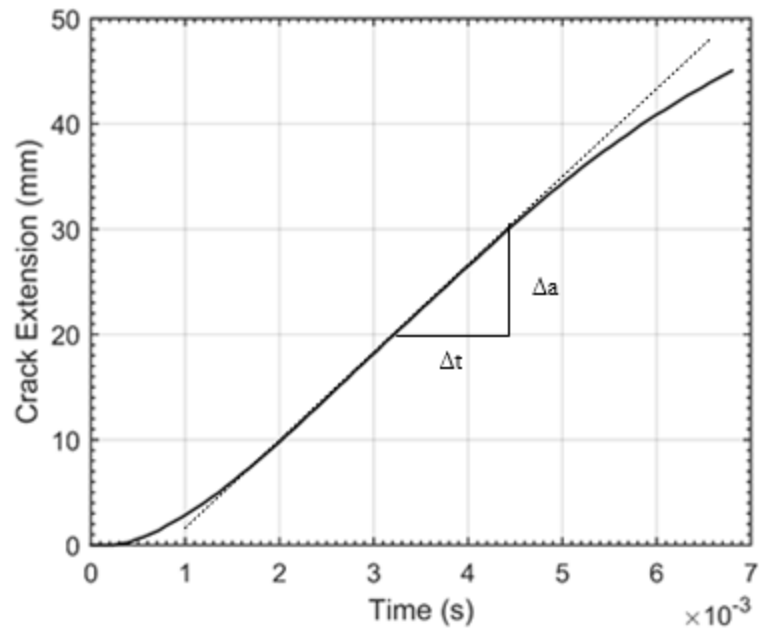


Figure 7.5 - X70 crack extension as a function of time. (FE updated TSL)

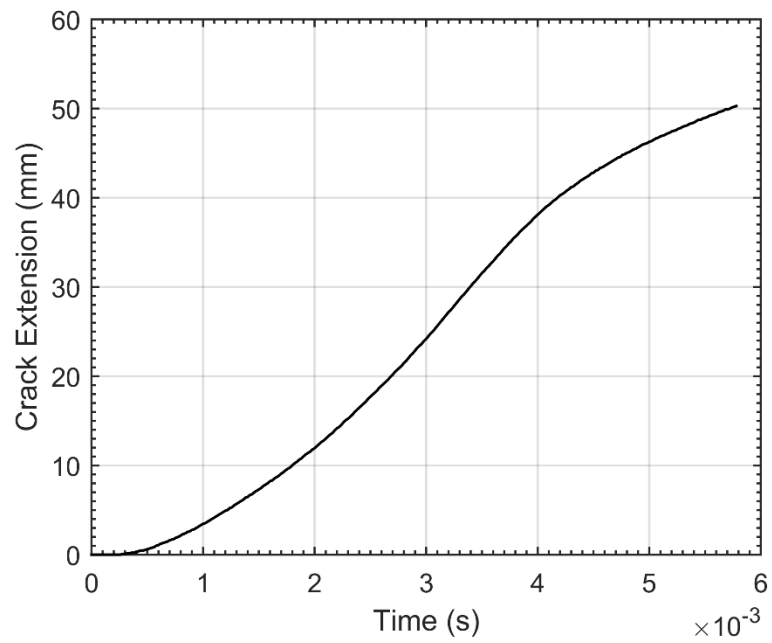


Figure 7.6 – X100 crack extension as a function of time. (FE updated TSL)

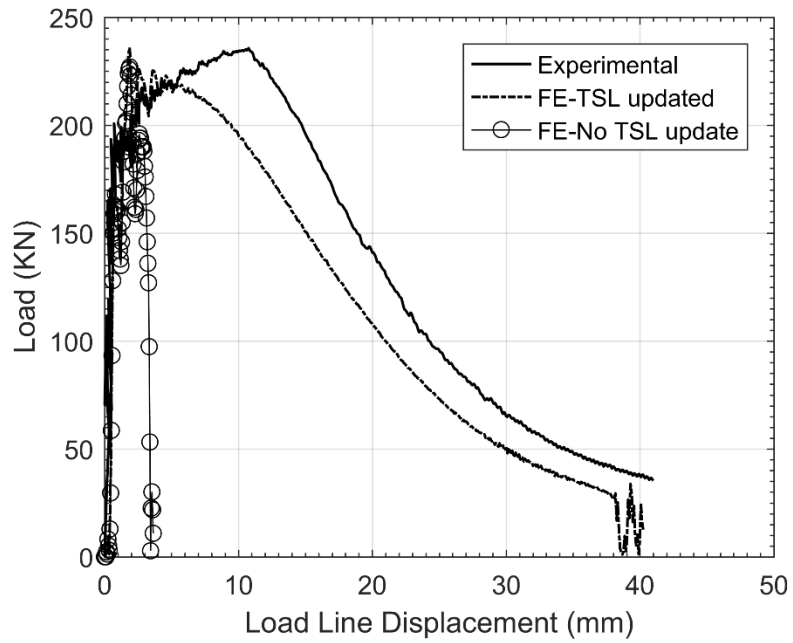


Figure 7.7 - X70 FE and experimental impact Load-LLD (FE updated and non-updated TSL)

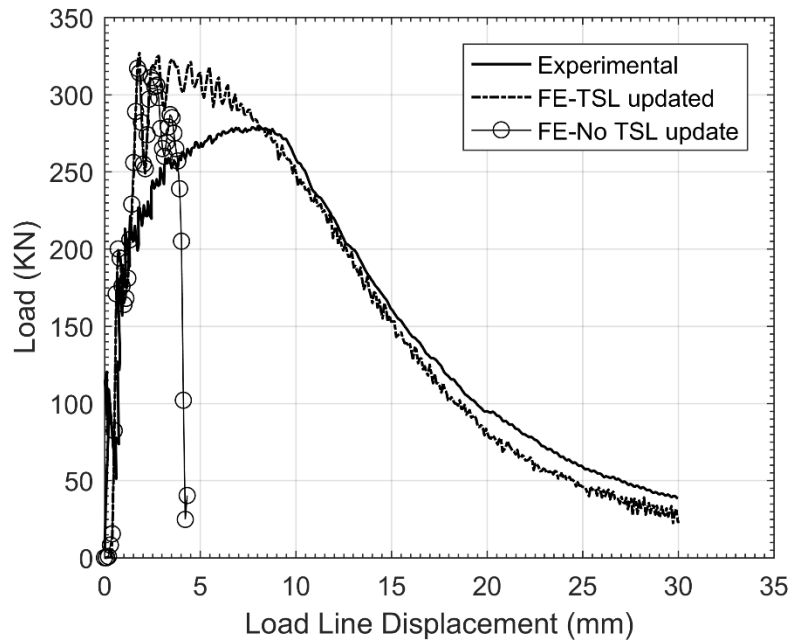


Figure 7.8 – X100 FE and experimental impact Load-LLD (FE updated and non-updated TSL)

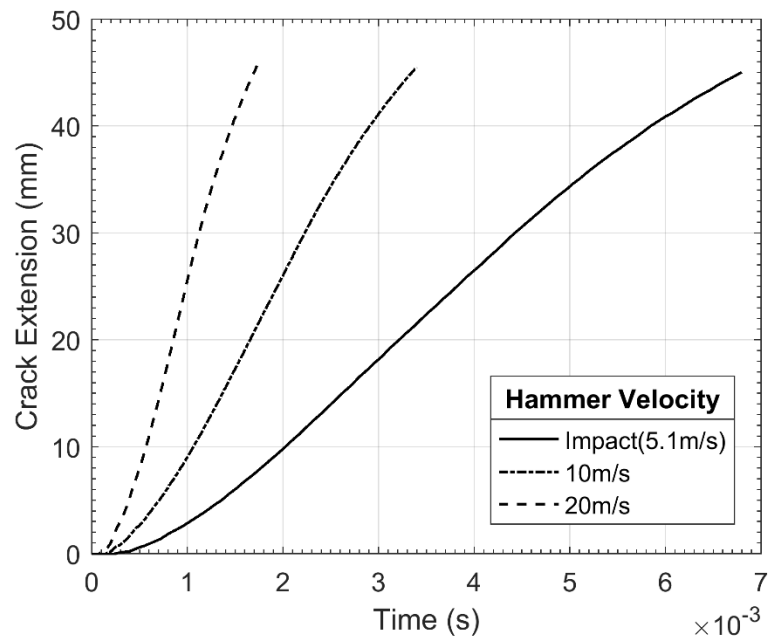


Figure 7.9 - X70 crack extension as a function of time.

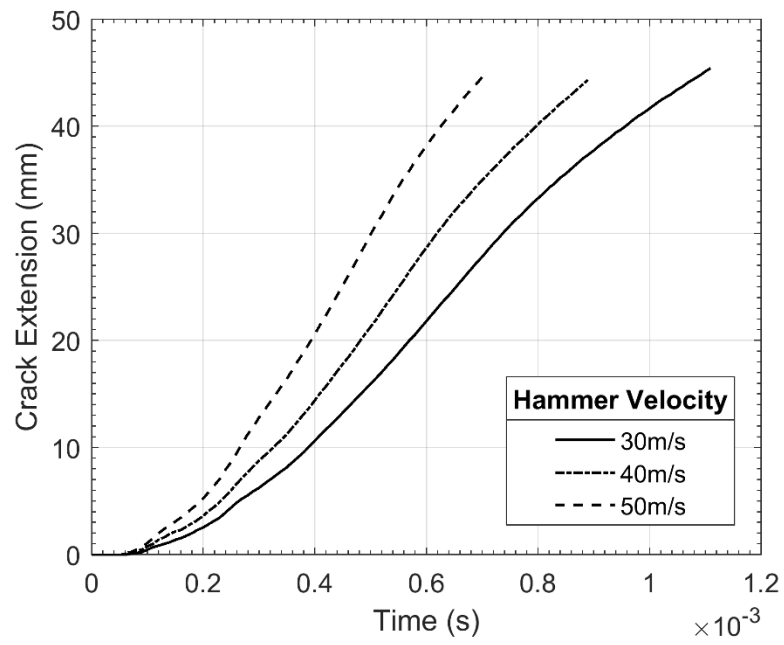


Figure 7.10 - X70 crack extension as a function of time (continued).

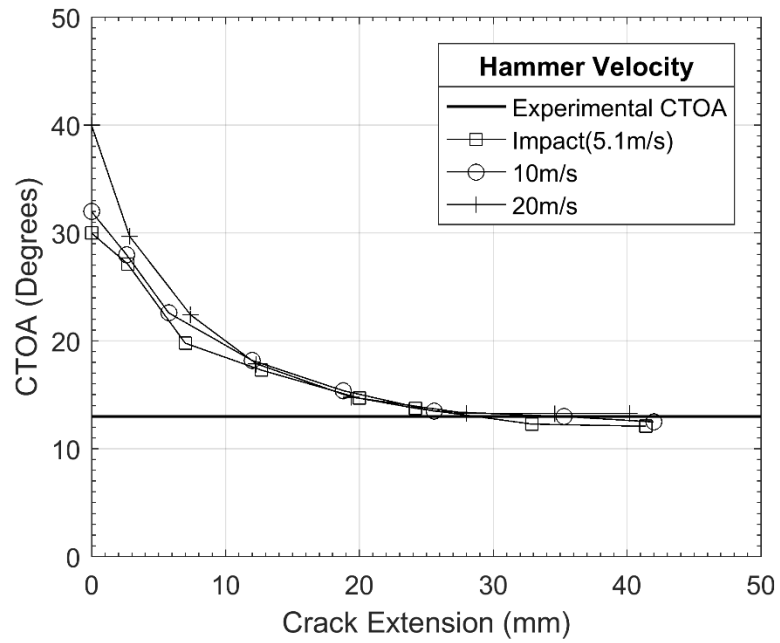


Figure 7.11 - X70 CTOA as a function of crack extension.

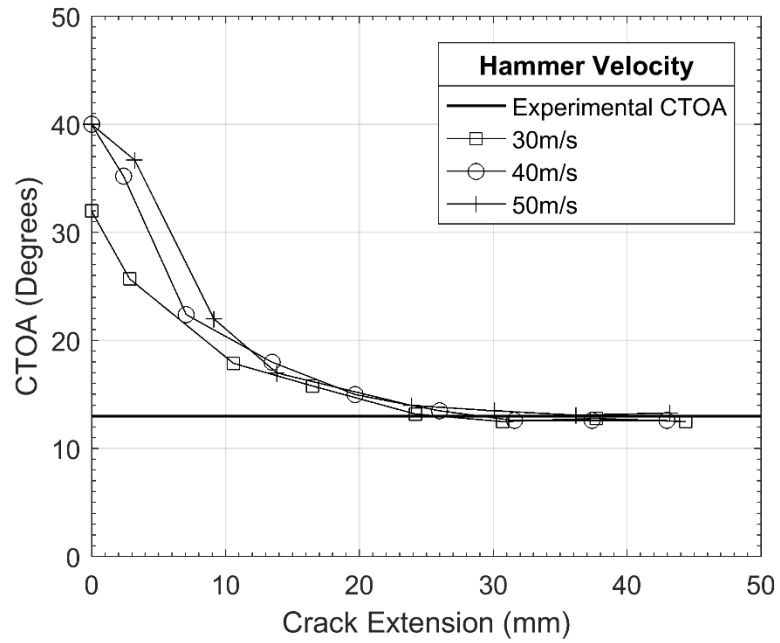


Figure 7.12 - X70 CTOA as a function of crack extension (continued).

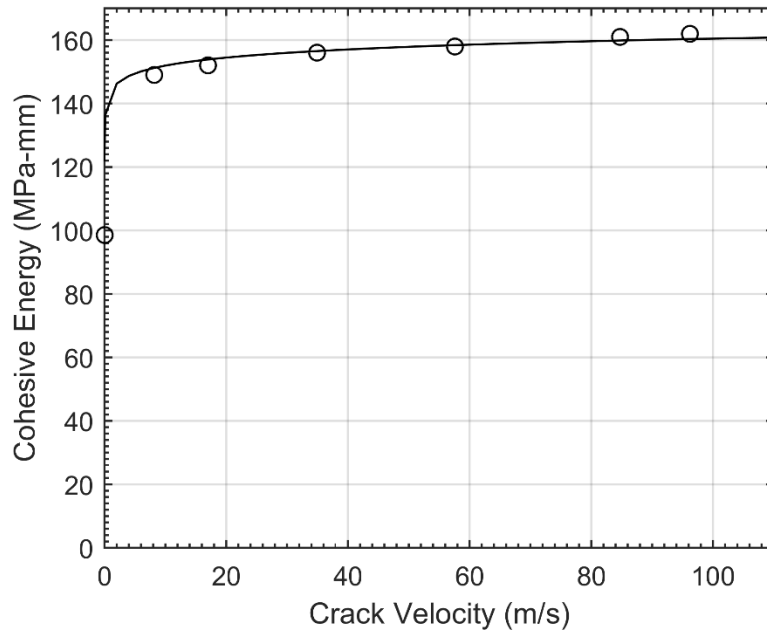


Figure 7.13 - X70 cohesive energy as a function of crack velocity.

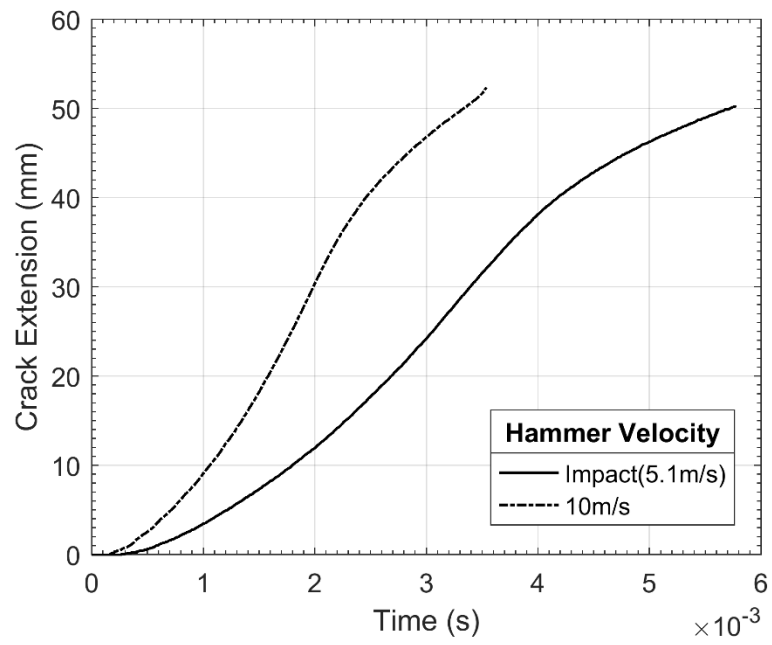


Figure 7.14 – X100 crack extension as a function of time.

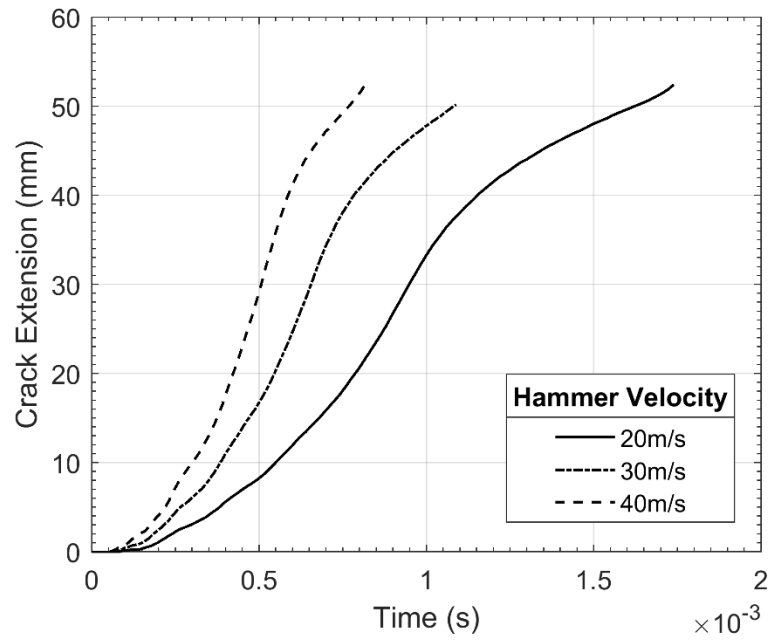


Figure 7.15 – X100 crack extension as a function of time (continued).

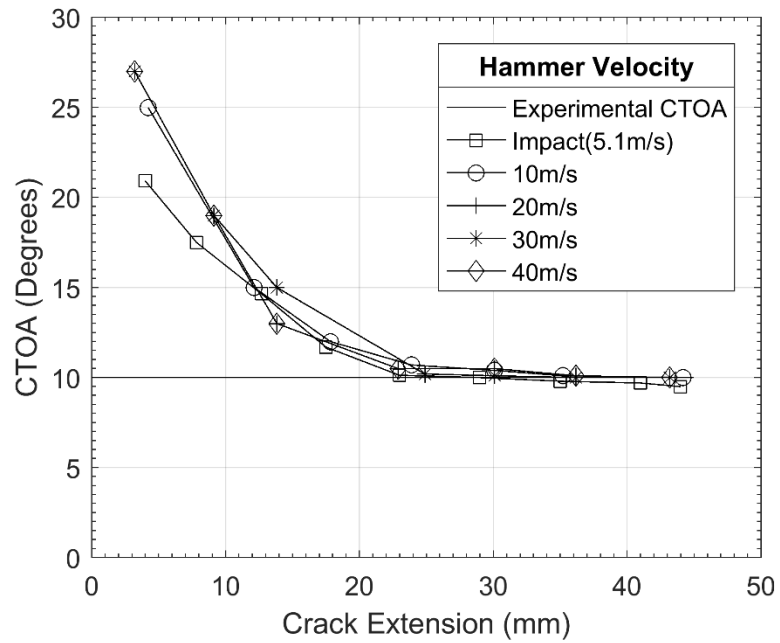
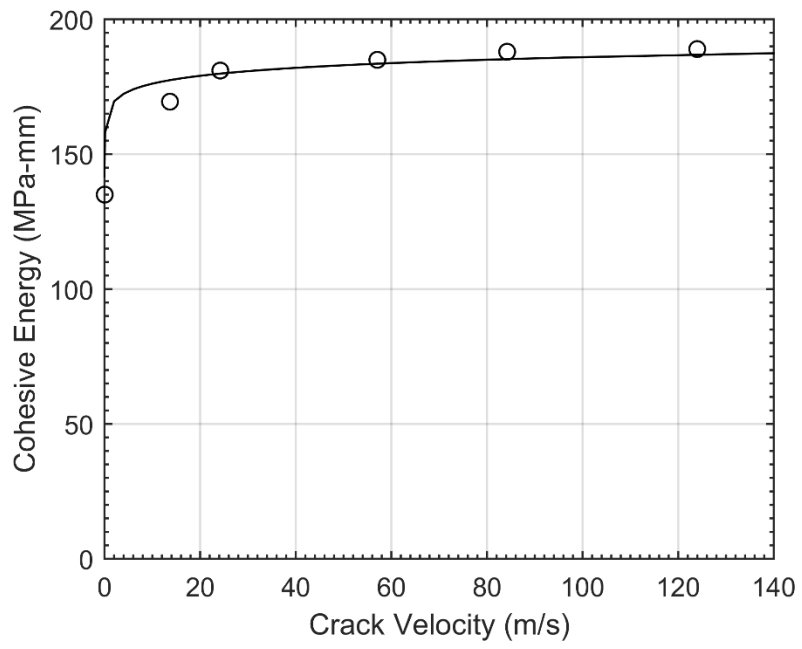


Figure 7.16 – X100 CTOA as a function of crack extension.



**Figure 7.17 – X100 cohesive energy as a function of crack velocity.**

## **Chapter 8: FE Simulations of a Plate Model under Dynamic Loading Conditions**

This chapter presents finite element simulations of a tensile plate model that simplifies the fracture process geometry in a pipe to a planar state. The intended use of this model was to provide insight on the effect of crack velocity on the CTOA at higher crack velocities ( $>100$  m/s). This was achieved in two parts; first by examining the model with the quasi-static calibrated TSL parameters and no material rate hardening, and secondly, by examining the model with the inclusion of rate hardening and updating the TSL to produce a constant CTOA (similar to Section 7.4). Furthermore, this model was used to analyze the effect of inertia on the material resistance data (crack velocity driving force relationship) and CTOA.

### **8.1 Tensile Plate Model**

The plate model was generated as a two-dimensional plane strain model and analyzed using the commercial finite element code ABAQUS 6.14-2 (Dassault Systemes, 2014). This section presents the computational model including the geometry, loading conditions, material properties, cohesive properties and mesh design.

#### **8.1.1 Geometry and Computational Procedures**

The model examined in this chapter is a simplification of a pipe to a plate subjected to a tensile stress load. A pipe loaded with an internal pressure experiences a tensile hoop stress. The 3-D shape of the pipe and the manner in which it separates during fracture propagation complicates many aspects of the model. Firstly, the effect of the flap opening

and the pressure distribution behind the crack tip is not completely known. Moreover, measuring the CTOA becomes much more complicated to accurately and repeatedly extract from a pipe model with the curvature of the unfolding flap. As the intention of this work is to examine the CTOA specifically the ability to confidently extract the CTOA was a priority. The plate model removes the complexity of accounting for the curvature of the flaps during propagation, as well as simplifies the model from three dimensions to two dimensions.

It was assumed that a large part of the inertial resistance would be present from the upper half of the pipe and the backfill which covered it. This assumption attributes the inertial effect to the material above the midsection of the pipe. The concept behind this assumption is illustrated in Figure 8.1.

The model is illustrated in Figure 8.2. The dimensions of the plate model were chosen based on the size of the pipe in which the material would operate in practice. The work of (Xu & Tyson, 2015) records the service size of several standard pipes. It was recorded that X70 was used in a pipe with an outer diameter of 914.4 mm and X100 was used in a pipe with an outer diameter of 1219.2 mm. The height of a single flank ( $H$ ) was chosen to be 718 mm for the X70 model and 957 mm for the X100 model. This was chosen based on the circumference of the pipe to keep the total mass of the model in the realm of the pipe. As shown in Figure 8.1, it was assumed that the total model height ( $2H$ ) was derived from half of the circumference of the pipe.

The total length ( $L$ ) of the models analyzed was 5000 mm with an initial notch depth ( $a_0$ ) of 1500 mm. As a result the length of the ligament was 3500 mm. This was chosen as it is common to allow for a minimum of one diameter length of propagation in a

pipe for the crack to reach steady-state. This assumption was verified and shown to be highly conservative when examining the crack extension as a function of time from the FE results. The dimensions of the two models are summarized in Table 8.1.

The cohesive elements were inserted along the ligament between the two flanks. The cohesive layer was constrained to the two flanks using a surface-to-surface tie constraint. This constrained the nodes of the cohesive layer to the surface of the flank.

### **8.1.2 Material Properties**

The material properties of X70 and X100 and their implementation in the numerical model were presented and discussed in Section 2.3. The true stress-strain curves can be seen in Figure 2.12. The elastic material properties used in the numerical analysis are presented in Table 2.3, the stress-plastic strain data was presented in Table 2.5 and Table 2.6 for X70 and X100, respectively. The rate hardening dependence was implemented using the data in Table 2.4.

### **8.1.3 Cohesive Zone Properties**

The cohesive parameters and their calibration were described in Chapter 3. The quasi-static cohesive zone properties are presented in Table 3.3. The cohesive properties were updated in a similar manner as Chapter 7, namely, the shape was maintained and the maximum traction and cohesive energy were increased.

#### **8.1.4 Loading Conditions**

The load was applied in a two-step analysis. In the first step there was a vertical constraint placed along the crack path, to prevent the crack from prematurely initiating. It should be noted that the vertical constraint is placed on the bulk material and not the cohesive elements. A horizontal constraint was placed on the right edge to prevent linear motion. The stress field, assigned to the outer edges, was ramped from 0 to the applied stress value for the analysis. The boundary conditions for the first step can be seen in Figure 8.3. The purpose of the first step was to induce a constant stress field in the model, while constraining the crack.

At the beginning of the second step, a horizontal constraint was added to the left side of model to simulate a symmetry condition. The constraint along the crack path was removed. The removal of the vertical constraint along the crack path allowed for the crack to propagate in a model with constant stress. Throughout the second step the stress field was kept constant along the outer edge of the model.

It is known that the constant stress field is an unrealistic assumption and not an accurate reflection of the physical process. It is understood that as the crack propagates the stress along the flank behind the crack tip should be reduced and eventually reach zero once the crack has propagated a significant portion past the location. However, as this model is merely used on a qualitative basis and not to generate specific data, this assumption will suffice for the purposes of this work.

### **8.1.5 Mesh Design**

The mesh was designed similar to the DWTT model. The model was divided into three zones; the ligament zone, the transition zone and the bulk zone. These zones are outlined in Figure 8.5. The ligament was assigned structured four node plane strain quadrilateral elements. The transition zone utilized a combination of four node quadrilateral elements and three node triangular elements, both of which were plane strain. This was done to facilitate a rapid mesh transition from the ligament to the remainder of the model. The ligament zone was assigned structured four node quadrilateral elements. The mesh used for the model can be seen in Figure 8.6. The mesh of the cohesive layer was assigned four node cohesive elements with a structured pattern. The specific details of the mesh including element types, number of elements and nominal sizing can be seen in Table 8.2.

## **8.2 Analysis Methodology**

The plate model was utilized for two separate analyses. The first was to continue examining the effect of loading rate on the CTOA at crack velocities  $>100$  m/s. This analysis was completed for both X70 and X100. The models were examined in two parts; the first part involved analyzing the models with the quasi-static TSL and neglecting material rate hardening. A specific focus was placed on assessing the effect on the SS-CTOA. The second part included material rate hardening and updating the TSL to produce a constant CTOA. In this analysis, a specific focus was placed on the resultant effect on the CVDFR.

The second analysis examines the effect of inertia on the crack velocity-driving force relation (CVDFR) and the steady-state CTOA. As discussed in Chapter 2, the CVDFR for this model is analogous to the material resistance curve for the TCM, though it is for a different geometry. In the inertia analysis only the X70 material was used. The analysis was assessed through comparing the CVDFR and the SS-CTOA of the models with three different densities. The densities assessed were unscaled ( $7850 \text{ kg/m}^3$ ), 150% of the unscaled density ( $11775 \text{ kg/m}^3$ ), and 200% of the unscaled density ( $15700 \text{ kg/m}^3$ ).

The CVDFR curves were determined from the models by plotting the applied stress as a function of the induced steady-state crack velocity.

### **8.3 Results and Discussion – Effect of Crack Velocity on the CTOA**

#### **8.3.1 Excluding Material Rate Hardening**

The use of the CZM to model crack propagation in pipes has been used on small diameter pipes in the work of (Shim, Wilkowski, Rudland, Rothwell, & Merritt, 2008). More recently, the CZM was used to simulate mechanical crack arrestors in larger pipes (diameter of 762 mm) in the work of (Uddin & Wilkowski, 2016). In the mentioned efforts, the effects of bulk material rate hardening are neglected for purposes of the analyses. As shown in Chapter 7 of this work, when accounting for the rate hardening of the bulk material, the TSL must be updated based on matching an experimental parameter when examining a dynamic model. This section addresses the effect on the CTOA and the steady-state crack velocity when using the CZM (neglecting rate hardening and using a quasi-static TSL) to model crack propagation at higher loading rates.

The effect of crack velocity on the CTOA was studied using the plate model assuming that the material behavior is independent of rate and is only modeled by the quasi-static stress-strain relationship. This was achieved by using the model to induce higher crack velocities, using the quasi-static calibrated CZM from Section 3.2.

### *X70 Results*

The crack extension as a function of time for the X70 material can be seen in Figure 8.7 and the steady-state crack velocities are listed in Table 8.3. Similar to the previous section, the steady-state portion of the crack extension – time curve was determined to be when the CTOA reached an approximately constant value. As expected with increasing applied stress, the velocity of the crack is increased. An important observation is that the crack velocities are unrealistically high for any practical comparison to experimental data. This is largely due to the simplifying assumptions of the pipe to a flat plate. The largest factor is the fact that the stress field does not decline after the crack has propagated through the region. The applied stress field was left constant throughout the analysis, and likely increased the steady-state crack velocity. However, for the purposes of analyzing the effect of velocity on the CTOA the model will suffice.

The CTOA as a function of crack extension can be seen in Figure 8.8. The CTOA is stable throughout the propagation of the ligament of the model. The average SS-CTOA values are listed in Table 8.4. As can be seen the CTOA is largely unaffected by the rate at which the crack propagates. This is due to the fact that the material deforms in the same manner at the crack tip regardless of the rate at which the crack propagates.

### *X100 Results*

The crack extension as a function of time for the X100 material can be seen in Figure 8.9 and the steady-state crack velocities are listed in Table 8.3. Similar to the DWTT model the steady-state portion of the crack extension – time curve was determined to be when the CTOA reached an approximately constant value. As expected with increasing applied stress, the velocity of the crack is increased. Similar to the X70 model, the crack velocities are unrealistically high. However, for the purposes of analyzing the effect of velocity on the CTOA the model will suffice.

The CTOA as a function of crack extension can be seen in Figure 8.10. The CTOA is quite stable throughout the ligament of the model. The average SS-CTOA values are listed in Table 8.4. As can be seen, the CTOA is largely unaffected by the rate at which the crack propagates. This is due to the fact that the material deforms in the same manner at the crack tip regardless of the rate at which the crack propagates.

The analyses presented the same general result for both materials, namely, that the CTOA, wasn't significantly affected by the increase in crack velocity. The reason for this is that excluding the effect of bulk material rate hardening did not cause any change in the yield stress level at the crack tip. This caused the flank to deform in the same manner regardless of the rate at which the crack propagated. This shows that when the CZM is used, and material rate hardening is neglected, the CZM generates a constant CTOA.

### 8.3.2 Including Material Rate Hardening

Material rate hardening was introduced to the model in the same manner as Chapter 7. The models were first analyzed with the quasi-static TSL, including the effects of bulk material rate hardening. Following this, the cohesive energy was adjusted, based on trial and error, similar to Section 7.4, until the SS-CTOA matched the experimental values of  $12.5^{\circ} \pm 1^{\circ}$  for X70 and  $9.7^{\circ} \pm 1^{\circ}$  for X100. The main parameters examined in this analysis were the effect on the CTOA and the CVDFR. The following sections present the specific results for each material.

#### *X70 Results*

The crack extension as a function of time for the rate hardening model, with the quasi-static TSL, can be seen in Figure 8.11 with the steady-state crack velocities listed in Table 8.5. Simulating the plate model with elevated loading rates presented unrealistic crack velocities on the order of 1500m/s. The SS-CTOA of these models was reduced to approximately  $3^{\circ}$ - $4^{\circ}$ . This is the same observation as seen in Section 7.3. The models were then updated based on matching the experimental dynamic CTOA ( $12.5^{\circ} \pm 1^{\circ}$ ). The updates were introduced in the same manner as Section 7.4, specifically, the TSL was increased maintaining the same shape. The updated crack extension as a function of time data can be seen plotted in Figure 8.12 with the steady-state crack velocities listed in Table 8.6. The updated cohesive energy for the models are listed in Table 8.7

The CVDFR data for the model (including bulk material hardening) with no update to the TSL is compared to the model with the TSL updated for a constant CTOA in Figure

8.13. As can be seen, once the TSL is updated for the constant CTOA the steady-state crack velocities are drastically reduced.

The CVDFR for the models updated for constant CTOA are compared to the CVDFR of the models excluding material rate hardening and using a quasi-static TSL (Section 8.4.1) in Figure 8.14. From the comparison, it is evident that there is a very small difference between the two curves. Thus, the model including material rate hardening updated for a constant CTOA produces the same CVDFR as the model with no inclusion of rate hardening and a quasi-static TSL. This result supports the findings of Section 8.3.1, namely, that the CZM when used with no material rate hardening is a constant CTOA model.

Similar to Section 7.4, the effect of loading rate on the TSL was assessed for higher crack velocities. The cohesive energy as a function of crack velocity for the models including bulk material hardening can be seen in Figure 8.15. The plate data is plotted with the DWTT data from Section 7.4. The function of  $\Gamma_{Dynamic, X70}$ , from Section 7.4, was not re-assessed with the plate model data; however, the trend between the two models can be observed. As can be seen, the plate model data follows a similar trend as the DWTT data. This analysis has shown that the cohesive energy is adjusted in a similar manner as the rate dependent yield stress of the bulk material hardening law. Further investigation into a possible relation will be required.

### *X100 Results*

The crack extension as a function of time for the rate hardening model with no TSL update can be seen in Figure 8.16 with the steady-state crack velocities listed in Table 8.5.

Simulating the plate model with elevated loading rates presented unrealistic crack velocities on the order of 1500 m/s. The SS-CTOA of these models were reduced to approximately 2°-3°. This is the same observation as not in Section 6.5. The models were then updated based on matching the experimental CTOA ( $9.7 \pm 1^\circ$ ). The updated crack extension as a function of time data can be seen plotted in Figure 8.17 with the steady-state crack velocities listed in Table 8.6. The cohesive energy required to produce the constant CTOA are listed in Table 8.7.

The CVDFR curves for the model with no update to the TSL is compared to the model with the TSL updated for a constant CTOA in Figure 8.18. As can be seen, once the TSL is updated for the constant CTOA the steady-state crack velocity is drastically reduced. The CVDFR for models updated for constant CTOA are compared to the CVDFR of the models with no inclusion of material rate hardening and a quasi-static TSL in Figure 8.19. Similar to the X70 results the two curves are nearly identical. This supports the main observation of this section, that the CZM when used to simulate higher loading rates is inherently a constant CTOA model.

Similar to Section 7.4, the effect of loading rate on the TSL was assessed for higher crack velocities. The cohesive energy as a function of crack velocity can be seen in Figure 8.20. The function of  $\Gamma_{dynamic, X100}$ , from Section 7.4, was not re-assessed with the plate model data; however, the trend between the two models can be observed. A similar trend to X70 was observed, namely, that the cohesive energy increased with crack velocity in a similar manner to that of the yield stress with increasing strain rate. Further investigation into a possible relation between the rate dependent material yield stress and cohesive energy/maximum traction will.

#### **8.4 Results and Discussion – Influence of Inertia**

The effect of inertia was only examined with the X70 material. When simulating full scale pipe models it is a challenge to model the interaction of the pipe and the backfill. A common technique used in the work of (O'Donoghue, Kanninen, Leung, Demofonti, & Venzi, 1997) was to scale the density of the pipe material, increasing the resistance to motion and thus accounting for the soil without its explicit inclusion in the model. This assumption though practical and computationally efficient has the potential to effect the numerical results. The plate model was analyzed with the quasi-static material properties and the quasi-static TSL parameters. The density of the model was altered to examine the effect of inertia. Essentially, the fracture process and the material properties were not altered with respect to rate, which highlighted the direct effect of inertia.

The crack extension as a function of time is plotted in Figure 8.21, Figure 8.22, and Figure 8.23 for the unscaled density, 1.5x density and 2x density, respectively. The crack extension as a function of time was determined from the model in the same manner as discussed in Section 7.3.2. The steady-state crack velocity was determined by fitting a linear trend line to the linear portion of the curve. The steady-state portion of the time extension curves were determined to be when the CTOA appeared to stabilize.

The CVDFR for all three models are shown in Figure 8.24, with the steady-state crack velocities listed in Table 8.8. As the mass of the model was increased the limiting velocity (upswing) was decreased. Intuitively this makes sense as the increase of the mass, increases the inertial resistance of the material and results in the crack propagating at a slower rate. The sudden upswing as the applied stress is increased is present in all models regardless of the mass. It appears as though the mass scaling used affected the magnitude

of the limiting velocity; reducing it as the mass increased. The presence of the upswing, while neglecting rate hardening, strongly supports the notion that the upswing is predominantly an inertial effect. For a more realistic and quantifiable effect on the numerical results this work will be extended to a pipe geometry.

Of course, the results of this analysis are purely qualitative as the geometry of the specimen and the loading conditions do not accurately reflect the physical process. However, utilizing the CZM and neglecting the effect of material rate hardening, this confirms that the upswing is influenced by the inertial resistance of the model.

The second parameter examined in the mass scaling analysis was the effect of mass scaling on the SS-CTOA. The CTOA and crack extension as a function of time can be seen in Figure 8.25-8.29. The average SS-CTOA values are tabulated in Table 8.9. It is evident that the CTOA was not significantly affected by the alteration of the density of the model. Each applied stress showed very little difference between the CTOA measured from the model. This demonstrates that altering the density of the model does not introduce any unexpected affect the SS-CTOA measured.

Moreover, the results further demonstrate that there is a coupled effect on the upswing in the CVDFR; the first part from the density of the model and the second from the fracture process parameters i.e. the TSL (CTOA). The density of the model was proven to only affect the location of the upswing of the CVDFR and not the CTOA. As shown in the work of (Ben Amara, 2015), the CTOA (toughness) affects the magnitude of the limiting velocity as well. This demonstrates the importance of properly modelling backfill when simulating ductile fracture in pipeline models.

## 8.5 Conclusions

A plate model, simplified from a pipe geometry, was used to investigate the effect of mass scaling on the steady-state crack velocity and the CTOA. Furthermore, the model was utilized to further the study performed in Chapter 7, and investigate the effect of crack velocity on the CTOA and the CVDFR.

The results of the mass scaling analysis demonstrate that the upswing in the CVDFR is an inertia dominated effect. It was shown that increasing the mass of the model reduces the limiting velocity in the CVDFR. Moreover, the use of mass scaling in a dynamic model presented no significant effect on the measured CTOA of the model.

Lastly, it was shown that the use of the CZM, neglecting bulk material hardening, to simulate crack propagation at higher loading rates is inherently a constant CTOA model. This was shown in two parts; the first was by examining the model at different loading rates with rate independent material properties (quasi-static TSL) and observing very little change in the CTOA. The second was from updating the TSL to produce a constant CTOA in the model accounting for rate hardening, and simultaneously producing an almost identical CVDFR to the one generated from the model with no rate hardening and a quasi-static TSL.

In conclusion, the main contributions of this chapter are as follows. It was confirmed that the upswing in the CVDFR is an inertia dominated effect. Furthermore, it was also shown that the CZM when used with a rate independent material model yields a constant CTOA.

**Table 8.1 - Plate model dimensions.**

Material	Pipe Diameter (mm)	Pipe Circumference (mm)	Flank Height ( <i>H</i> ) (mm)
X70	914.4	2872.8	718
X100	1219.2	3830.2	957

**Table 8.2 - Finite element mesh details of plate model.**

Material	Part	Zone	Element Types	Number of Elements	Nominal Size (mm)
X70	Plate Specimen	Ligament	CPE4R	10,500	1X1
		Transition	CPE4R/ CPE3	27,405	N/a
		Bulk	CPE4R	2016	40X40
	Crack	Cohesive Layer	COH2D4	11,667	0.3x0.01
X100	Plate Specimen	Ligament	CPE4R	10,500	1X1
		Transition	CPE4R/ CPE3	27,405	N/a
		Bulk	CPE4R	3510	40X40
	Crack	Cohesive Layer	COH2D4	11,667	0.3x0.01

**Table 8.3 - Steady-state crack velocities excluding material rate hardening.**

Applied Stress (MPa)	Steady-State Crack Velocity (m/s)	
	X70	X100
100	335	583
200	409	690
300	448	747
400	475	776
500	490	795
600	-	804
700	-	810

**Table 8.4 - Average steady-state CTOA excluding material rate hardening.**

Applied Stress (MPa)	Average Steady-State CTOA (Degrees)	
	X70	X100
100	12.1	10.0
200	12.3	10.3
300	12.8	10.2
400	12.7	10.1
500	12.8	10.1
600	-	10.2
700	-	10.0

**Table 8.5 - Steady-state crack velocity - Material rate hardening (no TSL update).**

Applied Stress (MPa)	Steady-State Crack Velocity (m/s)	
	X70	X100
100	1391	1257
200	1500	1399
300	1578	1530
400	1632	1638
500	1680	1710
600	-	1764
700	-	1796

**Table 8.6 - Steady-state crack velocity - Material rate hardening (TSL updated for constant CTOA).**

Applied Stress (MPa)	Steady-State Crack Velocity (m/s)	
	X70	X100
100	Did not propagate	503
200	405	660
300	450	734
400	470	771
500	481	794
600	-	796
700	-	804

**Table 8.7 – Cohesive energy updated for constant CTOA.**

Applied Stress (MPa)	Cohesive Energy (Updated constant CTOA) (MPa-mm)	
	X70	X100
100	N/A	211.9
200	167.3	213.2
300	168.6	215.2
400	169.3	216.3
500	169.9	217.3
600	-	217.9
700	-	218.7

**Table 8.8 – Steady-state crack velocities for mass scaling analysis.**

Applied Stress (MPa)	Steady-State Crack Velocity (m/s)		
	Unscaled mass	1.5x mass	2x mass
100	335	273	239
200	409	337	292
300	448	362	315
400	475	380	332
500	490	398	344

**Table 8.9 – Average steady-state CTOA for mass scaling analysis.**

Applied Stress (MPa)	Average Steady-State CTOA (Degrees)		
	Unscaled mass	1.5x mass	2x mass
100	12.1	11.9	11.8
200	12.3	12.5	12.0
300	12.8	12.2	12.5
400	12.7	12.4	11.9
500	12.8	12.6	12.5

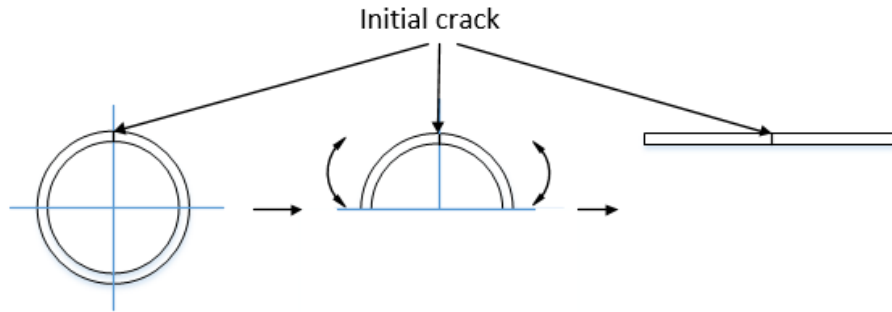


Figure 8.1 - Simplification of pipe to a tensile plate.

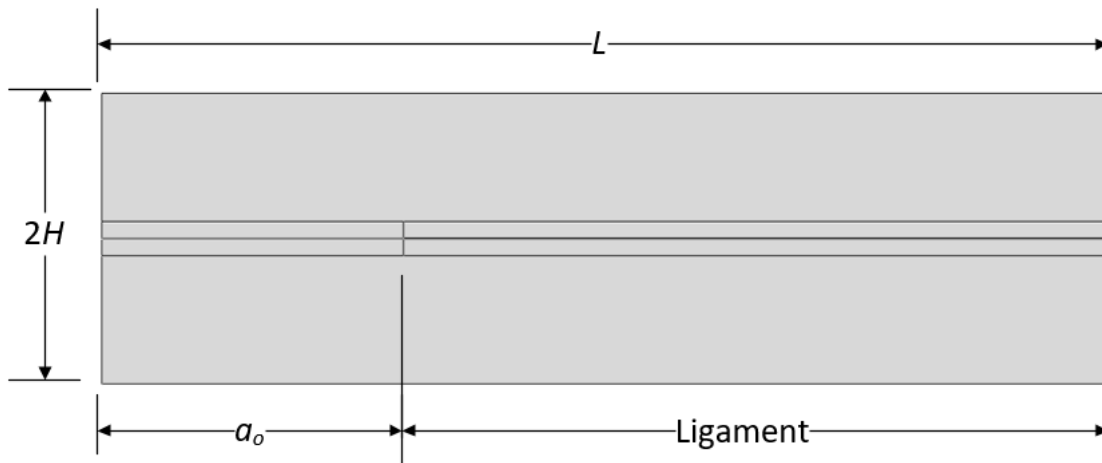
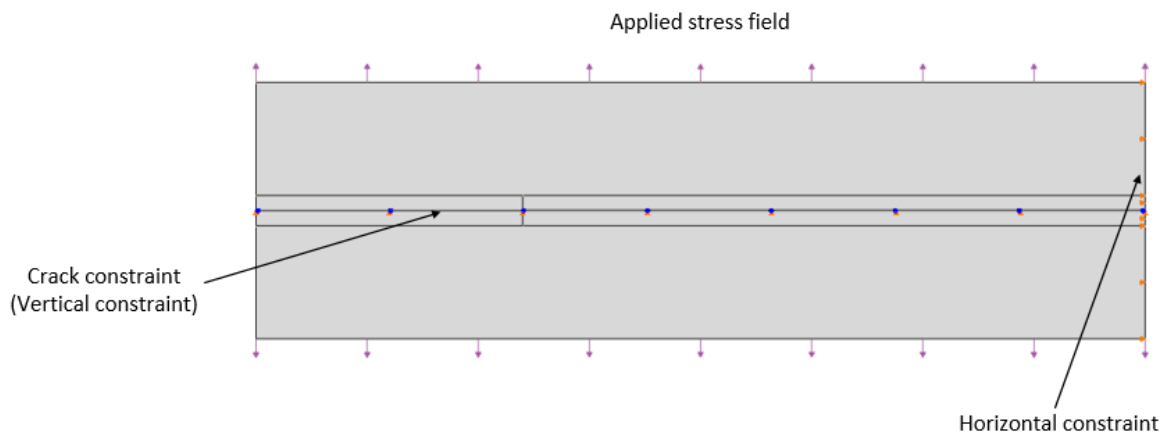
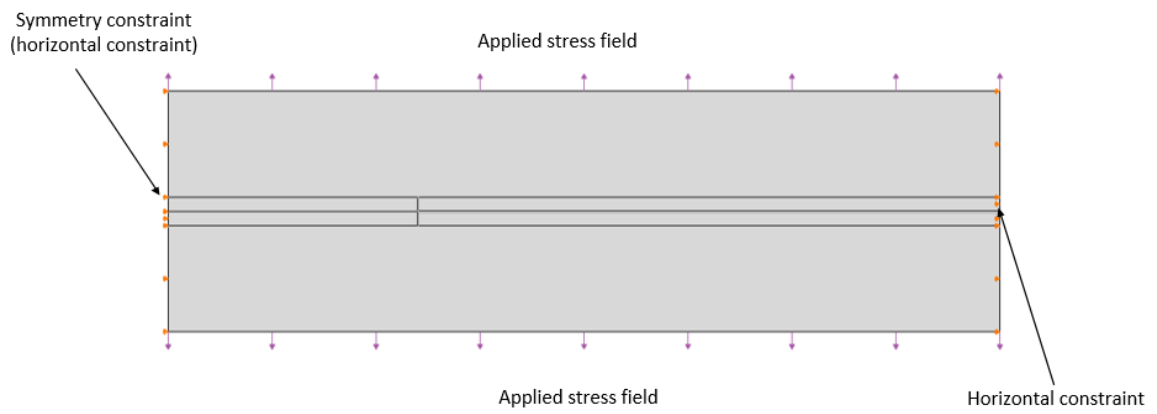


Figure 8.2 - Plate model geometry.



**Figure 8.3 - Plate model loading conditions - first step.**



**Figure 8.4 - Plate model loading conditions - second step.**

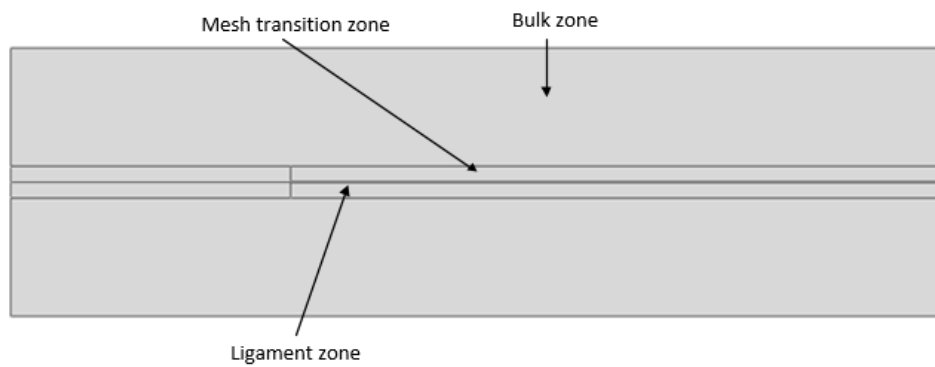


**Figure 8.5 - Plate model mesh zones.**

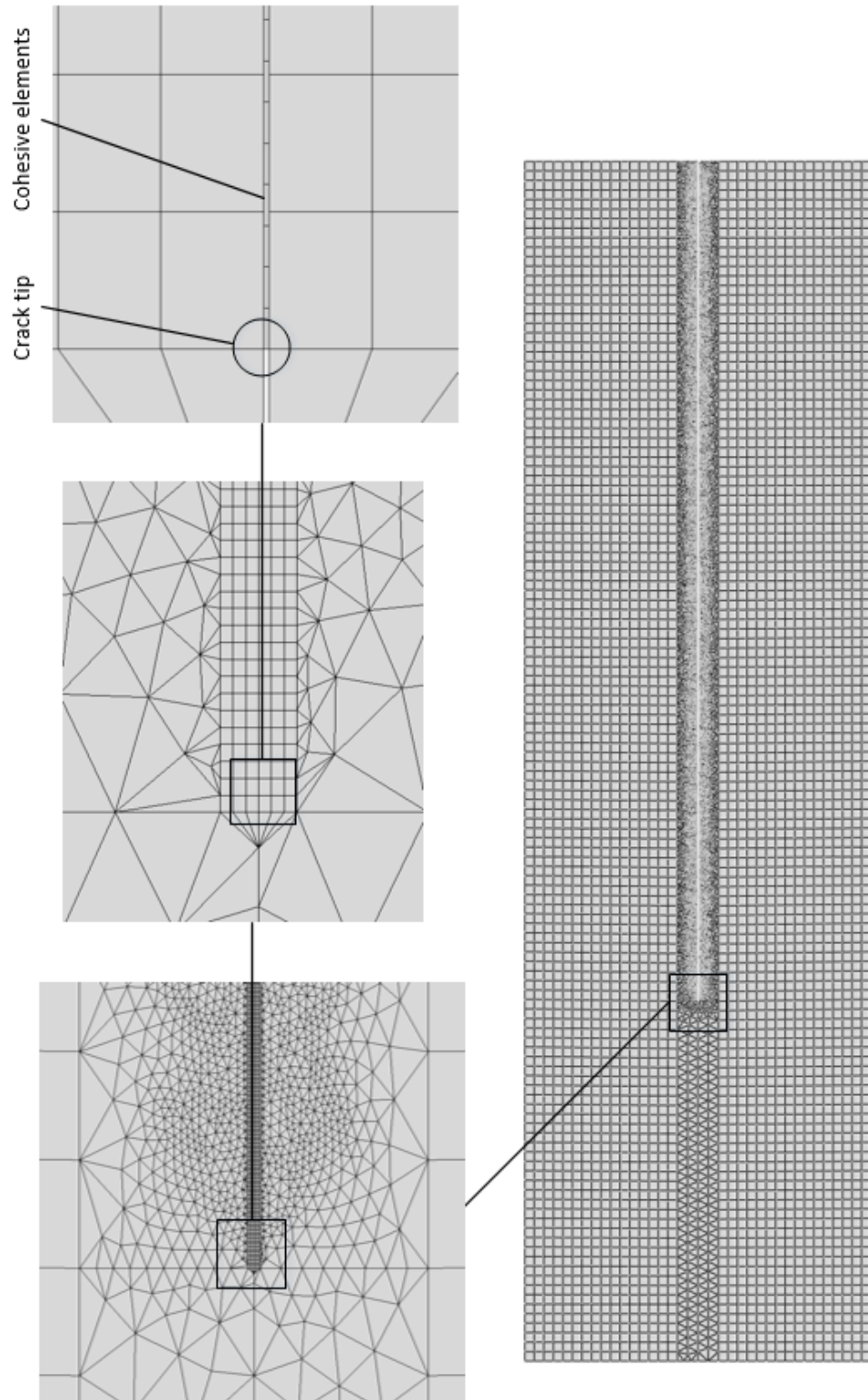


**Figure 8.6 - Plate model FE mesh design.**

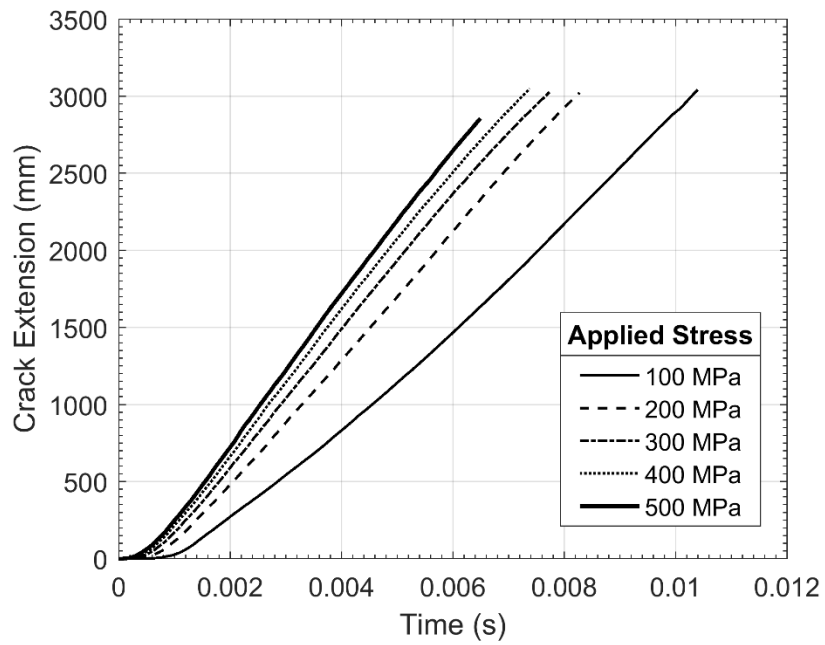


Figure 8.7 - Crack extension as a function of time - X70 excluding material rate hardening.

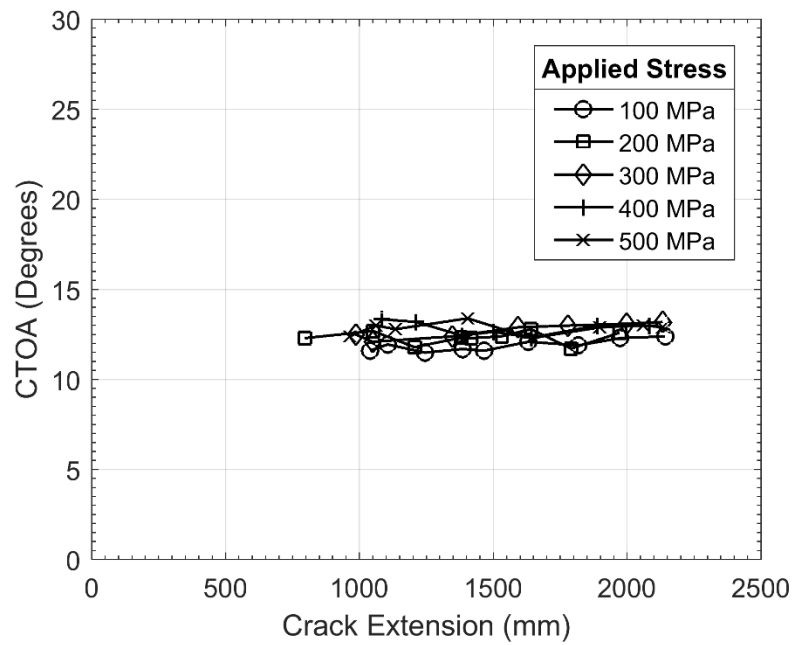


Figure 8.8 - CTOA as a function of crack extension - X70 excluding material rate hardening.

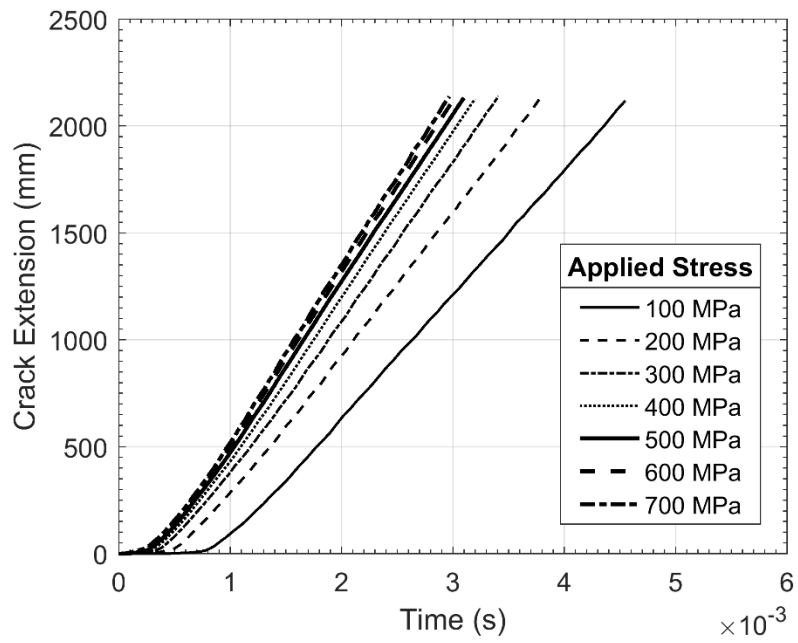


Figure 8.9 - Crack extension as a function of time – X100 excluding material rate hardening.

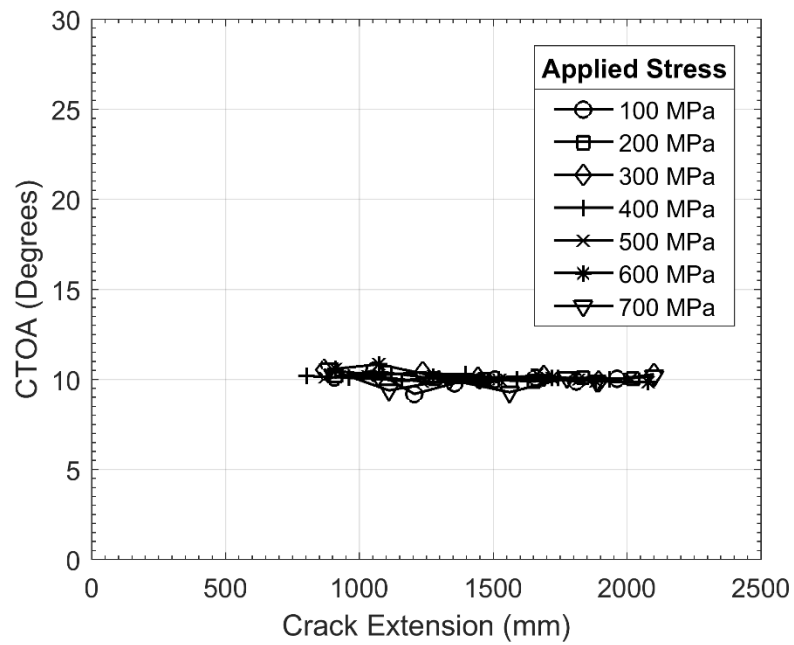


Figure 8.10 - CTOA as a function of crack extension – X100 excluding material rate hardening.

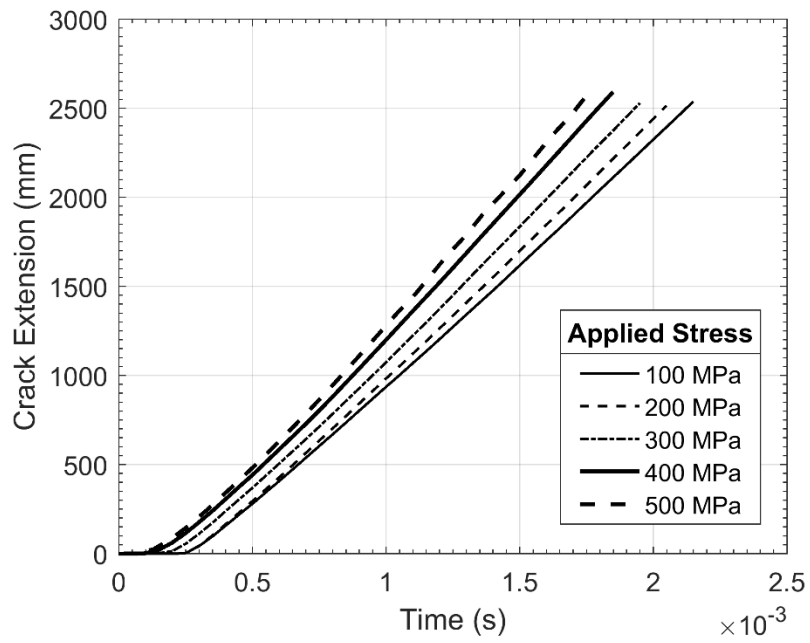


Figure 8.11 - Crack extension as a function of time – X70 material rate hardening (no TSL update).

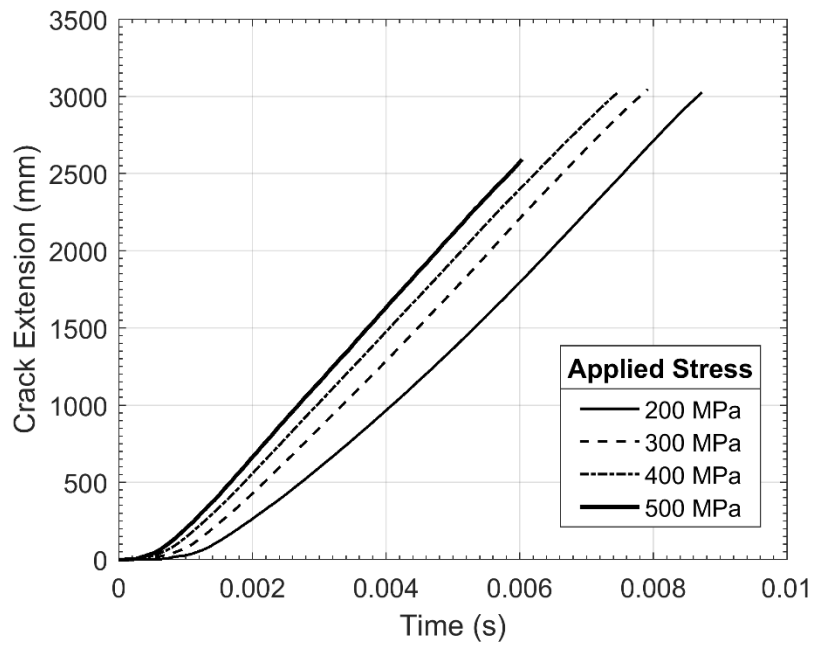


Figure 8.12 - Crack extension as a function of time – X70 material rate hardening (TSL updated constant CTOA).

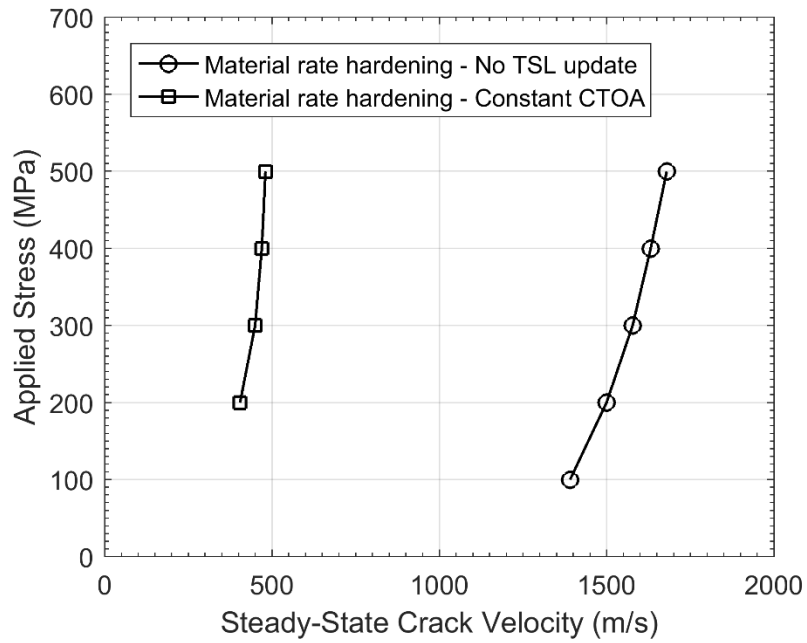


Figure 8.13 - CVDFR – X70 comparing quasi-static TSL to constant CTOA updated TSL.

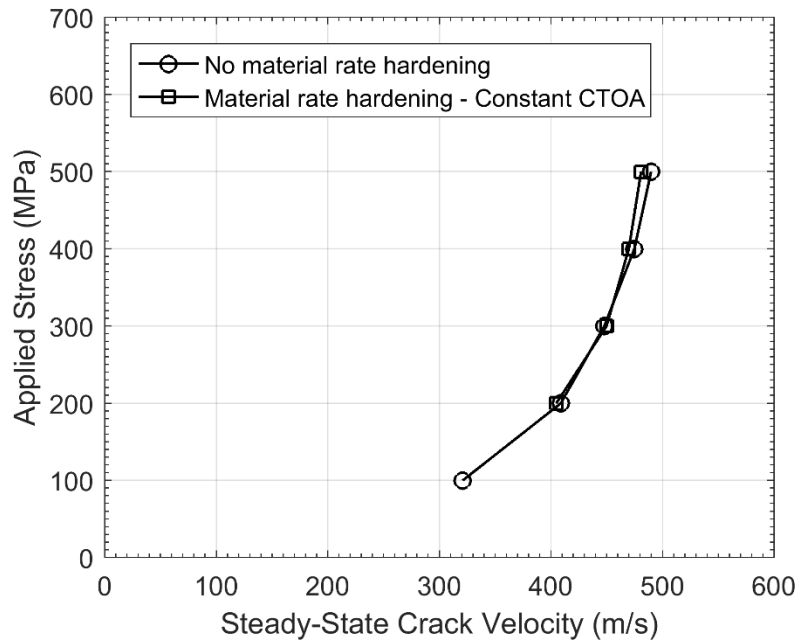


Figure 8.14 - CVDFR – X70 comparing rate insensitive model to constant CTOA updated TSL.

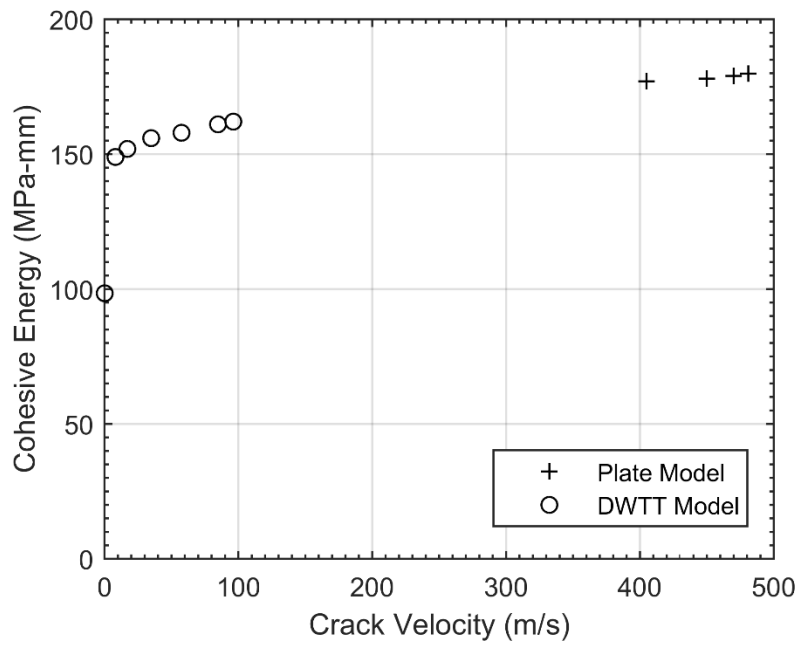


Figure 8.15 – X70 cohesive energy as a function of crack velocity.

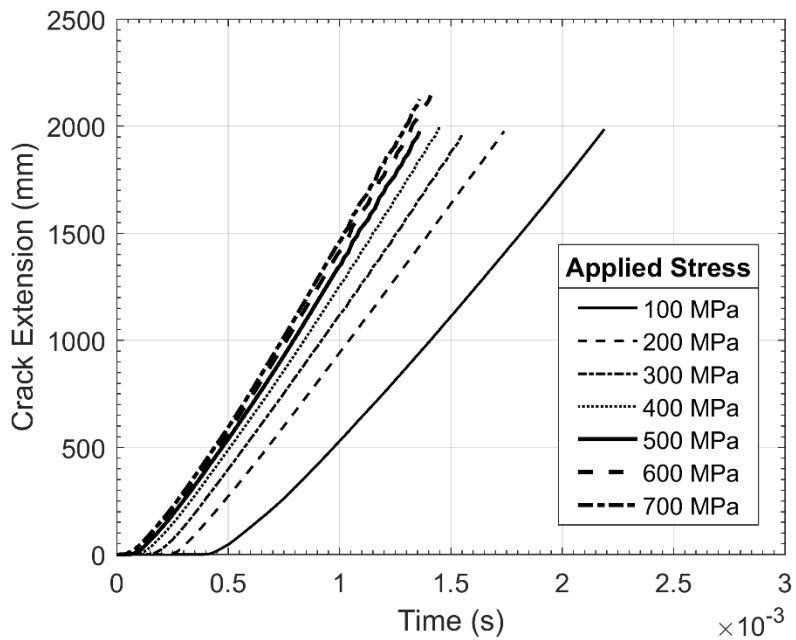


Figure 8.16 - Crack extension as a function of time - X100 material rate hardening (no TSL update).

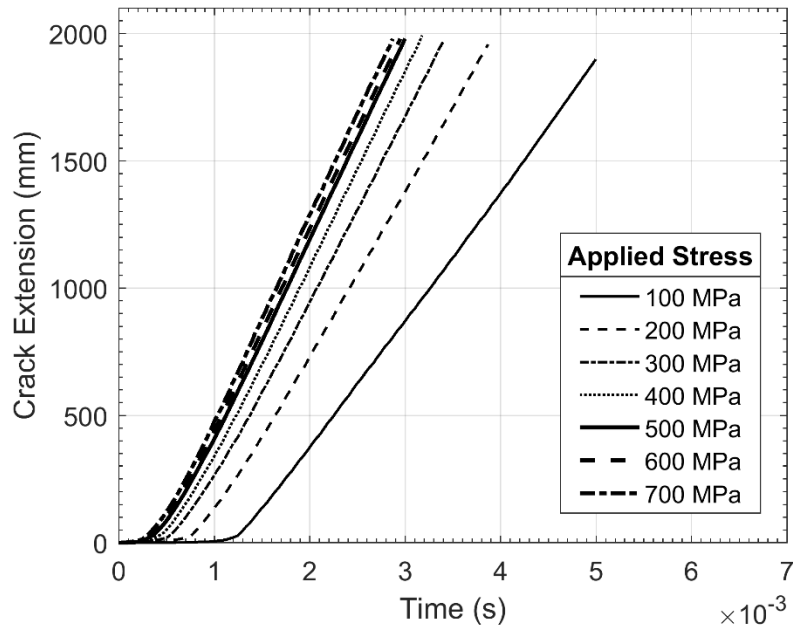


Figure 8.17 - Crack extension as a function of time – X100 material rate hardening (TSL updated constant CTOA).

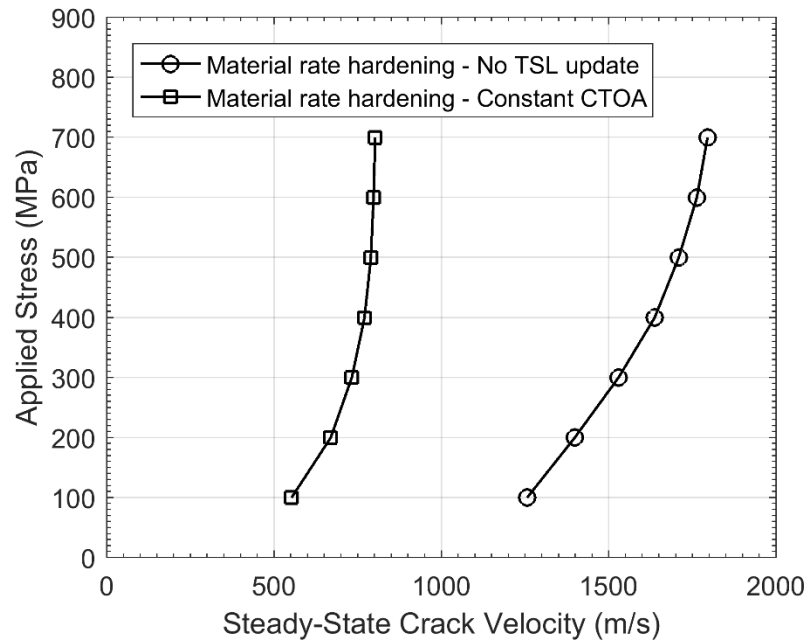


Figure 8.18 – CVDFR – X100 comparing quasi-static TSL to constant CTOA updated TSL.

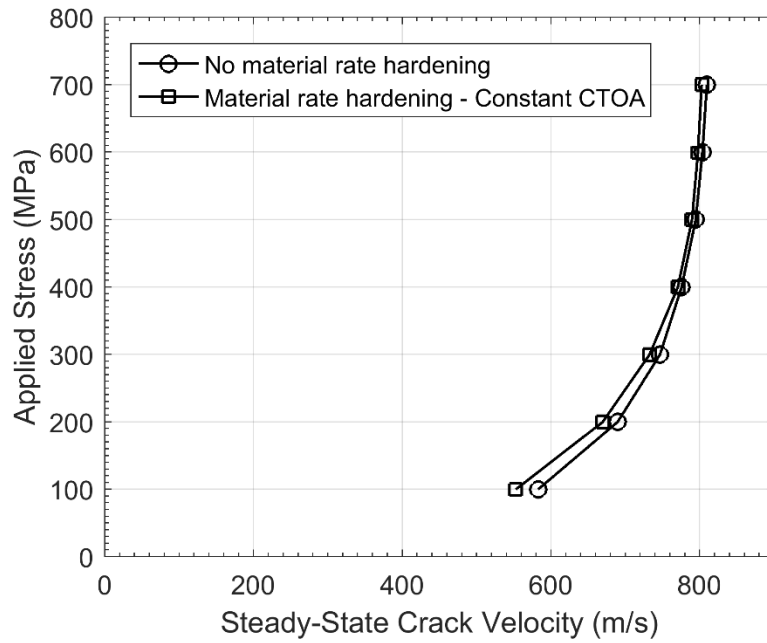


Figure 8.19 - CVDFR – X100 comparing rate insensitive model to constant CTOA updated TSL.

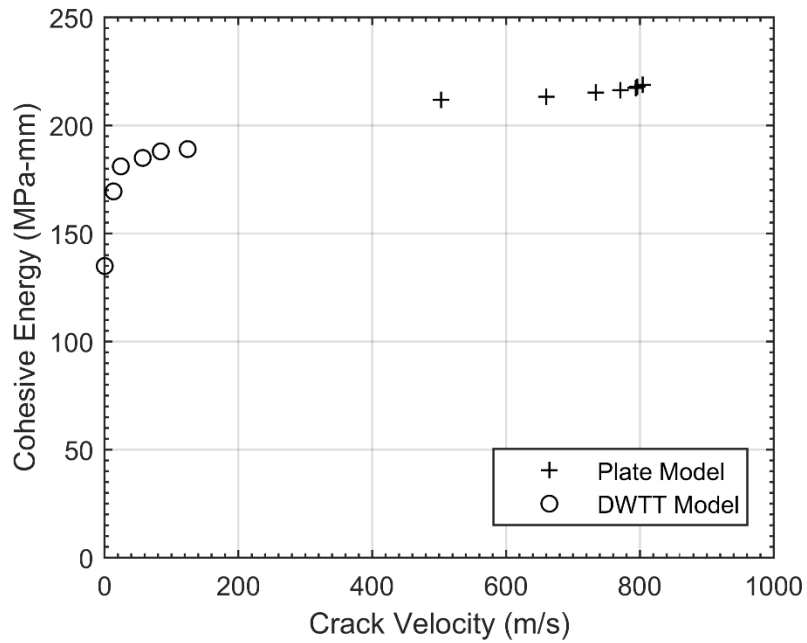


Figure 8.20 - X100 cohesive energy as a function of crack velocity.

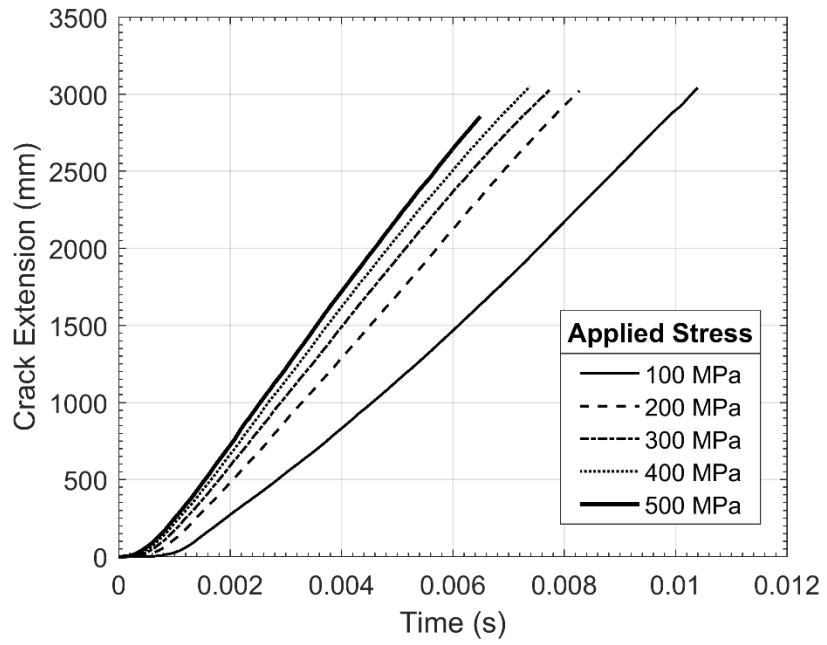


Figure 8.21 - Crack extension as a function of time - unscaled mass model.

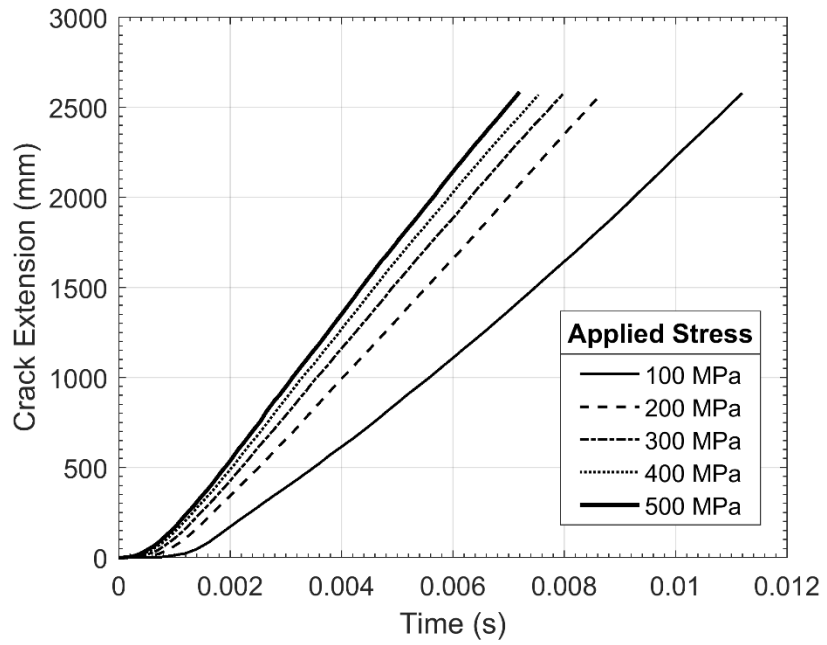


Figure 8.22 - Crack extension as a function of time – 1.5x density model.

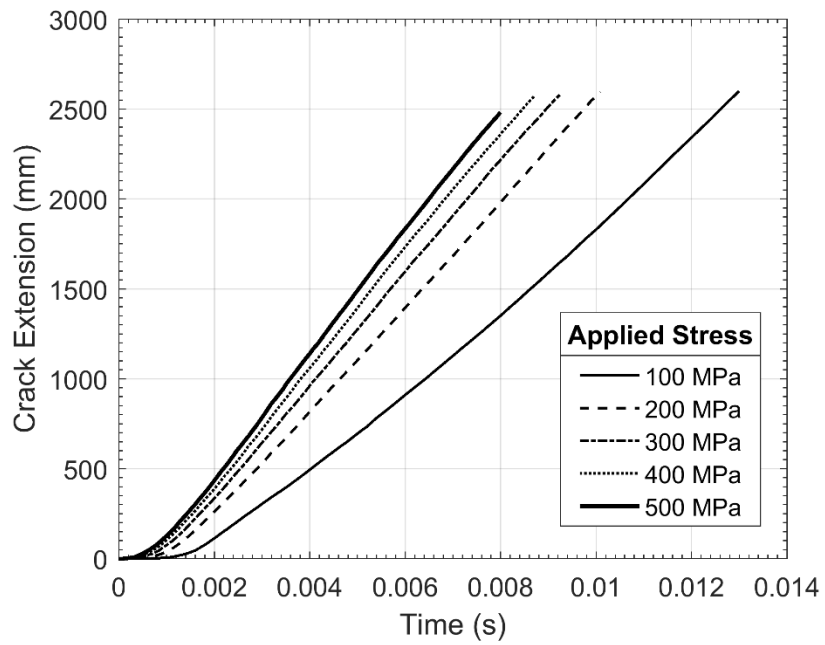


Figure 8.23 - Crack extension as a function of time – 2x density model.

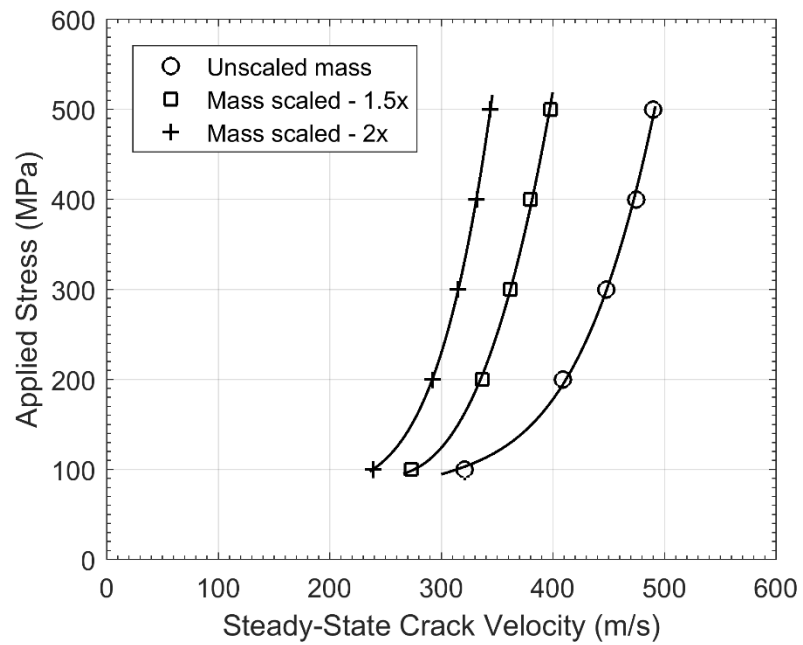


Figure 8.24 - Applied stress as a function of steady-state crack velocity.

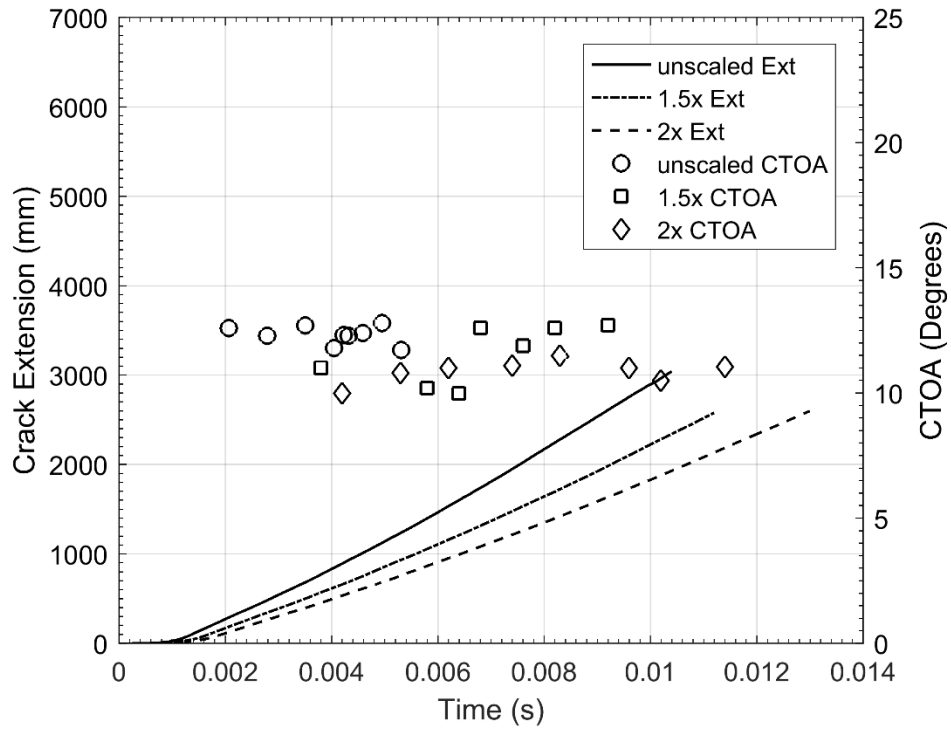


Figure 8.25 - Crack extension and CTOA as function of time – 100 MPa models.

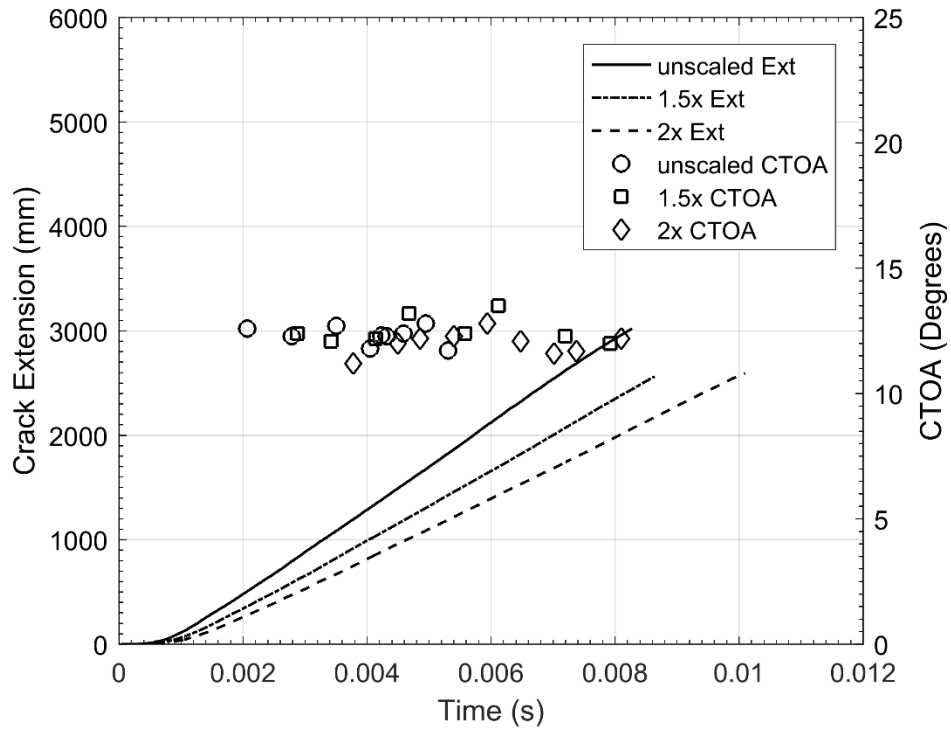


Figure 8.26 - Crack extension and CTOA as function of time - 200 MPa models.

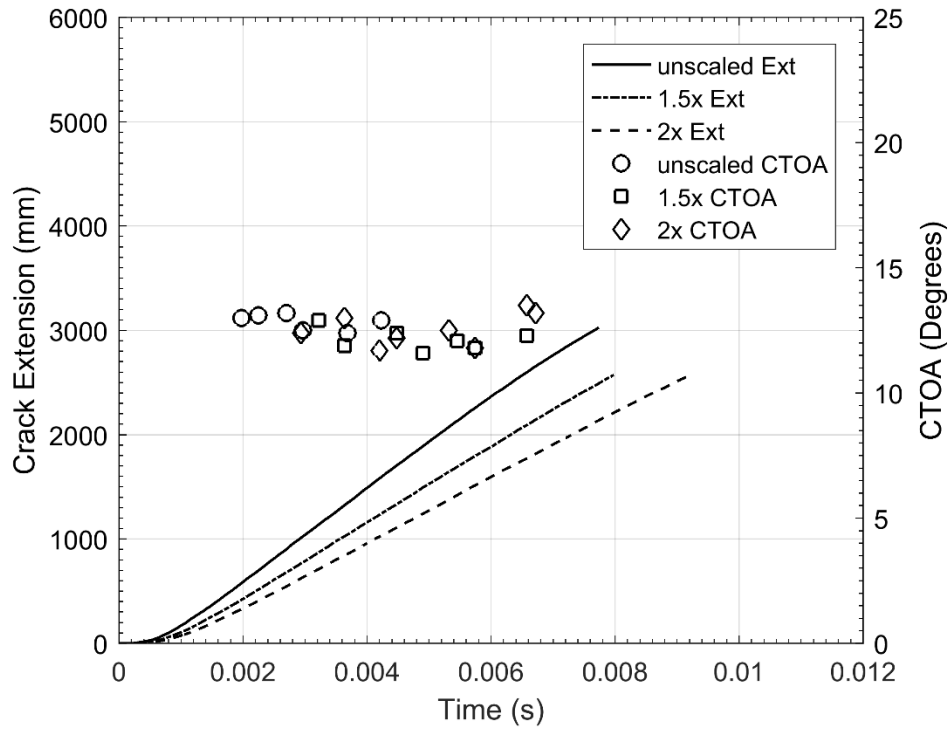


Figure 8.27 - Crack extension and CTOA as function of time - 300 MPa models.

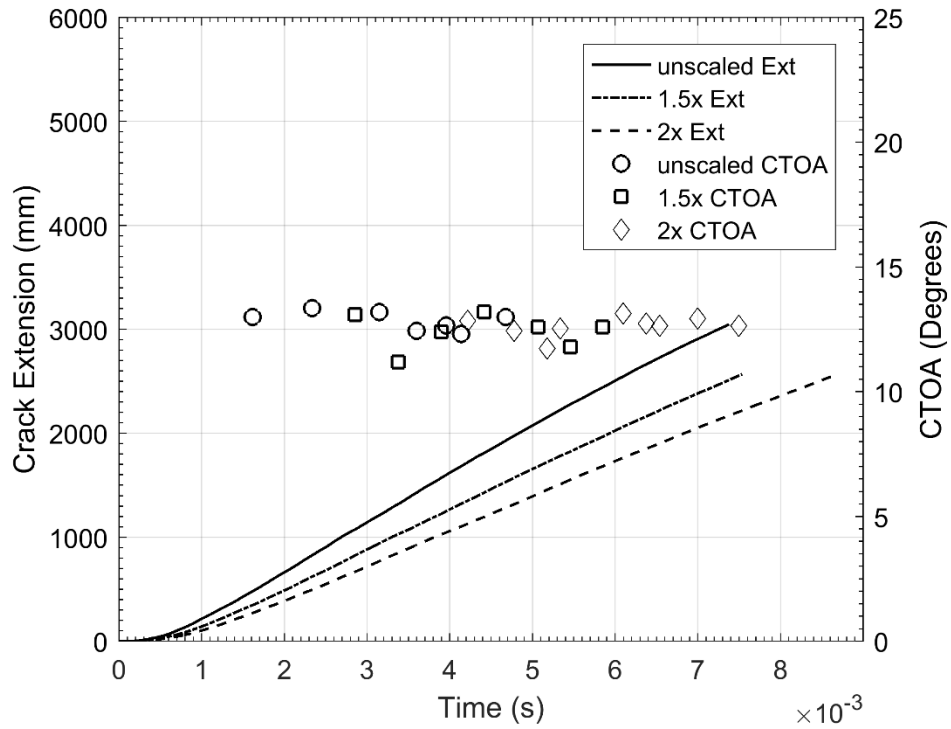


Figure 8.28 - Crack extension and CTOA as function of time - 400 MPa models.

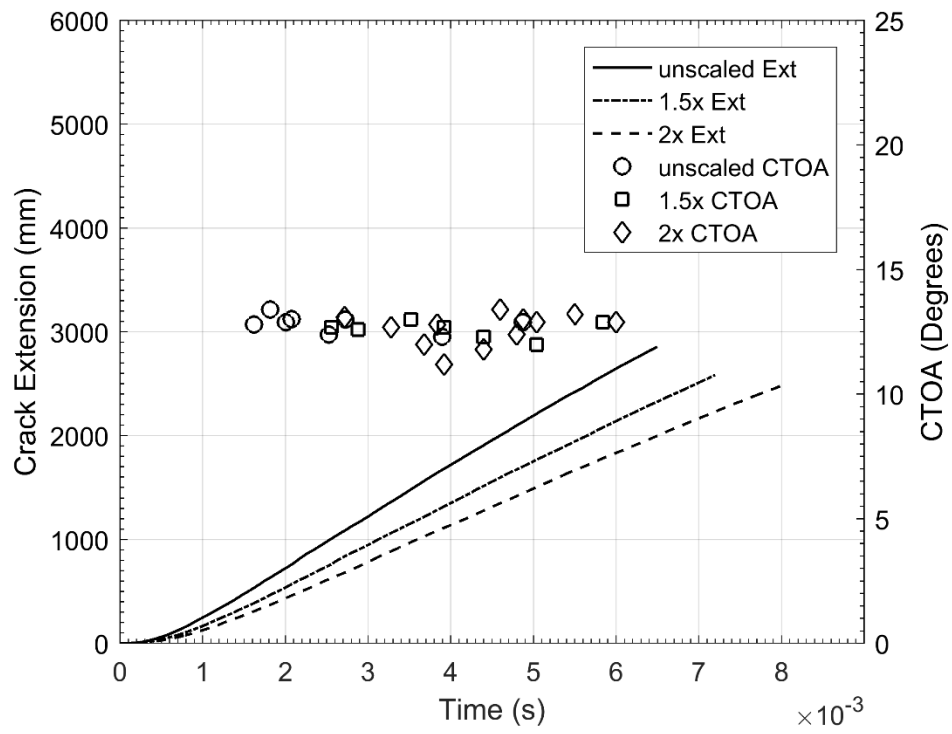


Figure 8.29 - Crack extension and CTOA as function of time - 500 MPa models.

## **Chapter 9: Conclusions and Future Recommendations**

### **9.1 Conclusions**

Numerical investigations of ductile fracture in pipeline steels are of significant interest to the pipeline industry as they provide a cost efficient alternative to expensive testing. The objective of this research was to examine the effect of loading mode, under quasi-static loading conditions, and higher loading rates on the CTOA. The concluding remarks of the various analyses performed are summarized below.

#### *Effect of TSL shape on the results of a Propagation Analysis (Chapter 4)*

The effect of the TSL shape was analyzed through examining an SSY model under quasi-static loading conditions. The results of the analysis demonstrate that the shape of the TSL has a significant effect on the results of a propagation analysis. It was shown that given the same cohesive parameters, and merely changing the shape from bilinear to variations of the trapezoidal law, the measured CTOA and the crack growth resistance of the model was increased with increasing plateau size. The most significant change was observed through comparing the bilinear and trapezoidal-1/4 law. There was very little difference in crack growth resistance and CTOA between the three trapezoidal shapes. This analysis demonstrated that changing the TSL shape for a rate update has an effect on the CTOA, and to minimize the number of parameters which affect the CTOA, the shape should be left constant.

### *Effect of Loading Mode (Constraint) on the CTOA (Chapter 5)*

The effect of loading mode on the CTOA was investigated by comparing a tensile model to a bending model under quasi-static loading conditions. The tensile model was modeled as a clamped end condition SENT specimen, and the bending model was modeled as a DWTT specimen. It was shown that though the two models were identical in terms of model properties and geometry, the variation in CTOA was small, showing that constraint has only a minor effect on the CTOA. With such a slight effect on the CTOA, this work confirms the notion that the CTOA is transferrable between loading modes under quasi-static loading conditions.

### *Quasi-Static DWTT Simulations (Chapter 6)*

The quasi-static DWTT model was examined with both X70 and X100. The TSL's were calibrated so as to produce the experimental CTOA. This was done to assess the CTOA as a TSL calibration parameter. This was assessed through examining and comparing the FE results with the experimental Load-LLD data. Good agreement with the experimental Load-LLD data (post initiation) was seen with both materials. In calibrating the model to produce the experimental CTOA, the post initiation slope of the Load-LLD curve was recreated. This verifies the use of the CTOA as a calibration parameter for both X70 and X100.

### *Effect of Loading Rate on the CTOA (Chapter 7)*

The DWTT model was simulated at an impact loading rate, first with rate sensitive material properties and the quasi-static TSL. Both materials presented a large drop in CTOA to approximately 2-4° for both X70 and X100. As well, a large drop in post-initiation slope of the Load-LLD data was observed. This demonstrates that the TSL must vary with loading rate if the CTOA is to remain constant with respect to loading rate.

The TSL was then updated based on matching the experimental dynamic CTOA. Calibrating the impact models to match the experimental CTOA produced good agreement with the Load-LLD data (post-initiation slope), similar to the quasi-static models. As well, after the update was applied X70 presented a crack velocity of 8.3 m/s which is in good agreement with a value from literature. This demonstrates that updating the model to produce the experimental CTOA also re-produces other experimental quantities (crack velocity, Load-LLD data). The results suggest further research is required to be able to use the CZM as a rate predictive tool.

The influence of loading rate on the cohesive energy was assessed assuming that the CTOA is independent of loading rate. The results demonstrate that the cohesive energy must increase with increasing crack velocity to maintain a constant CTOA.

### *Effect of Loading Rate on the CTOA – Continued (Chapter 8)*

The plate model was first simulated at higher loading rates with rate insensitive material properties and a rate insensitive fracture process zone (quasi-static TSL). The results of this analysis demonstrated that there was no significant effect on the CTOA. This result was observed for both materials. With regards to X70, the SS-CTOA remained in

the range of 12.1°-12.8° and remained in the range of 10.0°-10.3° X100. Thus it is evident that when the CZM is utilized with a rate insensitive bulk material model and rate insensitive fracture process zone the crack propagates with an essentially constant CTOA independent of loading rate.

Bulk material rate hardening was then introduced into the models, and the TSL was updated to produce the experimental dynamic CTOA from the DWTT experiments. The focus of this analysis was comparing the CVDFR of the rate sensitive model (updated for constant CTOA) to the rate insensitive model (quasi-static TSL). The comparison for both materials presented the same trend, namely, that the rate sensitive model updated for constant CTOA produced an almost identical CVDFR curve to the rate insensitive material model (quasi-static TSL). This demonstrates that for the purposes of the material resistance data of the TCM, the CZM is essentially a constant CTOA model.

#### *Effect of Inertia on the CVDFR and CTOA (Chapter 8)*

The effect of inertia was studied through examining a large tensile plate model simplified from a pipe geometry with the X70 material. This analysis involved using the model with rate insensitive material properties and a rate insensitive fracture process zone (quasi-static TSL). The density of the model was then scaled to assess the effect of inertia on the CVDFR and the CTOA. The results demonstrate that the upswing in the material resistance curve is sensitive to the density of the model, i.e. is predominantly an inertial effect. The upswing was observed in all three models. It can be concluded that the mass of the model affected the magnitude of the limiting velocity (lowering the velocity with increasing mass). Moreover, the results demonstrate that the CTOA is not sensitive to the

mass of the model. The average steady-state CTOA values of the models were in the range of 11.8°-12.8°. This range presents no significant change from the calibrated value of 12.4°.

## **9.2 Thesis Applications and Limitations**

The contents herein are targeted towards the simulation of ductile fracture of structures which experience loading rates higher than quasi-static using the cohesive zone model. Specifically, the calibration of high strength and high toughness materials is explored and a first approximation is developed for the CZM parameters of X70 and X100 steels. These CZM parameters are further investigated through analyzing how they change with increasing crack velocity. Some applications in which this work would apply include the modelling of fracture in large scale engineering structures in which the complex micromechanical fracture process can be approximated by a traction-separation law. More specifically, other applications would include the rate dependent debonding of adhered components in aerospace applications, fracture of large panels in ships, analysis of offshore oil platforms and airplane skins.

Some limitations in this work include those inherent with the use of the CZM; namely, that the direction and path of crack propagation is defined prior to the analysis with the insertion of the cohesive elements. This limits the application to loading modes where the crack path can be accurately predicted based on the loading conditions, geometry, and stress concentrations.

### 9.3 Recommendations for Future Work

The practical application of this research is to develop a ductile fracture model to be used for long running crack propagation analyses in natural gas pipelines. This section is dedicated to recommendations on possible research topics for advancement of the model.

1. Compare the results of a CZM analysis to those of a constant CTOA criterion model, focusing on a model with rate independent material parameters and a quasi-static calibrated CTOA. A comparison of the numerical stability and computational efficiency of the two models would be of interest.
2. Conduct a parametric study on the TSL shape, the maximum traction, cohesive energy and loading rate to assess the influence of rate on the TSL parameters. The idea with this study would be to relate the maximum traction to the yield stress of the bulk material at higher strain rates.
3. Examine the calibration of the TSL parameters (cohesive energy and maximum traction) for pipeline steels. The J-resistance values were only used as maximums for the cohesive energy in this work. Experimental tests could be performed to determine the SZW of the pipeline steels for a better approximation of the cohesive energy.
4. To provide a more quantifiable assessment of the effect of backfill (inertia) in a dynamic fracture model of a buried pipe, it would be recommended to extend the inertia analysis to a pipe geometry.
5. Examine the effect of biaxial stress on the CTOA.

## References

- ABAQUS. (2014). ABAQUS 6.14-2, 2014 - Analysis User's Manual.
- Alfano, G. (2006). On the influence of the shape of the interface law on the application of cohesive-zone models. *Composites Science and Technology*, 66(6), 723-730.
- Anderson, T. (2011). *Fracture Mechanics: Fundamentals and Applications*. Florida: CRC Press.
- Anvari, M., Scheider, I., & Thaulow, C. (2006). Simulation of dynamic ductile crack growth using strain-rate and triaxiality-dependent cohesive elements. *Engineering Fracture Mechanics*, 73(15), 2210-2228.
- ASTM E3039-16. (2016). *Determination of Crack-Tip-Opening Angle of Pipe Steels Using DWTT Specimens*. ASTM International.
- ASTM E436-03. (2014). *Standard Test Method for Drop-Weight Tear Tests of Ferritic Steels*. ASTM International.
- Barenblatt, G. (1962). The Mathematical Theory of Equilibrium Cracks Formed in Brittle Fracture. *Advances in Applied Mechanics*, 7, 55-129.
- Ben Amara, M. (2015). Mechanical Characterization of a Steel for the Transport of Supercritical CO<sub>2</sub>. PHD Thesis, Metz: National School of Engineers of Metz.
- Cerrone, A., Wawrzynek, P., Nonn, A., Paulino, G., & Ingraffea, A. (2014). Implementation and verification of the Park–Paulino–Roesler cohesive zone model in 3D. *Engineering Fracture Mechanics*, 120, 26-42.
- Darcis, P., McCowan, C., Wondhoff, H., McColskey, J., & Siewert, T. (2008). Crack tip opening angle optical measurement methods in five pipeline steels. *Engineering Fracture Mechanics*, 75(8), 2453-2468.

- Dassault Systemes. (2014). *ABAQUS Version 6.14-2*. Providence, USA: ABAQUS Inc.
- Demofonti, G., Mannucci, G., Hillenbrand, H., & Harris, D. (2004). Evaluation of the Suitability of X100 Steel Pipes for High Pressure Gas Transportation Pipelines by Full Scale Tests. *Internatrional Pipeline Conference* (pp. 1685-1692). Calgary: IPC2004-0145.
- Diehl, T. (2008). On using a penalty-based cohesive-zone finite element approach, Part I: Elastic solution benchmarks. *International Journal of Adhesion & Adhesives*, 28(4-5), 237-255.
- Duan, D.-m., Zhou, J., Shim, D.-J., & Wilkowski, G. (2010a). Effect of Fracture Speed on Ductile Fracture Resistance - Part 1: Experimental. *International Pipeline Conference* (pp. 539-545). Calgary: IPC2010-31310.
- Duan, D.-m., Zhou, J., Shim, D.-J., & Wilkowski, G. (2010b). Effect of Fracture Speed on Ductile Fracture Resistance - Part 2: Results and Application. *International Pipeline Conference* (pp. 201-208). Calgary: IPC2010-31021.
- Dugdale, D. (1960). Yielding of Steel Sheets Containing Slits. *Mechanics and Physics of Solids*, 8, 100-104.
- Dunbar, A. (2011). *Simulation of Ductile Crack Propagation in Pipeline Steels using Cohesive Zone Modelling*. Master's Thesis. Ottawa: Carleton University.
- Falk, M., Needleman, A., & Rice, J. (2001). A critical evaluation of cohesive zone models of dynamic fracture. *Journal of Physics IV*, 11, 543-550.
- Higuchi, R., Makino, H., & Takeuchi, I. (2009). New concept and test method on running ductile fracture arrest for high pressure gas pipeline. *World Gas Conference* (pp. 2730-2737). WGC.

- Hillerborg, A., Modeer, M., & Peterson, P. (1976). Analysis of Crack Formation and Crack Growth in Concrete by Means of Fracture Mechanics and Finite Elements. *Cement and Concrete Research*, 6(6), 773-782.
- Horsley, D. (2003). Background to the use of CTOA for prediction of dynamic ductile fracture arrest in pipelines. *Engineering Fracture Mechanics*, 70(3-4), 547-552.
- ISO 22889. (2013). Metallic materials -- Method of test for the determination of resistance to stable crack extension using specimens of low constraint. International Standards Organization.
- Johnson, G., & Cook, W. (1983). A Constitutive Model and Data for Metals Subjected to Large Strains, High Strain Rates and High Temperature. *7th International Symposium on Ballistics*, (pp. 541-547). The Hague, Netherlands.
- Leis, B., Eiber, R., Carlson, L., & Gilroy-Scott, A. (1998). Relationship between apparent (total) charpy vee-notch toughness and the corresponding dynamic crack propagation resistance. *International Pipeline Conference* (pp. 723-731). Calgary: IPC1998-2084.
- Li, H., & Chandra, N. (2002). Analysis of crack growth and crack-tip plasticity in ductile materials using cohesive zone models. *International Journal of Plasticity*, 19(6), 849-882.
- Martinelli, A., & Venzi, S. (1996). Tearing modulus, J-integral, CTOA and crack profile shape obtained from the load-displacement curve only. *Engineering Fracture Mechanics*, 53(2), 263-277.
- Maxey, W., Keifner, J., & Eiber, R. (1976). *Ductile Fracture Arrest in Gas Pipelines*. A.G.A catalogue number L32176.

- Moes, H., & Belytschko, T. (2002). Extended finite element method for cohesive crack growth. *Engineering fracture Mechanics*, 69(7), 813-833.
- National Energy Board. (2014). *Canadian Regulated Pipelines - Pipeline Ruptures*. National Energy Board.
- Needleman, A. (1987). A continuum model for void nucleation by inclusion debonding. *Journal Of Applied Mechanics*, 54(3), 525-531.
- O'Donoghue, P., Kanninen, M., Leung, C., Demofonti, G., & Venzi, S. (1997). The development and validation of a dynamic fracture propagation model for gas transmission pipelines. *International Journal of Pressure Vessels and Piping*, 7(1), 11-25.
- Parmar, S. (2014). *Simulation of Ductile Fracture in Pipeline Steels under Varying Constraint Conditions*. Master's Thesis. Ottawa: Carleton University.
- Ren, Z., & Ru, C. (2013). Numerical investigation of speed dependent dynamic fracture toughness of line pipe steels. *Engineering Fracture Mechanics*, 99, 214-222.
- Reuven, R., McCowan, C., Drexler, E., Shtechman, A., Darcis, P., Treinen, J., . . . McColskey, J. (2008a). Dynamic Apparatus for CTOA Measurement in Pipeline Steels. *International Pipeline Conference* (pp. 273-278). Calgary: IPC2008-64362.
- Reuven, R., McCowan, C., Drexler, E., Shtechman, A., Darcis, P., Treinen, J., . . . McColskey, J. (2008b). CTOA Results for X65 and X100 Pipeline Steels: Influence of Displacement Rate. *International Pipeline Conference* (pp. 279-286). Calgary: IPC2008-64363.
- Revie, R. (2015). *Oil and Gas Pipelines: Integrity and Safety Handbook*. John Wiley & Sons Inc.

- Rice, J., & Sorensen, E. (1978). Continuing crack-tip deformation and fracture for plane-strain crack growth in elastic-plastic solids. *Mechanics and Physics of Solids*, 26(3), 163-186.
- Scheider, I., & Brocks, W. (2003). The Effect of the Traction Separation Law on the Results of Cohesive Zone Crack Propagation Analyses. *Key Engineering Materials*, 251, 313-318.
- Schwalbe, K.-H., Scheider, I., & Cornec, A. (2013). *Guidelines for Applying Cohesive Models to the Damage Behaviour of Engineering Materials*. London: Springer Heidelberg.
- Seigmund, T., & Brocks, W. (2000). A numerical study on the correlation between the work of separation and the dissipation rate in ductile fracture. *Engineering Fracture Mechanics*, 67(2), 139-154.
- Shen, G., Bouchard, R., Gianetto, J., & Tyson, W. (2008). Fracture Toughness Evaluation of High Strength Steel Pipes. *ASME Pressure Vessels and Piping Division Conference* (pp. 1275-1282). Chicago: PVP2008-61100.
- Shim, D., Mohammed, U., Wilkowski, G., & Duan, D. (2013). Simulation of drop-weight tear test (DWTT) using cohesive zone model. *International Pipeline Technology Conference*. Ostend: IPTC: S35-01.
- Shim, D., Mohammed, U., Wilkowski, G., Duan, D., & Ferguson, J. (2014). Comparison Between Standard and Modified Back-Slotted DWTT Specimens. *International Pipeline Conference*. Calgary: IPC2014-33430.

- Shim, D., Wilkowski, G., Rudland, D., Rothwell, B., & Merritt, J. (2008). Numerical Simulation of Dynamic Fracture Propagation Using Cohesive Zone Modelling. *International Pipeline Conference* (pp. 21-28). Calgary: IPC2008-64049.
- Simha, H., Xu, S., & Tyson, W. (2014). Non-local phenomenological damage-mechanics-based modelling of the Drop-Weight Tear Test. *Engineering Fracture Mechanics*, *118*, 66-82.
- Tanguy, B., Besson, J., Piques, R., & Pineau, A. (2005). Ductile to brittle transition of an A508 steel characterized by Charpy impact test Part I: experimental results. *Engineering Fracture Mechanics*, *72*(1), 49-72.
- Tvergaard, V., & Hutchinson, J. (1992). The Relation Between Crack Growth Resistance and Fracture Process Parameters in Elastic-Plastic Solids. *Mechanical Physical Solids*, *40*(6), 1377-1397.
- Tvergaard, V., & Hutchinson, J. (1994). Effect of T-Stress on mode I crack growth resistance in a ductile solid. *Solids and Structures*, *31*(6), 823-833.
- Uddin, M., & Wilkowski, G. (2016). Simulation of Dynamic Crack Propagation and Arrest using Various Types of Crack Arrestor. *International Pipeline Conference* (p. V003T05A014). Calgary: IPC2016-64561.
- Valentin, T., Magain, P., Quik, M., Labibes, K., & Albertini, C. (1997). Validation of Constitutive Equations for Steels. *Mechanical and Physical Behaviour of Materials under Dynamic Loading*, *7*, pp. C3-611-C3-615.
- Volokh, K. (2004). Comparison Between Cohesive Zone Models. *Numerical Methods in Biomedical Engineering*, *20*(11), 845-856.

- Wang, J., & Shuai, J. (2012). Measurement and analysis of crack tip opening angle in pipeline steels. *Engineering Fracture Mechanics*, 79, 36-49.
- Williams, M. (1957). On the stress distribution at the base of a stationary crack. *Journal of Applied Mechanics*, 24, 109-114.
- Xu, S. (2016a). Private correspondence between Xu and the author regarding experimental results of quasi-static uniaxial tensile tests for X70 and X100.
- Xu, S. (2016b). Private correspondence between Xu and the author regarding experimental results of a DWTT for X70 and X100. Ottawa.
- Xu, S., & Tyson, W. (2015). Effect of Strain Rate on Strength, and of Orientation on toughness, of modern high strength pipe Steels. *Pipeline Engineering*, 14(3), 211-224.
- Xu, S., Bouchard, R., & Tyson, B. (2004). Flow Behavior and Ductile Fracture Toughness of a High Toughness Steel. *International Pipeline Conference* (pp. 1725-1732). Calgary: IPC2004-0192.
- Xu, S., Bouchard, R., & Tyson, B. (2007). Simplified single-specimen method for evaluating CTOA. *Engineering Fracture Mechanics*, 74(15), 2459-2464.
- Xu, S., Sollen, J., Liang, J., Zavadil, R., & Tyson, W. (2014). Effects of Notch Type and Loading Rate on the CTOA of Modern X65 and X70 Pipe Steels. *International Pipeline Conference*. Calgary: IPC2014-33334.
- Xu, S., Tyson, W., & Bouchard, R. (2009). Experimental Validation of Simplified Single-Specimen CTOA Method for DWTT Specimens. *International Conference on Fracture*. Ottawa: ICF2009-269.

- Xu, S., Tyson, W., & Rothwell, B. (2015). Recent Developments in Design for Crack Arrest Using the Crack Tip Opening Angle (CTOA). *Pipeline Engineering*, 14(4), 241-247.
- Xu, S., Tyson, W., Eagleson, R., & Park, D.-Y. (2011). Crack Tunnelling and Crack Tip Opening Angle in Drop-Weight Tear Test Specimens. *International Journal of Fracture*, 172(1), 105-112.
- Xu, S., Tyson, W., Eagleson, R., McCowan, C., Drexler, E., McCloskey, J., & Darcis, P. (2010). Measurement of CTOA of Pipe Steels Using MDCB and DWTT Specimens. *International Pipeline Conference* (pp. 269-278). Calgary: IPC 2010-31076.
- Yu, P., & Ru, C. (2015). Strain rate effects on dynamic fracture of pipeline steels: Finite element simulation. *International Journal of Pressure Vessels and Piping*, 126-127, 1-7.
- Yuan, H., & Li, X. (2014). Effects of the cohesive stiffness on ductile crack propagation simulation by using cohesive zone models. *Engineering Fracture Mechanics*, 126, 1-11.